MECHANISTIC MODEL VALIDATION OF PRODUCTION DECLINE CURVE ANALYSIS FOR UNCONVENTIONAL RESERVOIRS

A Thesis

By

MIKHAIL GORDITSA

Submitted to the Office of Graduate and Professional Studies of
Texas A&M University
in partial fulfillment of the requirements for the degree of

MASTER OF SCIENCE

Chair of Committee,	George J. Moridis
Co-Chair of Committee,	Peter P. Valko
Committee Members,	Thomas A. Blasingame
	Eduardo Gildin
Head of Department,	Jeff Spath

May 2020

Major Subject: Petroleum Engineering

ABSTRACT

A mechanistic reservoir simulation model is presented to study the time-rate relationships of flow in a multi-fractured horizontal well in unconventional reservoirs involving (a) a three-phase oil-gas-water system and (b) a two-phase gas-water system. In addition, non-mechanistic scenarios are also considered, including early-time high water production (*i.e.,* flowback) and fracture permeability degradation. The results are compared to those from previously published models of decline curve analysis, and are used to develop a new time-rate model.

A "fit-for-purpose" numerical reservoir simulator is developed and, following validation against analytical solutions, is used to generate time-rate data. Several simulation cases were constructed from various reservoir and fluid properties that were gathered from published literature to model typical conditions of major US unconventional plays. The reservoir simulator models the pressure-dependent reservoir and fracture properties, the multiphase-multicomponent flow of black oil and gas-water systems, and accounts for non-laminar (Forchheimer/Klinkenberg) flow and gas adsorption in gas-water systems encountered in shale gas reservoirs. A new decline curve analysis model is proposed based on the data generated in this study, and is compared to the Modified-Hyperbolic and the Power-Law/Stretched-Exponential decline curve analysis (DCA) models.

Four flow regimes were successfully generated by the mechanistic model: an early-time fracture-dominated performance, a transient (linear) flow regime, a transitional flow behavior, and a boundary-dominated flow. The effects of spatial discretization on the accuracy of the numerical solution were investigated and proved to be significant,

particularly for the wetting phase — leading to a conclusion that coarser grids tend to overpredict the wetting phase production.

The "non-mechanistic" scenarios were found to only affect the early-time production performance when compared to a given "mechanistic" scenario both in the three-phase black oil case and in the two-phase gas-water case. Production profiles generated in the "non-mechanistic" cases were shown to converge to the "mechanistic" ones no later than in 30 days. The additional computing time that was necessitated by the simulation of the "non-mechanistic" behavior, coupled with the lack of any significant impact on the production rates, suggests that the effects investigated should not be considered.

A "K_1-Exponential (K1X)" DCA model is proposed based on the results generated in this work. The K1X model was shown to fit the flow regimes and its derivatives observed in both black oil and gas-water cases quite well. The features affecting the terminal decline phase of production were identified from the sensitivity analysis of production profiles to various simulation input parameters. Based on the sensitivity analysis results, the terminal decline parameter correlations to the reservoir, fracture and fluid properties were developed for the new K1X model, as well as for the standard DCA models.

DEDICATION

This thesis is dedicated to my friends and family.

ACKNOWLEDGEMENTS

I would like to thank:

Dr. Tom Blasingame, for all of your guidance, support and most importantly a push well outside of my comfort zone that has given me the opportunity to achieve more than I thought possible.

Dr. George Moridis, for all of your help and patience — and in particular, for giving me the keys to the spaceship of supercomputing.

Dr. Peter Valko, for all of your kind support during my first year at Texas A&M, for your excellent teaching and for your service on my committee.

Dr. Eduardo Gildin, for your excellent teaching and for your service on my committee.

Dr. Iskander Diyashev, for your mentorship, advice and your encouragement for me to apply to the Department of Petroleum Engineering at Texas A&M.

All of the friends I made in College Station (S.G.). Your friendship helped me through my studies here.

And lastly, to the Moridis-Blasingame research group, for sharing this bumpy, but ultimately fulfilling, path with me.

CONTRIBUTORS AND FUNDING SOURCES

Contributors

This work was supervised by a thesis committee consisting of Dr. George Moridis (chair), Dr. Peter Valko (co-chair), and Dr. Eduardo Gildin (member) of the Department of Petroleum Engineering and Dr. Tom Blasingame (member) of the Departments of Geology and Geophysics and Petroleum Engineering.

Funding Sources

Graduate study was supported by the Crisman Institute for Petroleum Research from Texas A&M University, and by a fellowship provided by the Texas Engineering Experiment Station and the Department of Petroleum Engineering at Texas A&M University through their start-up funding of the projects of Professor G. Moridis. The contents of this thesis are solely the responsibility of the authors and do not necessarily represent the official views of the Texas A&M Department of Petroleum Engineering or the Crisman Institute for Petroleum Research from Texas A&M University.

TABLE OF CONTENTS

LIST OF FIGURES

LIST OF TABLES

CHAPTER I

INTRODUCTION

1.1 Statement of The Problem

The purpose of this research is to develop a mechanistic model for a typical multi-fractured-horizontal well in unconventional reservoirs and to identify key features that affect the production rates over time (*i.e.,* the so-called "time-rate" data). Once validated, this model can be used to study time-rate relationships typical for unconventional reservoirs including:

- Modified Hyperbolic Decline [Robertson 1988].

The modified hyperbolic decline model is the current industry standard for decline curve analysis (DCA) as it can model two flow regimes — linear flow (*i.e.,* the hyperbolic part) and boundary-dominated flow (*i.e.,* the terminal decline consisting of an exponential "tail"). However, the terminal decline parameter, required by the exponential decline relation, is a subjective parameter which cannot be predicted for a well in an unconventional reservoir during transient flow.

Two newer models that were developed empirically and were tested for applicability to wells in unconventional gas reservoirs are:

- The Power Law Exponential Decline [Ilk 2008, 2009]
- The Stretched Exponential Decline [Valko 2009, Valko & Lee 2010]

None of these models is known to be related to an analytical solution to the diffusivity equation. However, each model does have a tie to a specific flow regime or some other characteristic behavior. Based on my numerical modeling, a new DCA model that I

propose (based on the modified Bessel function (K_1 (x)) may be linked to an analytical solution for fractured wells.

An aspect of performance behavior that must be addressed is the "non-mechanistic" behavior of multi-fractured horizontal wells. Such "non-mechanistic" effects occur when a particular flow regime cannot be clearly observed, or is "masked" by some non-ideal aspect of the production behavior. This makes the choice of the correct DCA model impossible in a practical sense. Such non-mechanistic scenarios include:

- Early-time water unloading from the fractures
- Late time fracture permeability degradation [El Sgher et al 2018]

This study focuses on testing the applicability of the currently accepted DCA models against that of a mechanistic model representing typical conditions and various non-mechanistic scenarios encountered in multiphase flow in a horizontal-multi-fractured well in an unconventional reservoir.

1.2 Objectives

The objectives of this work are as follows:

- To *model* and *evaluate* the effect of pressure-dependent reservoir and fracture properties.
- To *model* and *evaluate* the effect of multiphase flow behavior of black oil and dry gas systems
- To *determine* the effects of spatial discretization on numerical solution

- To *model* non-laminar flow (turbulent/Forchheimer and inertial/Klinkenberg) and adsorption for dry gas systems.
- To *model* early-time performance that is often dominated by very high-water production (*i.e.,* flowback).
- To *develop* a new DCA model based on the results of this work.
- To *compare* the new/proposed DCA model to the current "standard" DCA models:
  - Modified Hyperbolic
  - Power Law Exponential/Stretched Exponential

1.3 Organization of The Research

Chapter II provides a review of published literature on the key concepts of Decline Curve Analysis (DCA), as well as descriptions of the most commonly used decline curve models and ties to particular flow regimes and analytical solutions. This background helps us identify DCA models which are most appropriate for our specific problem of multiphase flow towards a multi-fractured horizontal well in an unconventional reservoir.

Chapter III presents the description of the numerical simulator used as the mechanistic model for this study, and the description of some special features for modelling non-mechanistic behavior.

In **Chapter IV** the mechanistic model is validated against analytical solutions and numerical simulation results for both mechanistic and non-mechanistic scenarios. Parametric analysis results are also provided. For example, the effect of spatial discretization on the accuracy of the numerical solution is investigated.

Chapter V describes (a) the proposed DCA model based on the cases generated in this study, (b) comparisons to analytical solutions, (c) the validation against the mechanistic model, (d) field data and (e) a comparison to the "standard" DCA models. **Chapter V** also contains the correlations developed to estimate the terminal decline parameter for each of the considered models, as well as the rate-time data smoothing technique that was developed for the field cases presented in this work.

Chapter VI provides a summary of the results and the conclusions derived from this work, as well as recommendations for future work.

Appendix A provides an inventory of the parameters and data used in the numerical simulation studies. **Appendix B** presents the full derivation of the *D*- and *b*-parameter functions for the proposed "K_1-Exponential (K1X)" rate-time model. **Appendix C** provides the derivation of the approximate limiting form of the K1X model, as well as the derivation of the *D*- and *b*-parameter functions and the cumulative production function for this limiting form of the K1X model. **Appendix D** provides a final, generalized form of the approximate form of the K1X given in **Appendix C,** which is a hybrid "hyperbolic-exponential" formulation. The derivation of the *D*- and *b*-parameter functions and the cumulative production function for the "hyperbolic-exponential" formulation are also provided in **Appendix D**.

CHAPTER II

LITERATURE REVIEW

The purpose of this chapter is to provide a brief overview of the current status of decline curve analysis and its ties to analytical solutions to the diffusivity equation and particular flow regimes.

2.1 General Concepts — Decline Curve Analysis (DCA)

In general, DCA is production rate extrapolation in time. This methodology has been used to forecast production and estimate ultimate recovery since as early as 1908 (Arnold and Anderson). Johnson and Bollens (1928) introduced the concept of *loss ratio*, expressed by:

$$a = -\frac{q}{\Delta q / \Delta t}. \quad \text{.....(2.1)}$$

Their methodology for rate extrapolation was to calculate consequent time-rate data points from the loss ratio of the previous data points. In cases where the loss ratio was not constant, Johnson and Bollens (1928) recommended repeating the procedure using the loss ratio differences.

Arps (1945) generalized previous work and replaced the differences in **Eq.2.1** with the rate derivative, thus redefining the loss ratio as:

$$a = -\frac{q}{dq / dt}, \quad \text{.....(2.2)}$$

If q_i is the initial production rate and assuming that the loss ratio is constant, **Eq.2.3** can be integrated to yield the exponential decline curve formulation:

$$q = q_i \exp\left[-\frac{t}{a}\right]. \quad (2.3)$$

It is important to note that this work uses a different notation from that in the original Arps formulation. Thus, from this point onward, by the term *loss ratio* I refer to the following formulation:

$$D = -\frac{1}{q}\frac{dq}{dt}, \quad (2.4)$$

With this notation, **Eq.2.3** becomes:

$$q = q_i \exp\left(-Dt\right). \quad (2.5)$$

For cases in which the loss ratio is not constant, Arps (1945) introduced another parameter – the derivative of the loss ratio or *b-parameter*, which is defined as:

$$b = \frac{d}{dt}\left[\frac{1}{D(t)}\right]. \quad (2.6)$$

Integration of **Eq.2.6** yields the loss ratio of hyperbolic decline:

$$D\left(t\right) = \frac{D_i}{1 + bD_i t}, \quad (2.7)$$

where D_i is the initial decline rate. Substituting **Eq.2.7** into **Eq.2.4** yields:

$$\frac{dq}{q} = -\frac{D_i dt}{1 + bD_i t}, \quad (2.8)$$

Integration of **Eq.2.8** provides the formulation for hyperbolic decline:

$$q(t) = q_i \left(1 + D_i b t\right)^{-1/b} . \quad (2.9)$$

Cumulative production is defined by:

$$Q(t) = \int_0^t q(t)\, dt , \quad (2.10)$$

For this work, the *rate-integral* function is defined by:

$$q_{\text{int}}(t) = \frac{Q(t)}{t} , \quad (2.11)$$

or

$$q_{\text{int}}(t) = \frac{1}{t}\int_0^t q(t)\, dt . \quad (2.12)$$

2.2 Decline Curve Analysis Models

Modified Hyperbolic Decline

The industry standard of decline curve analysis for unconventional reservoirs is the Modified Hyperbolic Decline model. Robertson (1988) introduced this model and suggested that, at a certain point in time, the rate-function behavior changes from hyperbolic to exponential. Mathematically, the model is given by:

$$q(t) = \begin{cases} q_i \left(1 + D_i b t\right)^{-1/b} & , t < t_{\text{lim}} \\ q_{\text{lim}} \exp\left[-D_{\text{lim}} \left(t - t_{\text{lim}}\right)\right] & , t > t_{\text{lim}} \end{cases} , \quad (2.13)$$

where $t_{\lim}$ is the "switch" time, $q_{\lim}$ is the rate at $t_{\lim}$, and both of them are inferred from $D_{\lim}$ – the terminal decline. Formulation of $q_{\lim}$ and $t_{\lim}$ are given by:

$$q_{\lim} = q_i \left[\frac{D_{\lim}}{D_i} \right]^{1/b}, \quad (2.14)$$

$$t_{\lim} = \frac{1}{bD_i} \left[\left(\frac{q_i}{q_{\lim}} \right)^b - 1 \right]. \quad (2.15)$$

Obviously, it is necessary to know the terminal decline parameter in order to correctly predict the *switch* point (**Eqs. 2.14-2.15**). Note that the lack of a rigorous method for estimating the terminal decline often leads to non-unique and highly variable forecasts and reserves estimates.

Stretched Exponential Decline

Valko (2009) introduced another model based on the stretched exponential function, which was first proposed by Kohlrausch (1854) to describe the discharge of a capacitor. Valko (2009) used the data from more than ten thousand gas wells in the Barnett Shale to develop and validate the model. The novelty of this approach was to ignore the Arps definitions (1945) and to focus on the data. The stretched exponential time-rate relationship is given by:

$$q(t) = q_i \exp\left[-\left(\frac{t}{\tau} \right)^n \right], \quad (2.16)$$

where τ, n are the model parameters, and q_i is not the initial production rate but the maximum rate, after which the rate function starts to decline.

The parameters for the stretched exponential model can be determined from history matching either by curve fitting (non-linear regression) or from constructing case-specific type curves in dimensionless rate and dimensionless cumulative production coordinates. Having determined the parameters, one can rigorously calculate the estimated ultimate recovery (EUR) and the recovery potential function.

The cumulative production function for the stretched exponential decline is given by:

$$Q(t) = q_i \frac{\tau}{n}\left[\Gamma\left[\frac{1}{n}\right] - \Gamma\left[\frac{1}{n}, \left(\frac{t}{\tau}\right)^n\right]\right], \quad (2.17)$$

where $\Gamma\left[\frac{1}{n}\right]$ and $\Gamma\left[\frac{1}{n}, \left(\frac{t}{\tau}\right)^n\right]$ are the gamma and the incomplete gamma functions, respectively.

The EUR and recovery potential (fraction) are given by:

$$EUR = q_i \frac{\tau}{n}\Gamma\left[\frac{1}{n}\right], \quad (2.18)$$

$$rp = 1 - \frac{Q(t)}{EUR} = \frac{1}{\Gamma\left[\frac{1}{n}\right]}\Gamma\left[\frac{1}{n}, -\ln\left(q_D\right)\right], \quad (2.19)$$

where q_D is the dimensionless rate function that is described by the following equation:

$$q_D(t) = \frac{q(t)}{q_i} = \exp\left[-\left(\frac{t}{\tau}\right)^n\right]. \quad (2.20)$$

The matching technique proposed by Valko (2009) included tuning the n-parameter to achieve a straight line on the plot of the recovery potential vs. the dimensionless cumulative production.

Power-Law Exponential Decline

Ilk et al (2008) derived a time-rate relationship from the observed power-law behavior of the Arps (1945) loss-ratio parameter given by:

$$D(t) = D_\infty + D_1 t^{n-1}, \quad \text{.....(2.21)}$$

where D_∞ is the terminal decline constant, and D_1 and n are model parameters.

Substitution of **Eq. 2.21** into **Eq. 2.4** and integration yields:

$$q_D(t) = \exp\left[-D_\infty t - \frac{D_1}{n} t^n\right]. \quad \text{.....(2.22)}$$

Multiplying **Eq. 2.22** by the so-called rate *intercept* and introducing a new parameter gives the original formulation of the power-law exponential decline curve model:

$$q(t) = q_i \exp\left[-D_\infty t - \hat{D}_i t^n\right]. \quad \text{.....(2.23)}$$

Note that, if the D_∞ parameter is set to zero, **Eq. 2.23** becomes identical to **Eq. 2.16** (*i.e.,* the stretched exponential model). Therefore, the only mathematical difference between the stretched exponential and the power-law exponential models is the terminal decline parameter (D_∞).

The Arps (1945) *b*-parameter for the power-law exponential model can be derived from substituting **Eq. 2.21** into **Eq. 2.6**, which yields:

$$b(t) = -\frac{D_1(n-1)t^n}{(D_\infty t + D_1 t^n)^2}. \quad (2.24)$$

For the sake of consistency, I use the stretched exponential DCA model formulated in terms of the Ilk et al (2008) variables. Substituting $\tau^{-n} = \hat{D}_i$ into **Eqs. 2.16** and **2.17** leads to:

$$q(t) = q_i \exp\left[-\hat{D}_i t^n\right], \quad (2.25)$$

$$Q(t) = -q_i \frac{\hat{D}_i^{-1/n}}{n}\Gamma\left[\frac{1}{n}, \hat{D}_i t^n\right]. \quad (2.26)$$

The reciprocal of the loss ratio and the loss ratio derivative for the stretched exponential DCA model are:

$$D(t) = \frac{\hat{D}_i}{n} t^{n-1}, \quad (2.27)$$

$$b(t) = -\frac{n\hat{D}_i (n-1) t^n}{\left(\hat{D}_i t^n\right)^2}. \quad (2.28)$$

2.3 Analytical Solutions

It should be mentioned that all of the presented time-rate relations are empirical in nature. However, some among them can be shown to model a particular flow regime or an analytical solution. In this section I analyze the ability of DCA models to represent an analytical solution for a particular problem or flow regime.

Transient Linear Flow

In their classic reference, Gringarten et al (1974) proposed an analytical solution to the problem of production from a vertically fractured well in an infinite reservoir. The early-time limiting form for that solution is known as the linear-flow solution and is given by:

$$p_{wD}\left(t_{Dxf}\right)=\sqrt{\pi t_{Dxf}}\,, \quad (2.29)$$

where

$$p_{wD}=\frac{2\pi kh}{q\mu}\left(p_i-p_{wf}\right), \quad (2.30)$$

$$t_{Dxf}=\frac{kt}{\phi\mu c_t x_f{}^2}. \quad (2.31)$$

Substituting **Eqs. 2.30-2.31** into **Eq. 2.29,** and solving for the production rate, yields the linear flow "time-rate" expression:

$$q\left(t\right)=2x_f h\sqrt{\frac{\pi\phi c_t k}{\mu}}\frac{1}{\sqrt{t}}. \quad (2.32)$$

Recasting **Eq. 2.32** in a more compact form leads to:

$$q\left(t\right)=A_f C t^{-1/2}, \quad (2.33)$$

where

$$A_f=2x_f h, \quad (2.34)$$

$$C=\sqrt{\frac{\pi\phi c_t k}{\mu}}. \quad (2.35)$$

Assuming $b = 2$, **Eq. 2.33** can be represented by hyperbolic decline relation (**Eq. 2.9**):

$$q(t) = q_i \left(1 + 2D_i t\right)^{-1/2} . \quad (2.36)$$

As t becomes large, $\left(1 + 2D_i t\right)^{-1/2}$ approaches $\left(2D_i\right)^{-1/2} t^{-1/2}$, which is approximated as:

$$q(t) \approx q_i \left(2D_i\right)^{-1/2} t^{-1/2} = at^{-1/2} . \quad (2.37)$$

It is clear that **Eq. 2.33** is equivalent to **Eq. 2.37** — and therefore, the hyperbolic decline relation can be used to model linear flow toward a multi-fractured horizontal well producing under transient flow conditions.

Boundary Dominated Flow

Symmetries about various planes in a multi-fractured horizontal well system suggests that the problem can be divided into a number of repetitive elements, or *stencils*, each one of which represents the drainage volume of the area of one-half of a single hydraulic fracture multiplied by the height of a single fracture and half of the fracture spacing. Following this concept, the *stencil* can be approximated as a bounded rectangular reservoir, thus allowing the application of the Dietz (1965) solution that is given by:

$$p_{wD}(t_{DA}) = 2\pi t_{DA} + \frac{1}{2} \ln\left[\frac{4A}{e^{\gamma} C_A r_w^{\,2}}\right] + s , \quad (2.38)$$

where γ is the Euler's constant, C_A is the Dietz shape factor, and s is the skin.

The Van Everdingen and Hurst (1949) relationship between the solutions for constant bottom-hole pressure and constant production rate in the Laplace domain is given by:

$$\overline{p}_{wD}(u)\overline{q}_D(u)=\frac{1}{u^2}, \quad (2.39)$$

where u is the Laplace transform variable.

Taking the Laplace transform of **Eq. 2.38** leads to:

$$\overline{p}_{wD}(u)=\frac{2\pi}{u^2}+\frac{1}{u}\left[\frac{1}{2}\ln\left(\frac{4A}{e^{\gamma}C_A r_w^{\,2}}\right)+s\right]. \quad (2.40)$$

Substituting **Eq. 2.40** into **Eq. 2.39** and solving for $\overline{q}_D(u)$ yields:

$$\overline{q}_D(u)=\frac{1}{a\left(u+2\pi/a\right)}, \quad (2.41)$$

where a is given by:

$$a=\frac{1}{2}\ln\left(\frac{4A}{e^{\gamma}C_A r_w^{\,2}}\right)+s. \quad (2.42)$$

Taking the inverse Laplace transform of **Eq. 2.41** results in the following identity:

$$q_D(t_{DA})=\frac{1}{a}\exp\left(-\frac{2\pi t_{DA}}{a}\right), \quad (2.43)$$

where:

$$t_{DA}=\frac{kt}{\phi c_t \mu A} \quad (2.44)$$

Note that **Eq. 2.43** is identical to **Eq. 2.3**. This observation proves that the approach described by Raghavan (1993) provides a theoretical basis for using the Arps (1945) exponential decline model for boundary-dominated flow problems.

Fully Penetrating Vertical Fracture in a Closed Rectangular Reservoir

Ozkan and Raghavan (1988) derived a library of point source solutions in the Laplace domain to estimate the pressure distributions for various reservoir and fracture conditions. In my work, I consider the problem of a multi-fractured horizontal well using the single fracture solution provided by the Ozkan and Raghavan (1988) solution in a closed rectangular reservoir, which is given in the Laplace domain by the following equation:

$$\overline{p}_D\left(x_D, y_D, u\right) = \frac{\pi}{x_{eD} u}\left[\frac{\cosh\left[\sqrt{u}\left(y_{eD} - \left|y_D - y_{wD}\right|\right)\right] + \cosh\left[\sqrt{u}\left(y_{eD} - \left|y_D + y_{wD}\right|\right)\right]}{\sqrt{u}\sinh\left[\sqrt{u}\, y_{eD}\right]}\right.$$
$$+ \frac{2x_{eD}}{\pi}\sum_{k=1}^{\infty}\frac{1}{k}\sin\left[k\pi\frac{1}{x_{eD}}\right]\cos\left[k\pi\frac{x_{wD}}{x_{eD}}\right]\cos\left[k\pi\frac{x_D}{x_{eD}}\right]$$
$$\left.\times\frac{\cosh\left[\sqrt{u+\frac{k^2\pi^2}{x_{eD}{}^2}}\left(y_{eD} - \left|y_D - y_{wD}\right|\right)\right] + \cosh\left[\sqrt{u+\frac{k^2\pi^2}{x_{eD}{}^2}}\left(y_{eD} - \left|y_D + y_{wD}\right|\right)\right]}{\sqrt{u+\frac{k^2\pi^2}{x_{eD}{}^2}}\sinh\left[\sqrt{u+\frac{k^2\pi^2}{x_{eD}{}^2}}\, y_{eD}\right]}\right] \quad \text{.....(2.45)}$$

For $y_D = y_{wD}$ and $x_D = x_{wD}$ into **Eq. 2.44**, the Laplace-space solution at the wellbore is:

$$\overline{p}_D\left(x_{wD}, y_{wD}, u\right) = \frac{\pi}{x_{eD} u}\left[\frac{\coth\left[\sqrt{u}\, y_{eD}\right]}{\sqrt{u}}\right.$$
$$+ \frac{2x_{eD}}{\pi}\sum_{k=1}^{\infty}\frac{1}{k}\sin\left[k\pi\frac{1}{x_{eD}}\right]\cos\left[k\pi\frac{1}{2}\right]\cos\left[k\pi\frac{1}{2}\right] \quad \text{.....(2.46)}$$
$$\left.\times\frac{\coth\left[\sqrt{u+\frac{k^2\pi^2}{x_{eD}{}^2}}\, y_{eD}\right]}{\sqrt{u+\frac{k^2\pi^2}{x_{eD}{}^2}}}\right]$$

Assuming $x_{eD}=1$, **Eq. 2.46** further simplifies to:

$$\overline{p}_D(u)=\frac{\pi}{u}\frac{\coth\left[\sqrt{u}y_{eD}\right]}{\sqrt{u}} \quad \text{.....(2.47)}$$

Applying **Eq. 2.39** and solving for the dimensionless rate leads to:

$$\overline{q}_D(u)=\frac{1}{\pi}\frac{\tanh\left[\sqrt{u}y_{eD}\right]}{\sqrt{u}} \quad \text{.....(2.48)}$$

Because the solutions given by **Eqs. 2.46-2.48** cannot be analytically inverted into the real time domain, I use the following procedure to obtain the constant bottomhole pressure solution:

- Apply the identity in **Eq. 2.39** to obtain the Laplace domain solution for the dimensionless rate;
- Numerically invert the Laplace domain solution using the Stehfest algorithm [Stehfest 1970].

The solutions given by **Eqs. 2.46-2.48** cannot be clearly connected to a specific decline curve model — however; the numerical inversion results will be used to validate time-rate relations.

Trilinear Model for a Fracture in a Closed Rectangular Reservoir

Lee and Brockenbrough (1986) first formulated the trilinear flow concept, the key assumptions of which are that the fluid flow to a fractured well can be modeled by a system of three 1-D segments:

- Flow from the fracture to the vertical wellbore;
- Flow from the reservoir to the fracture in the direction perpendicular to the fracture;
- Flow in the reservoir in the direction parallel to the fracture.

The assumptions of the trilinear model are well-suited to the case of a multi-fractured horizontal well in an unconventional reservoir. The vast difference between the fracture and matrix permeabilities suggest that the trilinear model is a valid approximation of the actual flow regimes.

Olarewaju and Lee (1989) derived the trilinear solution for a finite rectangular reservoir. Not accounting for skin and wellbore storage, this solution is given in the Laplace domain as:

$$\overline{q}_D(u) = -\frac{\psi \tanh[\psi]}{bu}, \quad (2.49)$$

where

$$\psi = \sqrt{a\sqrt{\sigma}\tanh\left[\left(y_{eD} - w_{fD}\right)\sqrt{\sigma}\right] + C_1 u}, \quad (2.50)$$

$$\sigma = u + \sqrt{u}\tanh\left[\left(x_{eD} - 1\right)\sqrt{u}\right], \quad (2.51)$$

$$a = \frac{2}{C_{fD}}, \quad (2.52)$$

$$b = \frac{-\pi}{C_{fD}}, \quad (2.53)$$

$$C_{fD} = \frac{k_f w_f}{k x_f}, \quad (2.54)$$

$$C_1 = \frac{k\phi_f c_{ft}}{k_f \phi c_t}, \quad (2.55)$$

$$w_{fD} = \frac{w_f}{x_f}. \quad (2.56)$$

Interestingly, **Eq. 2.49** is based on the same hyperbolic tangent function as that in the Ozkan and Raghavan (1988) solution given by **Eq. 2.48**, which was derived without simplifying 1D flow assumptions and is more general. The fact that they both result in the same hyperbolic tangent function shows that the Olarewaju and Lee (1989) solution is an approximation of the more general Ozkan and Raghavan solution (1988).

CHAPTER III

MECHANISTIC MODEL DEVELOPMENT

In order to validate the applicability of DCA models, I developed a "fit-for-purpose" numerical reservoir simulator written in FORTRAN95. This is a fully implicit, three-phase, non-isothermal compositional simulator (involving three-components and/or pseudo-components) that describes all known physical-chemical processes with minimal assumptions and simplifications. The three modeled phases are the organic (oil), gaseous, and aqueous phases, and the three modeled components are oil (actually, a pseudo-component), natural gas and water. All components are soluble in all phases, with the exception of oil component in the gas phase.

Note that the nomenclature in this chapter differs from that commonly found in the SPE literature.

3.1 Governing Equations

Our modeling approach follows the integral finite difference method. According to this method, every gridblock (element) into which the domain is subdivided, conforms to mass and energy balance (Pruess et al., 1999) according to:

$$\frac{d}{dt}\int_{V_n} M^{\kappa} dV = \int_{\Gamma_n} F^{\kappa} \cdot \overline{n}\, d\tilde{A} + \int_{V_n} q^{\kappa} dV \,, \quad (3.1)$$

where V_n is the volume of the subdomain *n*, M^{κ} is the mass accumulation term of the component κ, $\tilde{A}$ and Γ_n are surface area perpendicular to the direction of the unit vector

$\overline{n}$ and total surface area of the grid-block *n*, F^{κ} is the Darcy flux vector of the component κ, q^{κ} is the source/sink term of the component κ.

The Mass accumulation terms for every mass component in **Eq. 3.1** are defined by:

$$M^{\kappa} = \sum_{\beta=A,G,O} \phi S_{\beta} \rho_{\beta} X_{\beta}^{\kappa} \quad \text{.....(3.2)}$$

where ϕ is the porosity, ρ_{β} is the density of phase β, S_{β} is the saturation of phase β, X_{β}^{κ} is the mass fraction of component κ in phase β.

The Heat accumulation terms for every phase and the rock matrix are given by:

$$M^{\theta} = (1-\phi)\rho_R C_R T + \sum_{\beta=A,G,O} \phi S_{\beta} \rho_{\beta} U_{\beta} \quad \text{.....(3.3)}$$

where ρ_R is the bulk density of the rock matrix, C_R is the heat capacity of the dry rock and U_{β} is the specific internal energy of the phase β.

The specific internal energy of the gaseous phase in **Eq. 3.3** is given by:

$$U_G = \sum_{\kappa=w,g,o,s} X_G^{\kappa} u_G^{\kappa} + U_{dep} \left(= H_G - \frac{P}{\rho_G} \right) \quad \text{.....(3.4)}$$

where u_G^{κ} is the specific internal energy of component κ in the gaseous phase, U_{dep} is the specific internal energy departure of the gas mixture and H_G is the specific enthalpy of the gaseous phase.

Similarly, the specific energy of the aqueous and the organic phases in **Eq. 3.3** are given by:

$$U_{O,A} = \sum_{\kappa=w,g,o} X_{O,A}^{\kappa} u_{O,A}^{\kappa} \,, \quad (3.5)$$

where the specific internal energy of the component κ in the aqueous or in the organic phase can be calculated as:

$$u_{O,A}^{\kappa} = h_{O,A}^{\kappa} - \frac{P_{\beta}}{\rho_{\kappa}} = \int_{T_0}^{T} C_{\kappa} dT - \frac{P_{\beta}}{\rho_{\kappa}} \,, \quad (3.6)$$

where $h_{O,A}^{\kappa}$ is the specific enthalpy of component κ in the aqueous or in the organic phase, T_0 is the reference temperature and C_{κ} is the temperature-dependent heat capacity of component κ.

The Mass flux of each component consists of contributions from all mobile phases and is given by:

$$F^{\kappa} = \sum_{\beta=A,G,O} F_{\beta}^{\kappa} \,, \quad (3.7)$$

where the mass flux of the oil and water components in the aqueous and in the organic phase, $F_{\beta}^{o,w}$ is given by:

$$F_{\beta} = -k \frac{k_{r\beta} \rho_{\beta}}{\mu_{\beta}} \left(\nabla P_{\beta} - \rho_{\beta} g \right) \,, \quad (3.8)$$

where k is the intrinsic rock permeability, $k_{r\beta}$ is the relative permeability of phase β (= O,A), μ_{β} is the viscosity of phase β, P_{β} is the pressure of phase β, and g is the gravitational acceleration vector.

The phase pressures P_β in **Eq. 3.8** are given by:

$$P_A = P_G + P_{cGW}, \quad (3.9)$$

$$P_O = P_G + P_{cGO}, \quad (3.10)$$

$$P_G = P_G^g + P_G^w + P_G^o, \quad (3.11)$$

where P_{cGW}, P_{cGO} are the gas-water and gas-oil capillary pressures respectively, and P_G^κ is the partial pressure of the component κ in the gaseous phase. The gas solubility in the aqueous phase is obtained from Henry's law:

$$P_G^g = H^g X_A^g, \quad (3.12)$$

where $H^g = H^g\left(P_G, T\right)$ is a function of pressure and temperature which is equivalent to the Henry's constant in the physical sense.

The mass flux of the gaseous phase accounts for gas slippage effects (Klinkenberg 1941) and is given by:

$$F_G^\kappa = -k\left(1+\frac{b_k}{P_G}\right)\frac{k_{rG}\rho_G}{\mu_G} X_G^\kappa\left(\nabla P_G - \rho_G g\right), \quad (3.13)$$

where b_k is the Klinkenberg parameter.

The Heat flux accounts for conduction- and advection-based heat transfer and is given by:

$$F^\theta = -\lambda_\Theta \nabla T + \sum_{\beta=A,G,O} H_\beta F_\beta, \quad (3.14)$$

where λ_Θ is an appropriate composite thermal conductivity of the rock-fluid system, H_β is the specific enthalpy of the phase β. The specific enthalpy of the gaseous phase is calculated as:

$$H_G = \sum_{\kappa=w,g,o} X_G^\kappa h_G^\kappa + H_{dep} \quad \text{.....(3.15)}$$

where H_{dep} is the specific enthalpy departure of the gas mixture. The specific enthalpy of the aqueous and the organic phase is given as:

$$H_\beta = \sum_{\kappa=w,g,o} X_\beta^\kappa h_\beta^\kappa \quad \text{.....(3.16)}$$

where $\beta = O, A$.

The mass source and sink term in **Eq. 3.1** represents withdrawal or addition of the mass component κ. For injection, q^κ is a known quantity; for production, q^κ is described by:

$$q^\kappa = \sum_{\beta=A,G,O} X_\beta^\kappa q_\beta \quad \text{.....(3.17)}$$

where q_β is the mass production or injection rate of phase β.

The heat source and sink term in **Eq. 3.1** accounts for heat exchange associated with (a) either direct heat addition or withdrawal q^θ (e.g., electrical or microwave heating) and/or (b) the withdrawal or addition of mass, in which case:

$$q^\theta = \sum_{\kappa=w,o,g} q^\kappa h^\kappa \quad \text{.....(3.18)}$$

3.2 Oil Thermophysical Properties

In my approach, I treat oil as a single pseudo-component, as opposed to its treatment in a fully compositional method that would describe each hydrocarbon compound (or families of compounds) as distinct components. Therefore, I can use empirical live-oil (i.e., oil with dissolved gas) correlations.

The oil bubble-point pressure, solution gas oil ratio, oil compressibility and formation volume factor are calculated using the Vazquez and Beggs (1977) correlations for live-oils.

Oil bubble-point pressure is calculated as follows:

$$P_b = \left[\frac{R_s}{C_1 \gamma_g \exp\left(\frac{C_3 \gamma_{API}}{T_R + 459.67} \right)} \right]^{1/C_2}, \quad (3.19)$$

where γ_g is the dissolved gas specific gravity, γ_{API} is the oil API gravity, T_R is the oil temperature in degrees Rankin, and $C_1 - C_3$ are constants given in **Table 3.1**.

Solution gas oil ratio is calculated by rearranging **Eq. 3.19**, yielding:

$$R_s = C_1 \gamma_g P_O^{C_2} \cdot \exp\left(\frac{C_3 \gamma_{API}}{T_R + 459.67} \right), \quad (3.20)$$

where P_O is the organic phase pressure.

Oil compressibility and formation volume factor (FVF) have different correlation for saturated and undersaturated oils (above and below the bubble-point respectively).

Because my code uses density instead of compressibility in the governing equations, it is sufficient to calculate the undersaturated and the saturated oil compressibilities, and then use them to develop the oil density equation.

Undersaturated oil compressibility is given as:

$$c_o = \frac{-1433 + 5 \cdot R_{sb} + 17.2 \cdot T - 1180 \cdot \gamma_g + 12.61 \cdot \gamma_{API}}{10^5 P_O}, \quad (3.21)$$

where R_{sb} is the solution gas oil ratio at the bubble-point conditions.

Undersaturated oil formation volume factor is given by:

$$B_o = B_{ob} \exp\left[c_o \left(P_b - P_O\right)\right], \quad (3.22)$$

where B_{ob} is the oil FVF at the bubble-point conditions.

Saturated oil formation volume factor is given by:

$$B_o = 1 + A_1 R_s + A_2 \left(T - 60\right)\frac{\gamma_{API}}{\gamma_g} + A_3 R_s \left(T - 60\right)\frac{\gamma_{API}}{\gamma_g}, \quad (3.23)$$

where $A_1 - A_3$ are constants presented in **Table 3.1**.

To avoid discontinuities in the FVF during the phase transition (liberation of gas), the following smoothing technique is used:

$$B_o = \frac{1}{2}\left[1 + \tanh\left(0.02\left(p_b - p_o\right)\right)\right] B_o^{\,sat} + \frac{1}{2}\left[1 + \tanh\left(0.02\left(p_o - p_b\right)\right)\right] B_o^{\,undersat}, \quad (3.24)$$

Table 3.1 – Vazquez and Beggs (1977) correlation coefficients

Coefficient	$\gamma_{API} \leq 30$	$\gamma_{API} > 30$	Coefficient	$\gamma_{API} \leq 30$	$\gamma_{API} > 30$
A_1	4.677E-04	4.670E-04	C_1	3.618E-02	1.784E-02
A_2	1.751E-05	1.100E-05	C_2	1.094E+00	1.187E+00
A_3	-1.811E-08	1.337E-09	C_3	2.572E+01	2.393E+01

Dead oil viscosity is calculated using the Egbogah and Ng (1990) correlation, given by:

$$\mu_{od} = 10^{1.8653 - 0.025085\gamma_o - 0.5644\log_{10}(T_F)} - 1. \quad (3.25)$$

Undersaturated live oil viscosity is also calculated using the Egbogah and Ng (1990) correlation as follows:

$$\mu_o = \mu_{ob}\left(\frac{P_O}{P_b}\right)^{2.6P_o^{1.187}\exp\left(-11.513+8.98\cdot10^5 P_o\right)}. \quad (3.26)$$

Saturated live oil viscosity is computed using Bergman and Sutton (2007) correlation, given by:

$$\mu_{ob} = A\mu_{od}{}^{B}, \quad (3.27)$$

where

$$A = \frac{1}{1+\left(\frac{R_{sb}}{a_1}\right)^{a_2}}, \quad (3.28)$$

$$B = a_3 + \frac{1 - a_3}{1 + \left(\frac{R_{sb}}{a_4} \right)^{a_5}}, \quad (3.29)$$

The coefficients $a_1 - a_5$ are presented in **Table 3.2**.

Table 3.2 – Bergman and Sutton (2007) correlation coefficients

a_1	3.442E+02
a_2	8.553E-01
a_3	3.823E-01
a_4	5.680E+02
a_5	8.193E-01

Live oil density is calculated from the following relation:

$$\rho_\beta^o = \frac{\rho_{sc}^o + R_s \rho_{sc}^g}{B_o}, \quad (3.30)$$

where ρ_{sc}^o, ρ_{sc}^g is the oil density and the gas density at standard conditions respectively.

Oil isobaric specific heat is estimated according to an empirical correlation developed by the American Petroleum Institute (API) and cited by Edwards et al. (1983) as:

$$C_o = A_1 + A_2 T_F + A_3 T_F^{\,2}, \quad (3.31)$$

where

$$A_3 = -1.17126 + (0.023722 + 0.024907\gamma_o)K + \frac{(1.14982 - 0.046535K)}{\gamma_o}, \quad (3.32)$$

$$A_2 = 10^{-4}\left(1.0 + 0.82463K\right)\left(1.12172 - \frac{0.27634}{\gamma_o}\right), \quad (3.33)$$

$$A_1 = 10^{-8}\left(1.0 + 0.82463K\right)\left(2.9027 - \frac{0.70958}{\gamma_o}\right), \quad (3.34)$$

where γ_o is the oil specific gravity and K is the Watson characterization factor.

Oil thermal conductivity is calculated using the empirical formula of Edwards et al (1983) as:

$$\lambda_o = \frac{137.0}{\rho_\beta^o}\left[1.0 - 0.00054\left(T_K - 273\right)\right] \quad (3.35)$$

Mutual solubility of a wide range of hydrocarbons and water was studied by Tsonopoulos and Wilson (1983), Economou et al. (1997) and Tsonopoulos (1999). In this work I assume that only the light fractions of oil are soluble in water. Thus, I choose hexane-water mutual solubility correlation (Tsonopoulos 1999), given by:

$$Y_A^o = \exp\left(-374.90804 + \frac{16327.128}{T_K} + 53.89582\ln(T_K)\right), \quad (3.36)$$

$$Y_O^w = \exp\left(6.698073 - \frac{4291.186}{T_K}\right), \quad (3.37)$$

where Y_A^o is the molar fraction of the oil component dissolved in the aqueous phase.

Heat of solution of water in normal alkanes is a constant (Tsonopoulos 1999), which for hexane is computed by:

$$h_w^{solution} = \frac{R}{MW_{H_2O}} 4291.186, \quad (3.38)$$

$$h_O^{solution} = \frac{R}{MW_{Oil}} \left(53.89582 T_K - 16327.128\right). \quad (3.39)$$

where R is the universal gas constant.

3.3 Gas Thermophysical Properties

The gas component in my code is assumed to be 100% methane. However, the gas phase may contain water vapor, which is fully considered. The PVT properties of methane are obtained from the real gas law given by:

$$P_G v_m = Z R T_K, \quad (3.40)$$

where Z is the real gas compressibility factor and v_m is the gas molar volume.

Gas Z-factor is calculated from Peng and Robinson (1977) cubic equation of state (PR-EOS) that is given by:

$$p = \frac{RT}{v_m - b} - \frac{a\alpha}{v_m{}^2 + 2bv_m - b^2}, \quad (3.41)$$

where

$$a = 0.45724 \frac{R^2 T_c{}^2}{p_c}, \quad (3.42)$$

$$b = 0.07780 \frac{RT_c}{p_c}, \quad (3.43)$$

$$\alpha = \left(1 + f_\omega \left(1 - T_r^{1/2}\right)\right)^2, \quad (3.44)$$

$$f_\omega = 0.37464 + 1.54226\omega - 0.26992\omega^2, \quad (3.45)$$

$$T_r = \frac{T}{T_c}, \quad (3.46)$$

ω is the acentric factor of the compound, p_c and T_c are the critical pressure and temperature of the compound. **Eq. 3.41** can be rearranged into the following cubic equation form:

$$Z^3 - (1 - B)Z^2 + \left(A - 2B - 3B^2\right)Z - \left(AB - B^2 - B^3\right) = 0, \quad (3.47)$$

where

$$A = \frac{\alpha a p}{R^2 T^2}, \quad (3.48)$$

$$B = \frac{bp}{RT}. \quad (3.49)$$

<u>*Gas density*</u> is calculated from the z-factor by rearranging **Eq. 3.40**:

$$\rho_\beta^g = \frac{MW_g Z R T_K}{P_G} \quad (3.50)$$

<u>*Gas viscosity at high pressures*</u> is estimated from the Chung et al. (1988) high-pressure viscosity equation that is given by:

$$\mu_g = \mu^* \frac{36.344\left(MW_g T_c\right)^{1/2}}{v_m^{2/3}}, \quad (3.51)$$

$$\mu^* = \frac{\left(T^*\right)^{1/2}}{\Omega_v} F_c \left(G_2^{-1} + E_6 y\right) + \mu^{**}, \quad (3.52)$$

$$y = \frac{\rho v}{6MW_g}, \quad (3.53)$$

$$G_1 = \frac{1 - 0.5y}{\left(1 - y\right)^3}, \quad (3.54)$$

$$G_2 = \frac{E_1 \dfrac{1 - \exp\left(-E_4 y\right)}{y} + E_2 G_1 \exp\left(E_5 y\right) + E_3 G_1}{E_1 E_4 + E_2 + E_3}, \quad (3.55)$$

$$\mu^{**} = E_7 y^2 G_2 \exp\left[E_8 + E_9 \left(T^*\right)^{-1} + E_{10} \left(T^*\right)^{-2}\right], \quad (3.56)$$

$$\Omega_v = 1.16145\left(T^*\right)^{-0.14874} + 0.52487\exp\left(-0.77320T^*\right) + 2.16178\exp\left(-2.43787T^*\right), \quad (3.57)$$

$$T^* = 1.2593T_r, \quad (3.58)$$

$$F_c = 1 - 0.2756\omega \quad (3.59)$$

Parameters $E_1 - E_{10}$ are linear functions of the acentric factor with coefficients given in **Table 3.3**.

Table 3.3 – Chung et al. (1988) coefficients to calculate $E_i = a_i + b_i\omega$

i	a_i	b_i
1	6.324E+00	5.041E+01
2	1.210E-03	-1.154E-03
3	2.283E+00	2.542E+02
4	6.623E+00	3.810E+01
5	1.975E+01	7.630E+00
6	-1.900E+00	-1.254E+01
7	2.428E+01	3.450E+00
8	7.972E-01	1.117E+00
9	-2.382E-01	6.770E-02
10	6.863E-02	3.479E-01

Gas viscosity at low pressures is estimated using the Chung et al. (1984, 1988) method given by:

$$\mu_g^o = 40.785 \frac{F_c \left(MW_g T\right)^{1/2}}{V_c^{2/3} \Omega_v} \quad \text{.....(3.60)}$$

All parameters in **Eq. 3.60** are calculated in the same way as in **Eq. 3.51**.

Ideal gas isobaric specific heat is calculated using a polynomial function of temperature presented in Poling et al (2007), which for methane takes the following form:

$$C_p^g = \frac{R}{MW_g}\left(4.568 - 8.975\cdot10^{-3}T + 3.631\cdot10^{-5}T^2 - 3.407\cdot10^{-8}T^3 + 1.091\cdot10^{-11}T^4\right),$$

..... (3.61)

Ideal gas isochoric specific heat is calculated using the ideal gas relation given by:

$$C_v^g = C_p^g - R\,.$$ ..... (3.62)

Real gas specific enthalpy consists of the ideal part and the departure function and is given by:

$$H_G = H_{ideal} + H_{dep}\,.$$ ..... (3.63)

The ideal part is the temperature integral of the specific heat function and is given by:

$$H_{ideal} = \int_{T_{ref}}^{T} C_g dT\,,$$ ..... (3.64)

where T_{ref} is an arbitrary reference temperature.

The departure function for the Peng and Robinson (1977) cubic equation of state is given by Poling et al (2007) as:

$$H_{dep} = \frac{RT_c}{MW_g}\left[T_r\left(Z-1\right) - 2.078\left(1+f_\omega\right)\sqrt{\alpha}\,\ln\left(\frac{Z+\left(1+\sqrt{2}\right)B}{Z-\left(1-\sqrt{2}\right)B}\right)\right],$$ ..... (3.65)

where T_r, f_ω, α and B are calculated from **Eqs. 3.46- 3.44** and **Eq. 3.49** respectively.

Gas thermal conductivity is calculated according to Chung et al. (1984, 1988) method for a high-pressure single-component real gas, which is given by:

$$\lambda_g = \frac{31.2\mu_g^o \Psi}{MW_g}\left(G_2^{-1} + B_6 y\right) + qB_7 y^2 T_r^{1/2} G_2, \quad (3.66)$$

where

$$\Psi = 1 + \alpha \frac{0.215 + 0.28288\alpha - 1.061\beta + 0.26665\zeta}{0.6366 + \beta\zeta + 1.061\alpha\beta}, \quad (3.67)$$

$$\alpha = \frac{C_v^g}{R} - \frac{3}{2}, \quad (3.68)$$

$$\beta = 0.7862 - 0.7109\omega + 1.3168\omega^2, \quad (3.69)$$

$$\zeta = 2.0 + 10.5T_r^2, \quad (3.70)$$

$$q = 3.586 \cdot 10^{-3} \frac{\left(T_c / MW_g\right)^{1/2}}{V_c^{2/3}}, \quad (3.71)$$

$$y = \frac{V_c \rho_g}{6MW_g}, \quad (3.72)$$

$$G_1 = \frac{1 - 0.5y}{\left(1 - y\right)^3}, \quad (3.73)$$

$$G_2 = \frac{\left(B_1 / y\right)\left[1 - \exp\left(-B_4 y\right)\right] + B_2 G_1 \exp\left(B_5 y\right) + B_3 G_1}{B_1 B_4 + B_2 + B_3}, \quad (3.74)$$

The parameters $B_1 - B_7$ are linear functions of acentric factor and are given by:

$$B_i = a_i + b_i \omega, \quad (3.75)$$

The values of the coefficients a_i and b_i are listed in **Table 3.4**.

Table 3.4 – Chung et al. (1984, 1988) coefficients for Eq. 3.75

i	a_i	b_i
1	2.4166E+00	7.482E-01
2	-5.0924E-01	-1.509E+00
3	6.6107E+00	5.621E+00
4	1.4543E+01	-8.914E+00
5	7.9274E-01	8.202E-01
6	-5.8634E+00	1.280E+01
7	9.1089E+01	1.281E+02

Gas Henry constant as a function of temperature for the estimation of gas solubility in the aqueous phase is calculated using a correlation by Dhima (1998) that is given by:

$$H_A^g = \exp\left(-2.1721 + \frac{7.8856 \cdot 10^3}{T_K} - \frac{1.4196 \cdot 10^6}{T_K{}^2}\right) \quad (3.76)$$

3.4 Water Thermophysical Properties

The thermophysical properties of water in this work are modeled according to the formulations of the International Association for the Properties of Water and Steam (IAPWS, 2018).

The water vapor content in the gaseous phase is calculated from component partial pressures in the following manner:

$$P_G^{CH_4} = P_G - P_G^{H_2O}, \quad (3.77)$$

$$Y_G^{CH_4} = P_G^{CH_4} / P_G, \quad (3.78)$$

$$Y_G^{H_2O} = 1 - Y_G^{CH_4}, \quad (3.79)$$

where $P_G^{H_2O}$ is the water vapor saturation pressure for a given temperature, as computed using the IAPWS (2018) correlations.

All liquid phase properties are assumed to be equal to the mass-weighted average of the properties of the components in phase. All gaseous phase properties are assumed to be equal to the mole-weighted average of the properties of the components in phase.

3.5 Non-Darcy Flow

My code can model two kinds of flow that occur outside the range of validity of Darcy's law, including – micro-flow and turbulent flow.

Micro-flow in porous media occurs in ultra-tight porous media, where the particle-wall interactions interfere with the Brownian motion of gases. My code includes an option for micro-flow according to the Knudsen transport model. In the flux term of the diffusivity equation (**Eq. 3.13**), the extra pressure drop due to friction is accounted for by modifying the effective permeability through the addition of a *Klinkenberg* term. Freeman et al (2011) showed how the Klinkenberg parameter is related to the Knudsen diffusivity and the Knudsen number through the following equations:

$$\frac{b_k}{P_G} = \left(1 + \alpha_K K_n\right)\left(1 + \frac{4K_n}{1 + K_n}\right) - 1, \quad (3.80)$$

$$\alpha_K = \frac{128}{15\pi^2}\tan^{-1}\left[4.0K_n^{\,0.4}\right], \quad (3.81)$$

$$K_n = \frac{\mu_G}{2.81708P_G}\sqrt{\frac{\pi RT\phi}{2kMW_G}}, \quad (3.82)$$

where b_k is the Klinkenberg parameter and K_n is the Knudsen number.

Turbulent flow occurs at high velocities when Darcy's law, which is valid only for laminar flow, is no longer valid. In this case, the pore velocity is estimated from the general momentum-balance Forchheimer equation (Forchheimer, 1901; Wattenbarger and Ramey, 1968; Moridis and Freedman 2014), which is given by:

$$v = \frac{-2\left(\nabla P - \rho g\right)}{\frac{\mu}{kk_r} + \sqrt{\left(\frac{\mu}{kk_r}\right)^2 + 4\beta\rho\left|\left(\nabla P - \rho g\right)\right|}}, \quad (3.83)$$

where β is the *turbulence correction factor* (Katz et al., 1959) and is estimated according to the SI-unit version of the Frederick and Graves (1994) correlation by:

$$\beta = \frac{3.2808}{\theta^2}\exp\left[45 - \sqrt{3205.71 + 81\cdot\ln\left(\frac{kk_r}{\theta}\right)}\right], \quad (3.84)$$

$$\theta = \phi\left(S - S_{irr}\right) \quad (3.85)$$

Eq. 3.83 incorporates laminar, viscous, inertial and turbulence effects and can be introduced into the flux term of the diffusivity equation in a manner similar to that for Darcian velocity, given by:

$$F = v\rho \quad (3.86)$$

3.6 Multiphase Flow

Relative Permeability

The relative permeabilities of the three-phase system in a porous medium (e.g., the matrix in the stencil-based domain in a fractured low-permeability medium) are modeled according to the Dietrich and Bondor (1976) modification of the Stone (1973) three-phase relative permeability model, and are given by:

$$k_{rA} = \left(\frac{S_A - S_{irA}}{1 - S_{irA}} \right)^{n_w}, \quad (3.87)$$

$$k_{roa} = \left(\frac{S_O - S_{irO}}{1 - S_{irA}} \right)^{n_o}, \quad (3.88)$$

$$k_{rog} = \left(\frac{S_O - S_{irO}}{1 - S_{irO}} \right)^{n_o}, \quad (3.89)$$

$$k_{rG} = \left(\frac{S_G - S_{irG}}{1 - S_{irO}} \right)^{n_g}, \quad (3.90)$$

$$k_{rO} = \frac{1}{k_{roca}} \left(k_{roa} + k_{rA} \right) \left(k_{rog} + k_{rG} \right) - \left(k_{rA} + k_{rG} \right) \quad (3.91)$$

The matrix relative permeability curves for the parameters I used in this study are shown on **Figs. 3.1-3.2**.

The relative permeabilities of the three-phase system in the proppant-filled hydraulic fracture of the stencil-based domain are modeled according to a linear relative permeability model given by:

$$k_{rA} = \frac{S_A - S_{irA}}{1 - S_{irA} - S_{irO} - S_{irG}}, \quad (3.92)$$

$$k_{rG} = \frac{S_G - S_{irG}}{1 - S_{irA} - S_{irO} - S_{irG}}, \quad (3.93)$$

$$k_{rO} = \frac{S_O - S_{irO}}{1 - S_{irA} - S_{irO} - S_{irG}}. \quad (3.94)$$

The fracture relative permeability curves that correspond to the parameters I used in this study are shown on **Figs. 3.3-3.4**.

Note that the same three-phase equations **3.87-3.94** are used for the two-phase systems for the sake of consistency. If a phase is not present in the system, a null value is supplied to the corresponding relative permeability equation.

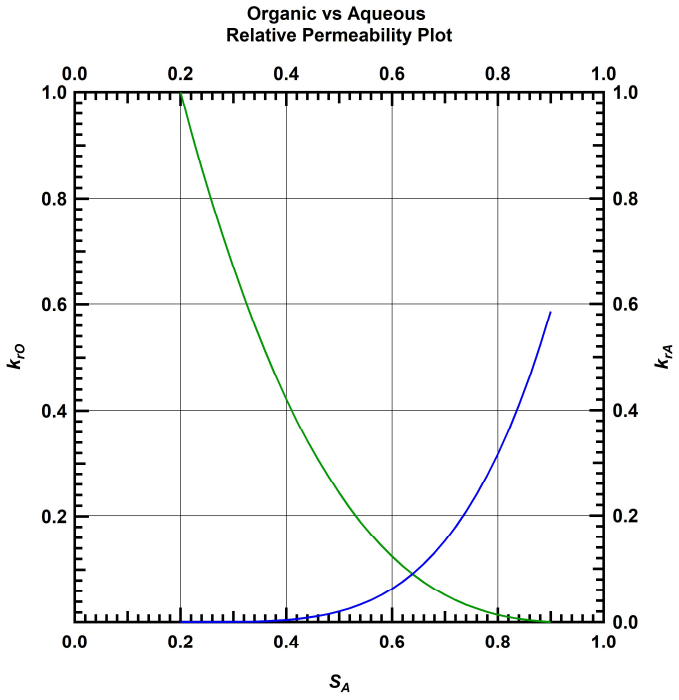

Figure 3.1— Matrix relative permeability curves for the parameters used in this study – organic-aqueous system.

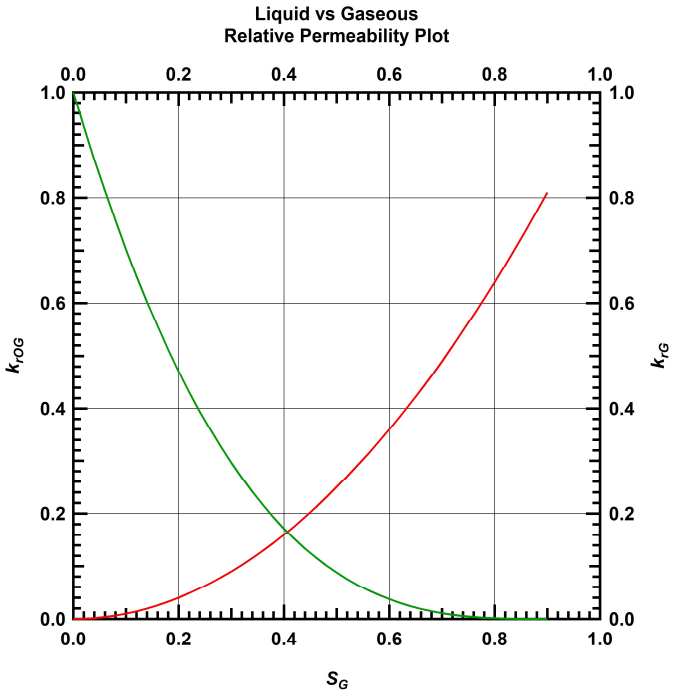

Figure 3.2—Matrix relative permeability curves for the parameters used in this study – liquid-gaseous system.

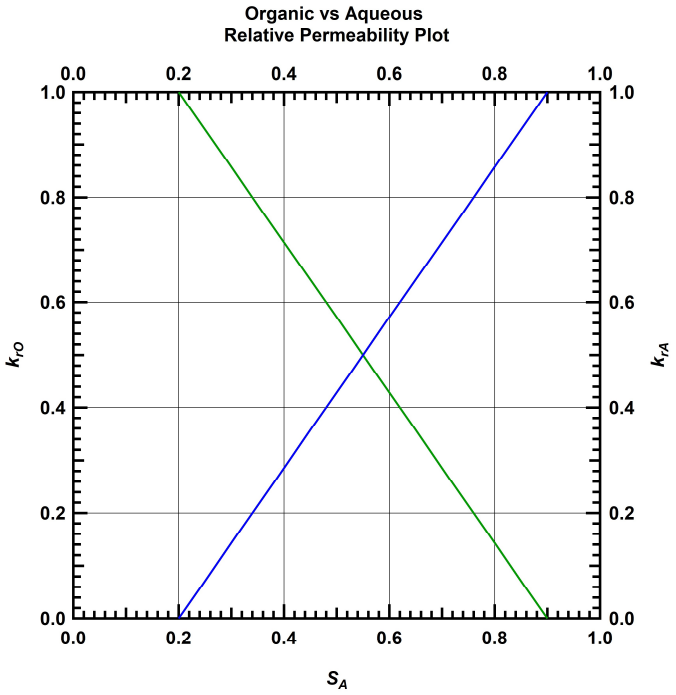

Figure 3.3— Hydraulic fracture relative permeability curves for the parameters used in this study – organic-aqueous system.

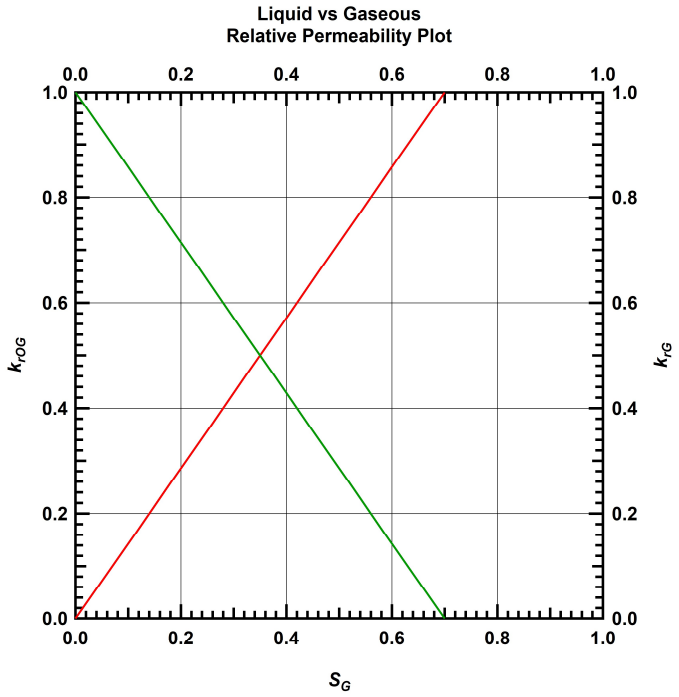

Figure 3.4—Hydraulic fracture relative permeability curves for the parameters used in this study – liquid-gaseous system.

Capillary Pressure

Capillary effects are modeled according to Parker et al. (1987) three-phase extension of the Van Genuchten (1980) two-phase capillary pressure model, and are given by:

$$P_{cOW} = \frac{g}{\alpha_{OW}}\left[\left(\frac{S_A - S_{irA}}{1 - S_{irA}}\right)^{1-1/n} - 1\right]^{1/n}, \quad (3.95)$$

$$P_{cGW} = \frac{g}{\alpha_{GW}}\left[\left(\frac{1 - S_G - S_{irA}}{1 - S_{irA}}\right)^{1-1/n} - 1\right]^{1/n}, \quad (3.96)$$

$$P_{cGO} = P_{cGW} + P_{cOW}, \quad (3.97)$$

where α, n are capillary pressure curve parameters. The parameters for the matrix capillary pressure in my study were the ones for clay reported in Table 1 of Parker et al (1987). Zero capillary pressure was assumed in the hydraulic fracture.

3.7 Adsorption

In order to fully describe the behavior of organic-rich shale gas reservoirs, it is important to account for the occurrence of adsorbed gas. Adsorbed gas is stored in nanopores within the organic matter as a dense liquid-like (confined) phase. There are numerous different models describing gas adsorption-desorption processes, but for the purposes of this study, I selected the most widely used and computationally simple Langmuir isotherm (Langmuir, 1916).

Langmuir Isotherm was developed assuming a dynamic equilibrium between adsorbed and free phase at a constant pressure and temperature. Another major assumption of the model is that there is a single layer of molecules on the solid surface. The Langmuir (1916) model is described by following equation:

$$V(p) = \frac{V_L p}{p + p_L}, \quad (3.98)$$

where, $V(p)$ is the volume of gas adsorbed at pressure p, V_L and P_L are the fitting parameters, called Langmuir volume and Langmuir pressure. The physical meaning of the Langmuir volume is that it is the maximum volume of gas that can be adsorbed at infinite pressure. The Langmuir pressure refers to the pressure at which half of the Langmuir volume is adsorbed.

To incorporate the effects of adsorption into the reservoir simulator, the mass of the desorbed gas needs to be added to the mass accumulation term as proposed by Ali (2012):

$$M_G^{\kappa} = \phi S_G \rho_G X_G^{\kappa} + (1-\phi)\rho_G^{SC} V_G^{desorbed} \rho_R \,, \quad (3.99)$$

where ρ_G^{SC} is the gas density at standard conditions, $V_G^{desorbed}$ is the desorbed gas specific volume, calculated from the isotherm, and ρ_R is the rock bulk density.

3.8 Fracture Permeability Degradation

Fracture permeability degradation is modeled according to El Sgher et al. (2018). Their approach introduces a fracture conductivity multiplier tensor fitted to laboratory measurements of closure stress along the principal axis instead of performing an expensive coupling of a geomechanical simulator. The pressure-temperature dependent fracture permeability is given by:

$$k_i = k_{0,i} \exp\left[\xi_i \left(\frac{\phi}{\phi_0} - 1 \right) \right], \quad (3.100)$$

$$\phi = \phi_0 \exp\left[c_R \left(p - p_0 \right) - a_R \left(T - T_0 \right) \right], \quad (3.101)$$

where ξ is the fracture conductivity multiplier tensor.

3.9 Stencil Model and Spatial Discretization

A multi-fractured horizontal well is modeled by using the *one quarter stencil* approach (Olorode, 2011; Olorode et al., 2013), the results of which are to be later multiplied by

the number of fractures in a cluster and then by the number of clusters for the specific well. The use of the stencil was shown to be an accurate predictor of production of the entire multi-fractured horizontal well for very long periods (Olorode, 2011; Olorode et al., 2013). This approach serves my focus on modeling the flow processes from the ultra-tight reservoir interior (the matrix) to the high-permeability fracture for long production times (up to 40 years) using very high-resolution grids in order to capture the full scale of the mechanistic and non-mechanistic response. The reservoir-fracture stencil is shown in **Fig.3.5**. The position of the stencil within the horizontal well/fracture system is shown in **Fig.3.6**

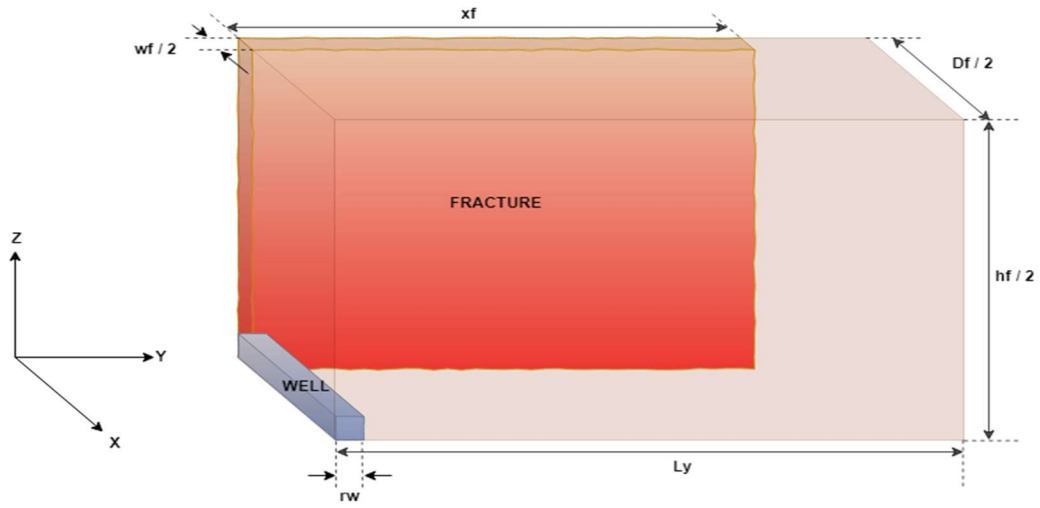

Figure 3.5 — Sketch of the stencil geometry.

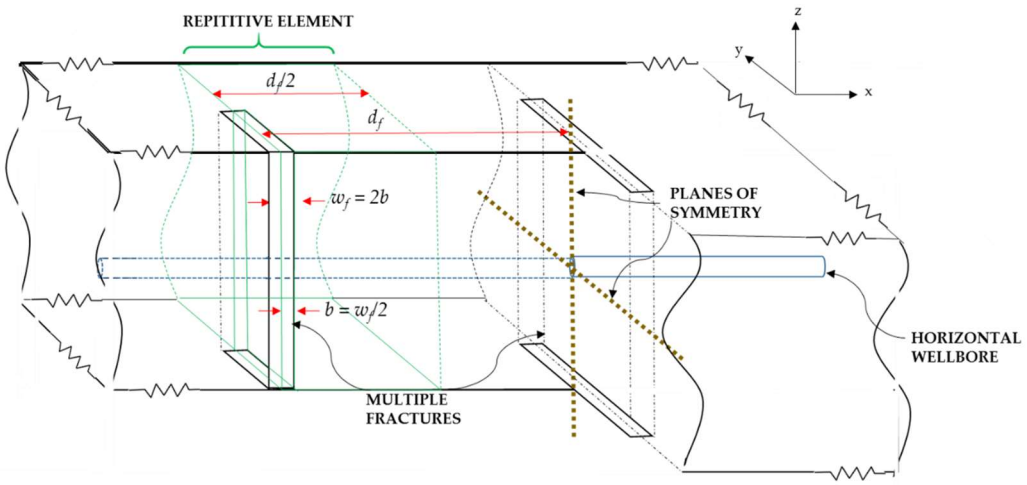

Figure 3.6 — Schematic diagram of the stencil as a repetitive element in the multi-fractured horizontal well system in a rectangular reservoir.

3.10 Numerical Implementation

The mass and heat transport of three-phase black oil and two-phase gas-water systems in porous media is fully and uniquely described by a set of primary variables that completely define the thermodynamic state of the system, as well as the distribution of mass components among the various phases. The number of the primary variables is fixed, and the type of variables serving as primary variables are specific to the thermodynamic state and the present phases for a given set of conditions.

The primary variables used in the three-phase black oil problem and in the two-phase gas-water problem are listed in **Tables 3.5** and **3.6,** respectively.

Table 3.5 — List of primary variables used in the three-phase black oil numerical simulator.

Thermodynamic State		Primary Variables
Number of Phases	Phases Present	
1	Organic	P, X_O^g, X_O^w, T
1	Aqueous	P, X_A^o, X_A^g, T
2	Aqueous, Organic	P, X_O^g, S_A, T
2	Gaseous, Organic	P, Y_G^w, S_G, T
3	Aqueous, Organic, Gaseous	P, S_A, S_G, T

Table 3.6 — List of primary variables used in the two-phase gas-water numerical simulator.

Thermodynamic State		Primary Variables
Number of Phases	Phases Present	
1	Gaseous	P, Y_G^g, T
1	Aqueous	P, X_A^g, T
2	Aqueous, Gaseous	P, S_G, T

The mass and energy balance equations defined by **Eq. 3.1** are discretized in time and space. The spatial discretization is implemented according to the integral finite difference (IFD) method [Narasimhan and Witherspoon, 1976; Pruess et al, 1999]. Introducing the volume average V_n and the volume averaged mass (or heat) M_n, the integral of accumulation terms in **Eq. 3.1** becomes:

$$\int_{V_n} M^\kappa dV = V_n M_n \quad \text{.....(3.102)}$$

The use of the IFD method allows the equation of the surface integral of flux in **Eq. 3.1** by the algebraic sum of the individual fluxes through the surface area A_{nm} of the connection of elements *n* and *m* as follow:

$$\int_{\Gamma_n} F^{\kappa} \cdot \overline{n}\, d\tilde{A} = \sum_m A_{nm} F_{nm} \,. \qquad (3.103)$$

The averaged flux term in **Eq. 3.103** is obtained in the following manner:

$$F_{\beta,nm} = -k_{nm} \left[\frac{k_{r\beta}\rho_{\beta}}{\mu_{\beta}} \right]_{nm} \left(\frac{P_{\beta,n} - P_{\beta,m}}{D_{nm}} - \rho_{\beta,nm} g_{nm} \right), \qquad (3.104)$$

where the subscript *mn* denotes the upstream weighting of the mobilities, permeabilities and densities at the connection interface between the adjacent elements, D_{nm} is the distance between the element centers and g_{nm} is the adjusted gravity vector in the direction from *m* to *n*.

Substitution of **Eqs. 3.102-3.104** into **Eq. 3.1** results in a set of spatially discretized ordinary differential equations in time given by:

$$\frac{d}{dt} M_n^{\kappa} = \frac{1}{V_n} \sum_m A_{nm} F_{nm}^{\kappa} + q_n^{\kappa} \,. \qquad (3.105)$$

The time in the time derivative of Eq. 3.105 is discretized using a first-order backward finite-difference scheme.

All the variables on the right-hand side of **Eq. 3.105** are evaluated at the new (current) timestep $t^{k+1} = t^k + \Delta t$. The time discretization in **Eq. 3.105** results in the following set of coupled algebraic equations:

$$R_n^{k+1} = M_n^{\kappa,k+1} - M_n^{\kappa,k} - \frac{\Delta t}{V_n}\sum_m A_{nm} F_{nm}^{\kappa,k+1} - \Delta t\, q_n^{\kappa,k+1}, \quad \text{.....(3.106)}$$

where R_n^{k+1} is the residual. N_E elements and N_x equations per element result in a system of $N_E \times N_x$ coupled non-linear equations in the form of **Eq. 3.106**.

In the fully implicit scheme I used in my simulator, the system of equations at time t^{k+1} is solved for the $N_E \times N_x$ primary variables by Newton-Rhapson iteration. Introducing the iteration index p, I expand the residuals in **Eq. 3.106** at iteration step p+1 in a Taylor series as follows:

$$R_n^{\kappa,k+1}\left(x_{i,p+1}\right) = R_n^{\kappa,k+1}\left(x_{i,p}\right) + \sum_i \left.\frac{\partial R_n^{\kappa,k+1}}{\partial x_i}\right|_p \left(x_{i,p+1} - x_{i,p}\right) + \ldots = 0 \text{ . .....(3.107)}$$

Discarding all higher-order terms, **Eq. 3.107** yields the following linear system:

$$-\sum_i \left.\frac{\partial R_n^{\kappa,k+1}}{\partial x_i}\right|_p \left(x_{i,p+1} - x_{i,p}\right) = R_n^{\kappa,k+1}\left(x_{i,p}\right), \quad \text{.....(3.108)}$$

where the $\partial R_n^{\kappa,k+1} / \partial x_i$ terms represent the derivatives in the resulting Jacobian matrix and are evaluated by numerical differentiation.

The linear system in **Eq. 3.108** is solved by the Bi-Conjugate Gradient Stabilized (BiCGStab) iterative sparse matrix method with an incomplete-LU preconditioner. These are implemented in Compute Unified Device Architecture (CUDA) and GPU-parallelized.

CHAPTER IV

MECHANISTIC MODEL VALIDATION AND RESULTS

In this section I demonstrate the mechanistic model response to (a) a typical three-phase flow to a horizontal multi-fractured well in the Wolfcamp formation and (b) a typical two-phase gas and water flow to a horizontal multi-fractured well in the Marcellus formation and how the results are affected by the non-mechanistic processes.

To validate the mechanistic mode, I compared the simulation results to the analytical solution of Olarewaju and Lee (1989). The comparison plot for the typical three-phase black-oil flow case is shown on **Fig. 4.1**. The comparison plot for the typical two-phase dry gas flow case is shown on **Fig. 4.2**. The complete tables of input parameters as well as initial and boundary conditions for the cases shown on **Figs. 4.1-4.2** can be found in **Appendix A**.

The results in **Figs. 4.1** and **4.2** indicate that the 2D numerical solution matches the analytical solution perfectly for both the black oil and the dry gas cases. However, the 3D numerical solutions differ from the analytical solution in the early-time behavior. The difference is caused by the assumption of the trilinear flow and the model geometry in the analytical solution: the trilinear model assumes 3 independent 1D linear flows and was developed for vertical wells, thus it cannot account for flow in the vertical direction and the more complex flows that deviate from the assumption of independent 1D flows that occur in the stencil model. Note that the analytical solution cannot account for gravitational and capillary pressure effects.

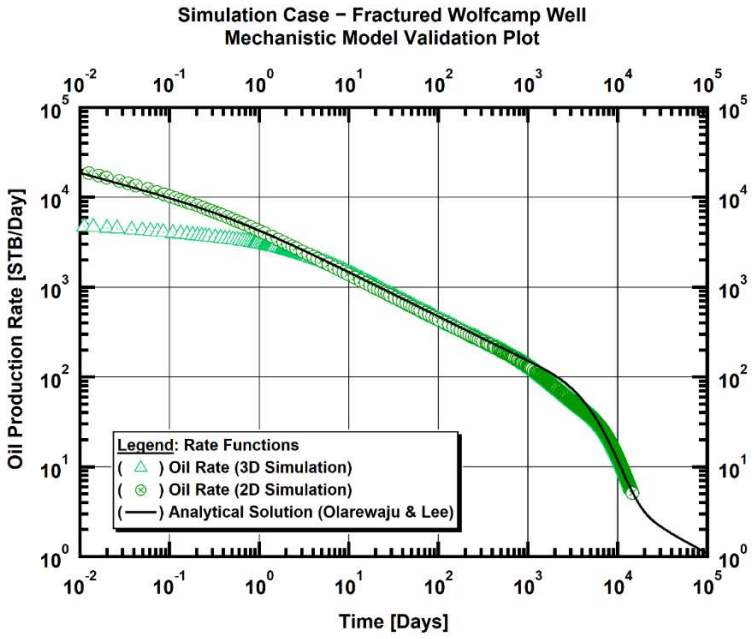

Figure 4.1 —Log-log mechanistic model validation plot for three-phase black oil flow in the Wolfcamp shale.

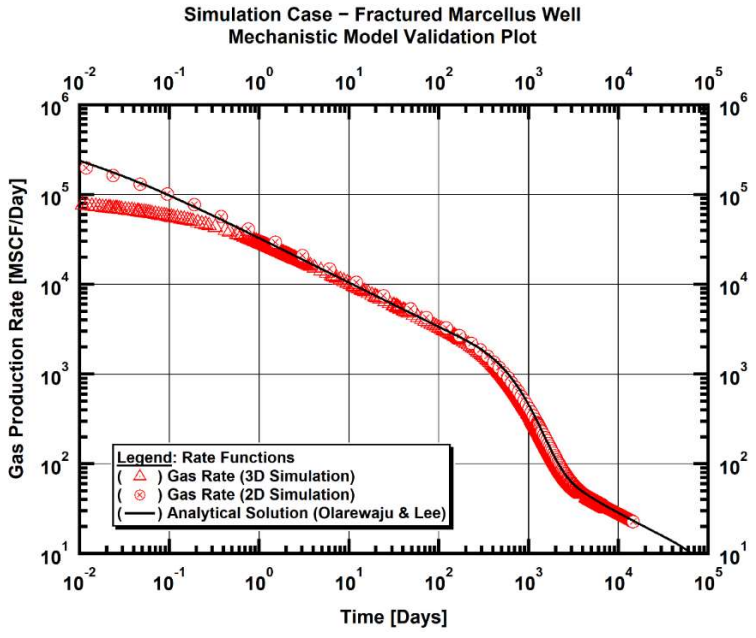

Figure 4.2 —Log-log mechanistic model validation plot for two-phase dry gas flow in the Marcellus shale.

Four flow regimes can be observed from the mechanistic model validation plots, three of which are validated against the analytical solution. The modeled flow regimes are:

- The *early-time fracture-dominated flow* (*i.e.,* fracture unloading). This flow regime is not present in the analytical solution or in the 2D simulation, as both of them fail to model the effects of gravity, flow in the vertical direction and more complex 3D flows.
- The *linear flow* regime (*i.e.,* non-interfering fractures) is modeled and validated against the analytical solution.
- The *late-time boundary-dominated flow* regime is modeled and validated against the analytical solution. However, the simulation cases show a short transitional period before converging to the analytical solution.
- The *late-time compound linear* flow regime is modeled and validated against the analytical solution.

Having validated the mechanistic model, I can now use it to study the characteristic behavior of multi-phase fluid flow to a multi-fractured horizontal well in unconventional reservoirs.

4.1 Three-Phase Black Oil Case

Here I demonstrate the mechanistic model behavior in the simulation of a case of a typical three-phase black oil flow to a multi-fractured horizontal well in the Wolfcamp shale. **Fig. 4.3** shows the plot of the evolution of the phase production rates in the base case that involved the fracture and well-spacing design listed in **Appendix A** (**Table A4**). Note that wells in the Wolfcamp formation are known to have high water production rates. I made two different runs of the base case using the highest resolution grid (the grid

description is provided in **Appendix A**) to determine if the high initial water saturation affects the characteristic behavior. The first run (**Fig. 4.3**) was made with an initial water saturation of $S_w = 0.4$, and in the second run $S_w = 0.5$ (**Fig. 4.4**).

As can be seen from the **Figs. 4.3-4.4**, the increase in the initial S_w affects the overall phase production rates, and especially the water production rate which is almost 5 times higher when S_w increases from $S_w = 0.4$ to $S_w = 0.5$. However, the characteristic behavior remains unchanged in both cases, the observed flow regimes are the same and the transition points are also the same. Consequently, I continued the study with the $S_w = 0.4$ reference case in order to investigate a more general problem: because other unconventional plays do not have such high water cuts, the observations of the model can be extended to other plays.

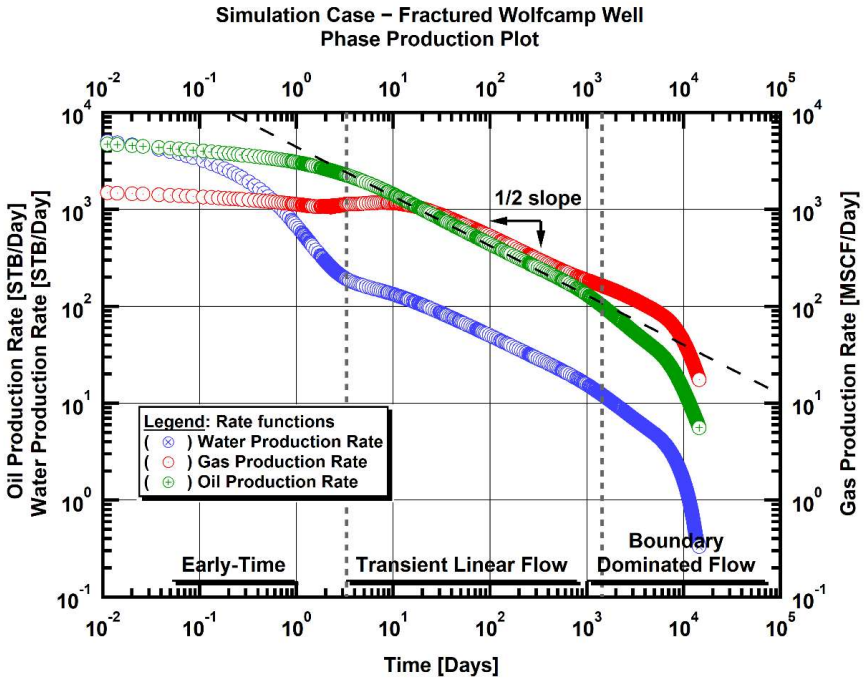

Figure 4.3 —Log-log phase plot of the evolution of the phase production rates in the base case of three-phase black oil flow in the Wolfcamp shale (S_w = 0.4).

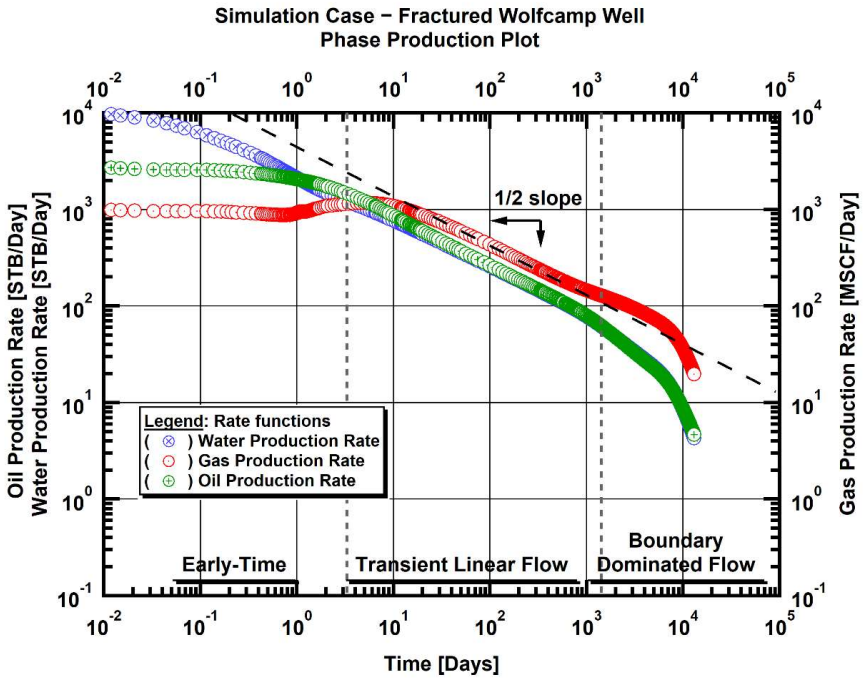

Figure 4.4 —Log-log phase plot of the evolution of the phase production rates in the case of three-phase black oil flow in the Wolfcamp shale (S_w = 0.5).

I continued the study of the mechanistic model by investigating the well and fracture spacing effect on production. For this purpose, I constructed a number of different geometry grids, described in **Appendix A**, and used them to quantify their effects on the simulation results in runs that kept all the reservoir and fluid properties unchanged from the base case.

Fig. 4.5 shows the plot of the phase rate evolution over time for the Wolfcamp problem obtained with Mesh B. In this figure, the reservoir behaves as an infinite-acting system for the first 40 years of production when the cluster spacing is 130 ft (vs. a 50 ft cluster spacing in the base case). Consequently, there is no need to investigate larger cluster

spacing as the boundary-dominated flow does not emerge in 40 years of production. A comparison to the base case in **Fig. 4.3** indicates that cluster spacing strongly affects the late-time behavior.

Fig. 4.6 shows the plot of the phase rate evolution over time for the Wolfcamp problem obtained with Mesh C, which differs from Mesh B in the stencil height, which is 50 ft in Mesh C and 130 ft in Mesh B. The behavior of the rate functions is consistent with those in an infinite acting reservoir, with the only difference from the Mesh B case in the early-time behavior. The *bi-linear flow* regime is evident in **Fig. 4.6** and is validated against the Lee and Brockenbrough (1986) analytical solution for an infinite-acting reservoir. The conclusion to be drawn from this study is that (a) the pay-zone height affects mainly the early-time behavior, and (b) there is no need for numerical simulation when the reservoir height is lower than 50 ft because the solution converges to the 2D solution and can be adequately resolved by the analytical solution.

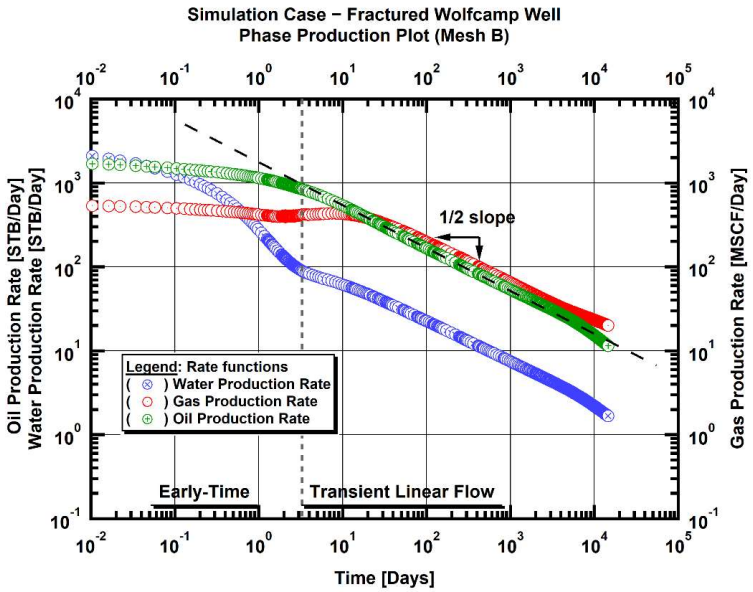

Figure 4.5 —Log-log phase plot of the evolution of the phase production rates in the case of three-phase black oil flow in the Wolfcamp shale (Mesh B, 130-ft cluster spacing, 150 ft pay zone height).

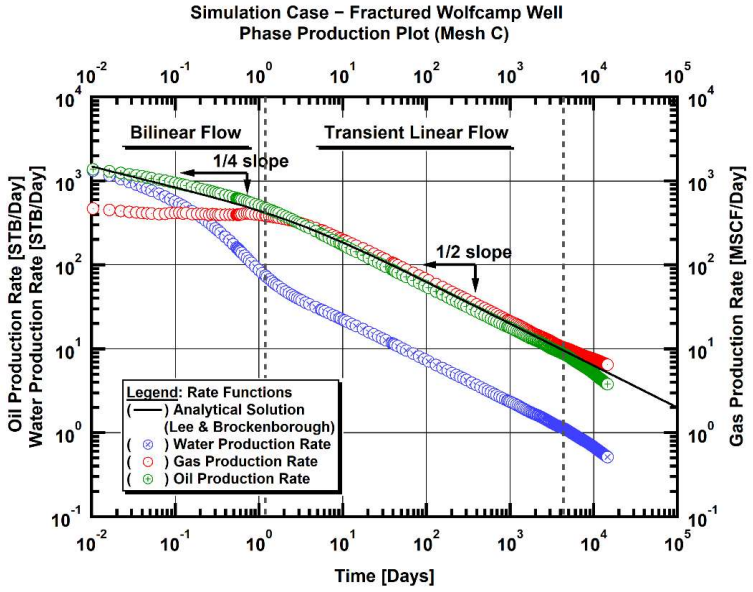

Figure 4.6 —Log-log phase plot of the evolution of the phase production rates in the case of three-phase black oil flow in the Wolfcamp shale (Mesh C, 130-ft cluster spacing, 50 ft pay zone height).

Having established the geometric boundaries of investigation, I then conducted an analysis of the sensitivity of the oil production rate behavior to the cluster spacing, in order to determine the exact relationship with the end of linear flow. To avoid the error introduced by the multiplication by the number of fractures and clusters in the horizontal well system, I conducted the sensitivity analysis using a single stencil. I introduced the dimensionless aspect ratio parameter, which is described by:

$$y_{eD} = \frac{y_e}{x_f} \quad \text{.....(4.1)}$$

In the stencil coordinate system, the same parameter is defined as:

$$y_{eD} = \frac{D_f}{2x_f} \quad \text{.....(4.2)}$$

The sensitivity of the oil rate to the aspect ratio is shown on **Fig. 4.7**. The variable input parameters for this sensitivity analysis are listed in **Table 4.1**. The simulation results confirm the earlier observation (**Fig. 4.5**) that the aspect ratio only affects the time at which linear flow ends in this single-fracture system. The same conclusion can be reached by analyzing the analytical solutions of Ozkan and Raghavan (1988) and Olarewaju and Lee (1989).

The dimensionless stencil height is defined by:

$$h_{eD} = \frac{h_f}{2x_f} \quad \text{.....(4.3)}$$

The sensitivity of the oil production rate to the dimensionless stencil height is described in **Fig.4.8**. The values of the dimensionless stencil height used in this sensitivity analysis are listed in **Table 4.2**.

Fig. 4.8 shows that the initial oil production rate increases with an increasing stencil height, which is rather obvious and is generalized by the use of dimensionless variables, as a fully-penetrating fracture is considered. However, there is an early-time effect that cannot be explained by the use of dimensionless variables, or by analytical solutions. This effect is caused by vertical flow inside the fracture and acts as a skin, limiting early-time performance.

The vertical flow effect needs to be investigated more thoroughly, and perhaps accounted for (if possible) in an analytical model, as it may distort the shut-in well test results in fractured wells. Note that, although this effect occurs only at very early times, it may be exaggerated in lower conductivity fractures.

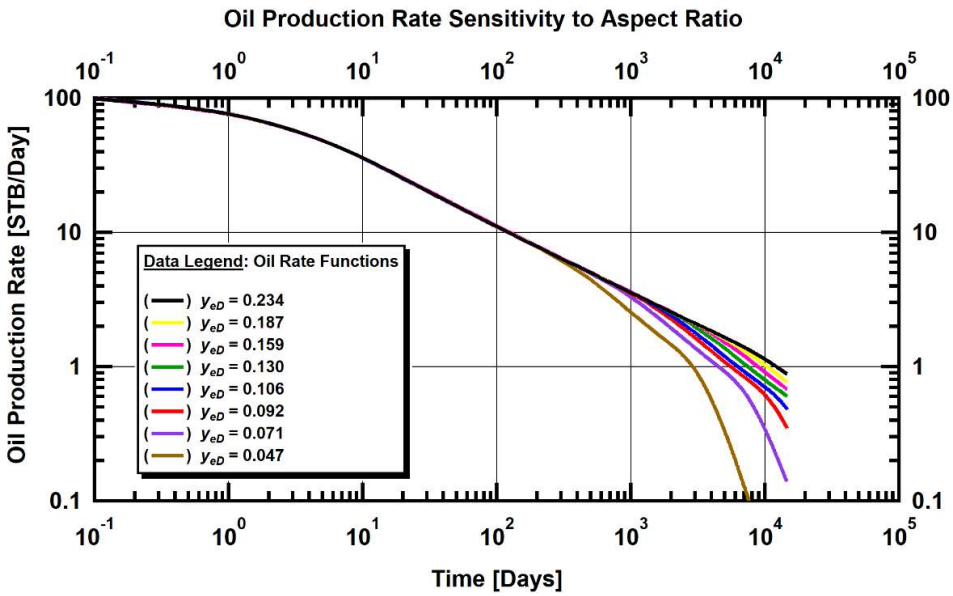

Figure 4.7 —Log-log plot of sensitivity of the oil production rate to the cluster spacing in the problem of the three-phase black oil flow problem in the Wolfcamp shale.

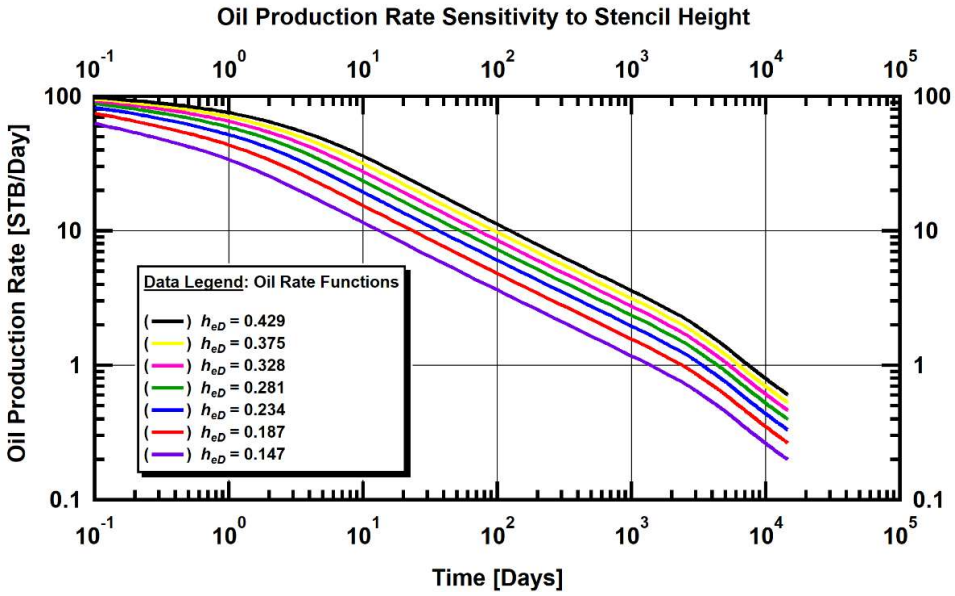

Figure 4.8 —Log-log plot of sensitivity of the oil production rate to the reservoir thickness in the problem of the three-phase black oil flow problem in the Wolfcamp shale.

Table 4.1 — Aspect ratio inputs for the sensitivity analysis studies in the three-phase black oil problem in the Wolfcamp shale.

y_e (m)	x_f (m)	y_{eD} (Dimensionless)
25.00	106.68	0.234
20.32	106.68	0.190
20.00	106.68	0.187
16.93	106.68	0.159
13.85	106.68	0.130
11.29	106.68	0.106
10.51	106.68	0.099
9.83	106.68	0.092
7.62	106.68	0.071
5.00	106.68	0.047

Table 4.2 — Stencil height inputs for the sensitivity analysis studies in the three-phase black oil flow problem in the Wolfcamp shale.

$h/2$ (m)	x_f (m)	h_{eD} (Dimensionless)
15.00	106.68	0.141
20.00	106.68	0.187
25.00	106.68	0.234
30.00	106.68	0.281
35.00	106.68	0.328
40.00	106.68	0.375
45.72	106.68	0.429

Analytical solutions do not provide any parameters that might describe the late time behavior of the production rate, other than the aspect ratio and the parameters included in the dimensionless time. To investigate the possible effects of the oil composition on the terminal decline behavior, I investigated the sensitivity of the oil production rate to the initial gas content, as quantified by the gas-oil ratio (GOR). The results for the GOR values listed in **Table 4.3** are shown in **Fig. 4.9**, and lead to the conclusion that an increasing GOR is associated with a higher oil production rate. The effect of the dissolved gas on the properties of the organic phase can be accounted for by correcting the total compressibility of the fluid.

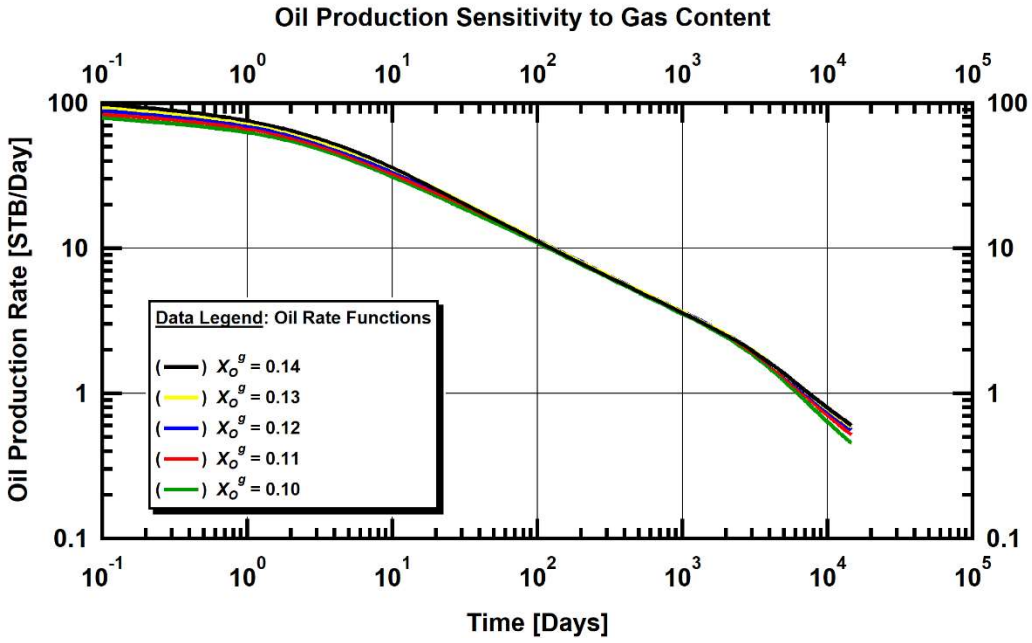

Figure 4.9 —Log-log plot of sensitivity of the oil production rate to the GOR in the problem of the three-phase black oil flow problem in the Wolfcamp shale.

Table 4.3 —Dissolved gas (GOR) inputs for the sensitivity analysis studies in the three-phase black oil flow problem in the Wolfcamp shale.

X_O^g (kg/kg)	R_S (scf/STB)
0.100	752.68
0.110	837.27
0.120	923.79
0.130	1012.30
0.140	1102.88

4.2 Two Phase Dry Gas Case

Here I demonstrate the performance of the mechanistic model in the study of the typical problem of two-phase dry gas flow to a multi-fractured horizontal well in the Marcellus shale. The simulator inputs, grid specifications along with initial and boundary conditions can be found in **Appendix A**.

The cluster spacing in this case is 50 ft, i.e., the same as in the Wolfcamp base case described in **Fig. 4.3**. The gas production rate in **Fig. 4.10** reaches (a) the boundary-dominated flow regime after one year of production and (b) the compound linear flow regime after approximately eight years of production, indicating that the cluster spacing in this gas base case is too small.

For a better resolution of the production behavior, I used the Mesh B (with a cluster spacing of 130 ft) discussed in the study of **Fig. 4.5**. The corresponding results are presented on **Fig. 4.11**, and show that (a) the boundary-dominated flow is reached in a little over three years of production and (b) the compound linear flow does not evolve in forty years.

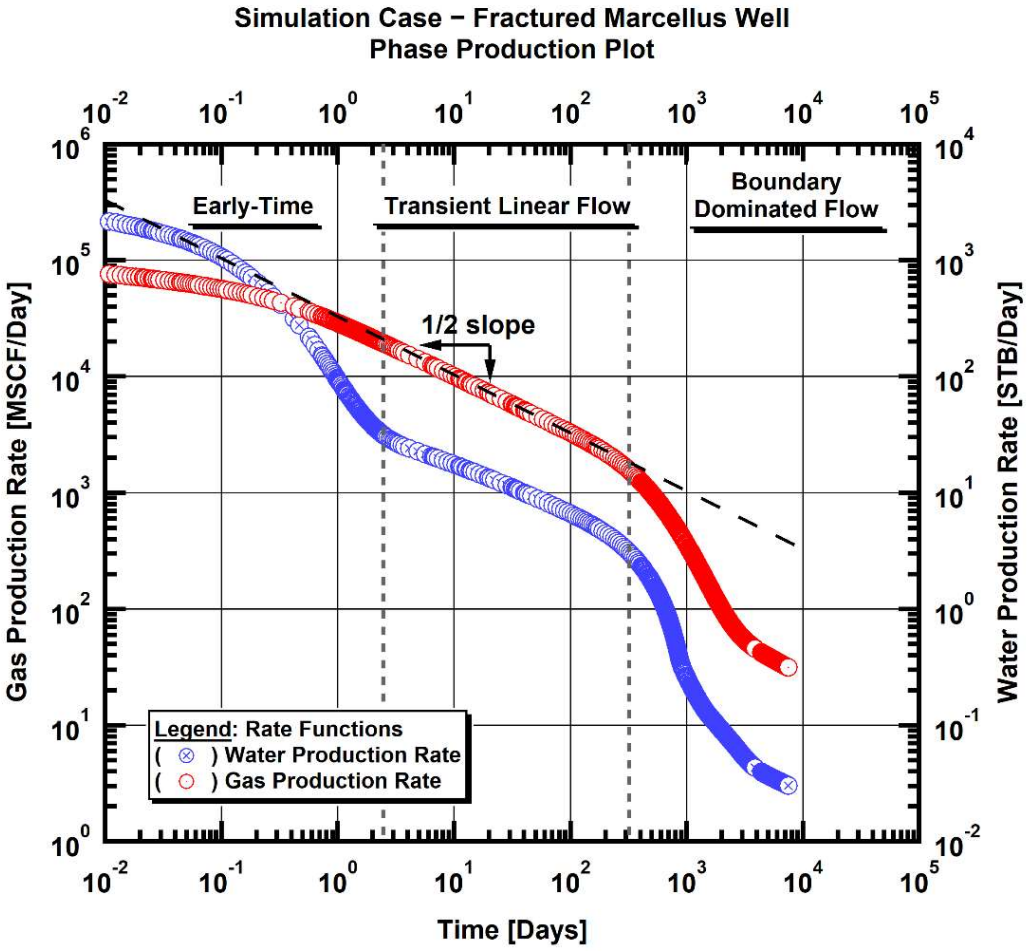

Figure 4.10—Log-log phase plot of the evolution of rate over time in the two-phase gas-water flow problem in the Marcellus shale.

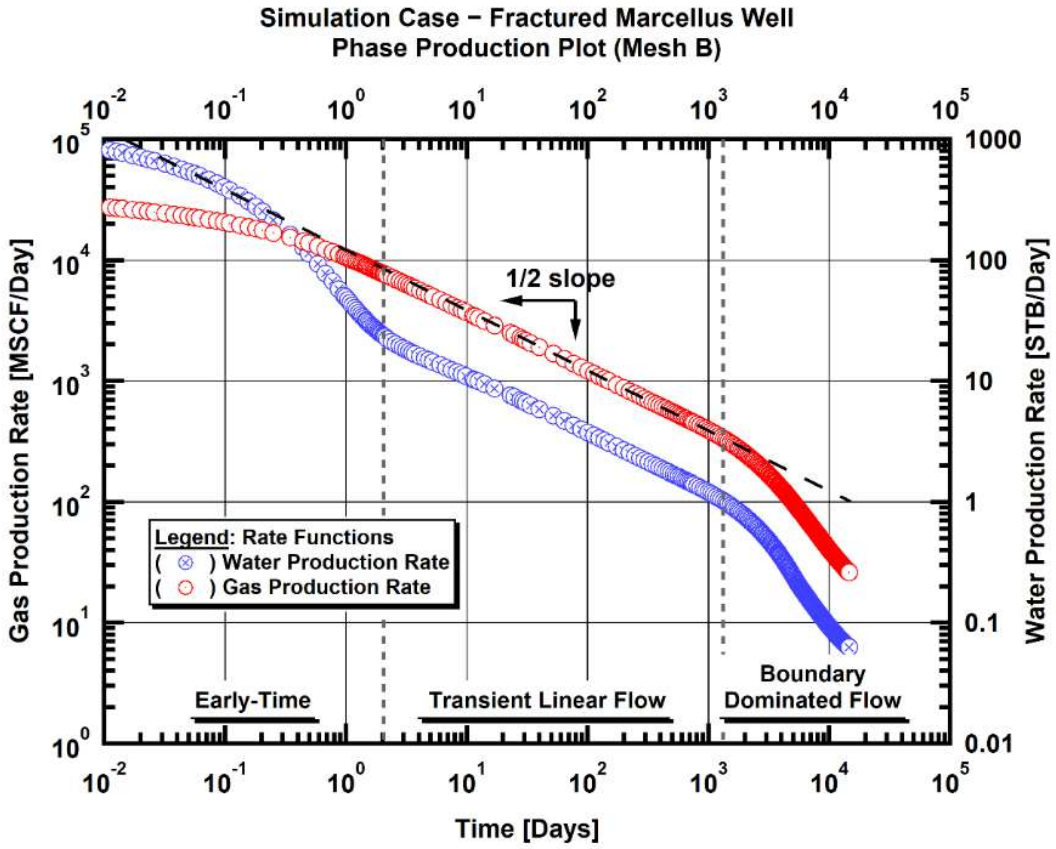

Figure 4.11—Log-log phase plot of the evolution of the phase production rates in the case of two-phase gas flow problem in the Marcellus shale (Mesh B, 130-ft cluster spacing, 75 ft pay zone height).

Following the same approach discussed in the three-phase black flow problem, I first conducted an analysis of the sensitivity of production to the aspect ratio using as a basis the stencil domain. The aspect ratios that were used as the inputs in this sensitivity analysis study are listed in **Table. 4.4**, and the corresponding plots are shown in **Fig. 4.12**. Compared to the oil case (**Fig. 4.7**), the aspect ratio has a stronger effect in the two-phase gas problem, and this is attributed to the higher compressibility of the gas. Another

difference from the black oil case is the absence of a transitional period between the linear flow regime and the boundary-dominated flow regime.

Fig. 4.13 shows the sensitivity of the gas production rate to the fracture permeability. The fracture permeability inputs used in the sensitivity analysis are listed in **Table. 4.5**. The solutions of the mechanistic numerical model agree well with the analytical solutions in the sense that fracture permeability only affects early time behavior, which in our case lasts less than one day.

Fig. 4.14 shows the sensitivity of the gas production rate to the reservoir temperature. Because all of the analytical solutions used in this study are isothermal, it is interesting to investigate the temperature effect on production. It is evident from **Fig. 4.14** that the effect of the temperature on gas production is minor, consequently, it will not be investigated further.

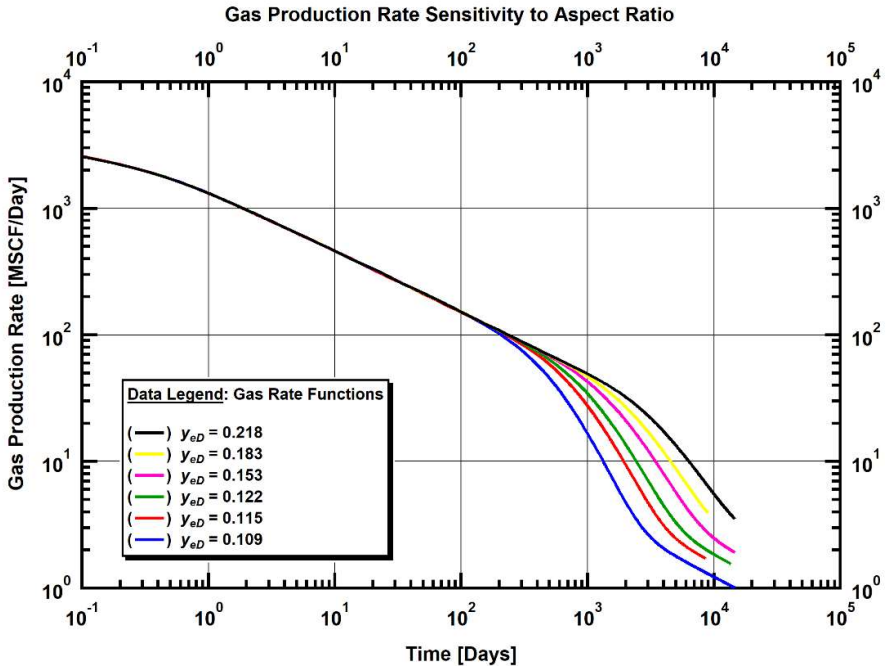

Figure 4.12—Log-log plot of sensitivity of the gas production rate to the aspect ratio in the problem of the two-phase gas flow problem in the Marcellus shale.

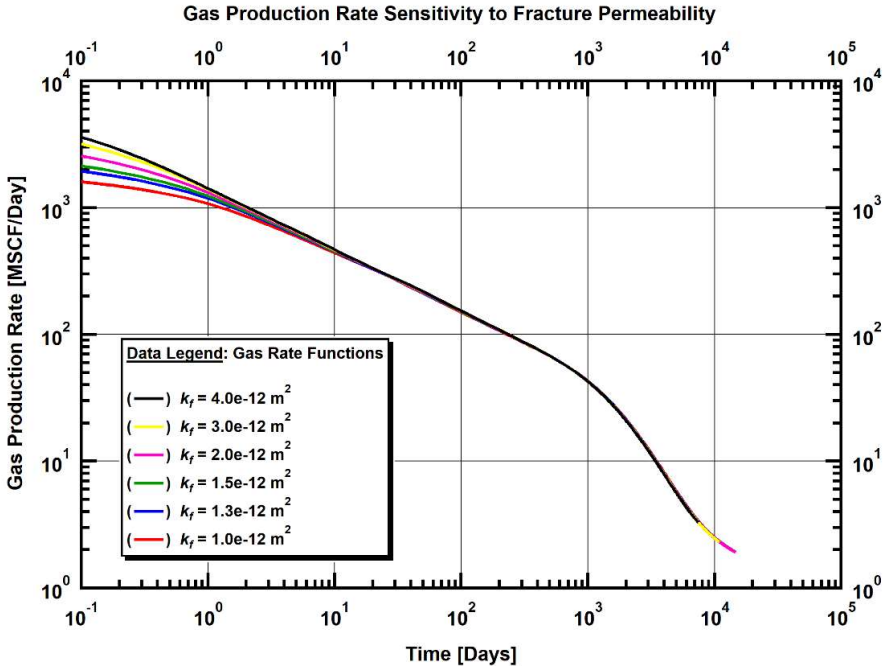

Figure 4.13—Log-log plot of sensitivity of the gas production rate to the fracture permeability in the two-phase gas flow problem in the Marcellus shale.

Table 4.4 — Aspect ratio inputs for the sensitivity analysis studies in the two-phase gas-water flow in the Marcellus shale.

y_e (m)	x_f (m)	y_{eD} (Dimensionless)
20.96	91.44	0.229
20.00	91.44	0.219
16.76	91.44	0.183
13.97	91.44	0.153
11.18	91.44	0.122
10.48	91.44	0.115
9.86	91.44	0.108
7.62	91.44	0.083

Table 4.5 — Aspect ratio inputs for the sensitivity analysis studies in the two-phase gas-water flow in the Marcellus shale.

k_f (m^2)	k_f (mD)	C_{fD} (Dimensionless)
4.00E-12	4053.00	379.12
3.00E-12	3039.75	284.34
2.00E-12	2026.50	189.56
1.50E-12	1519.87	142.17
1.30E-12	1317.22	123.21
1.00E-12	1013.25	94.78

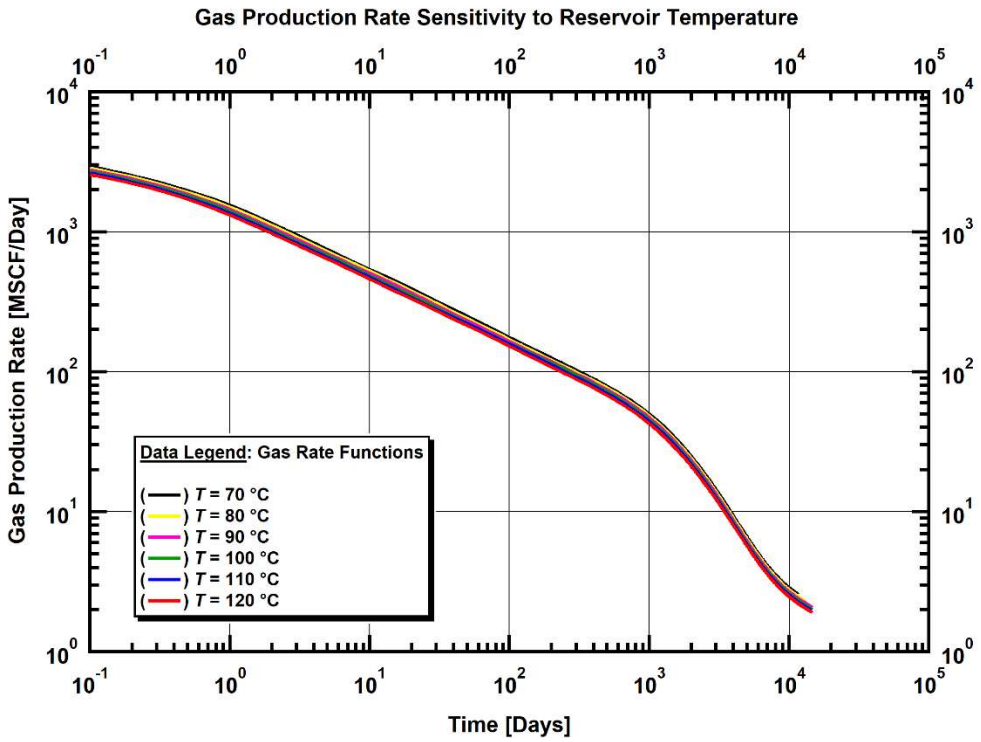

Figure 4.14—Log-log plot of sensitivity of the gas production rate to the temperature in the two-phase gas flow problem in the Marcellus shale.

4.3 Effect of Water-filled Fracture

In this section I investigate the non-mechanistic scenario of the effect of a water-filled fracture. In order to model the water-filled fracture, the saturation in the hydraulic fracture medium in the stencil was initialized with $S_w = 0.8$ initial water saturation. The production rates of the various phases with an initially the water-filled fracture are shown on **Fig.4.15**, which shows that the effect of the water-filled fracture is very significant at early times, when it causes a high water cut and reduces the oil and gas production during the first day.

Fig. 4.16 better demonstrates the overall effect of the water-filled fracture by comparing the associated phase production rates to those in the base case of **Fig. 4.3**. The two sets of the phase production curves converge after the first five days of production, which means that (a) the effect of the water-filled fracture is temporary and present only at very early-times and, consequently, (b) it can be ignored in long-term simulations.

Note that the case of the water-filled fracture is more computationally intensive compared to the base case because of the strong non-linearities in the numerical solution. Another disadvantage of this case is that it requires an extra initialization operation for the fracture.

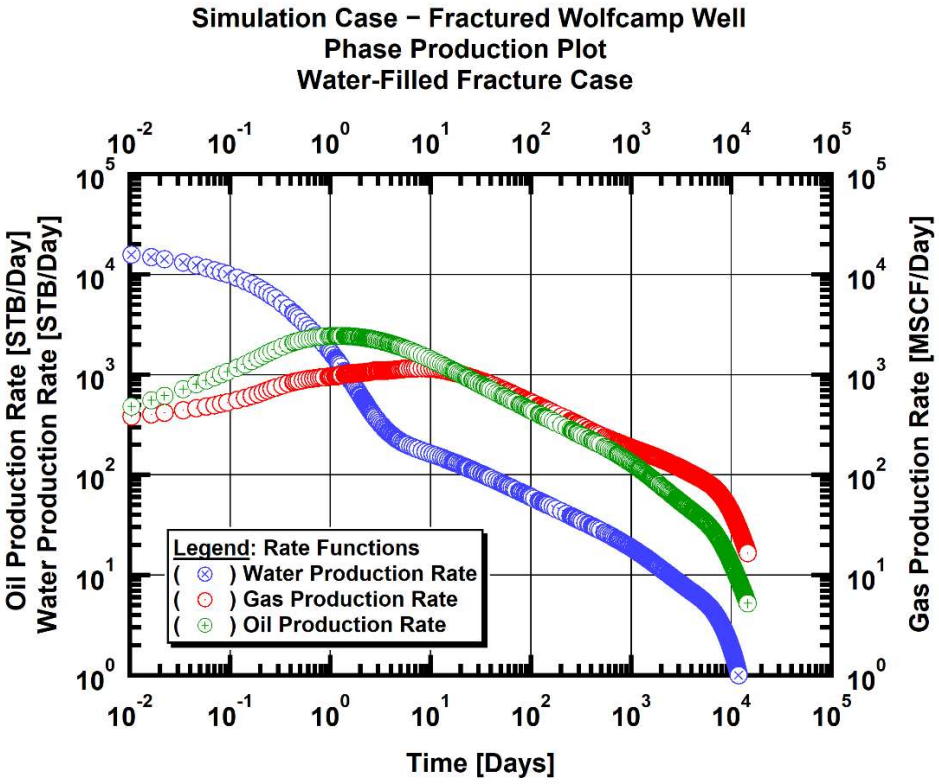

Figure 4.15—Log-log plot of the evolution over time of the phase production rates in the three-phase black oil flow problem in the Wolfcamp shale (water-filled fracture case).

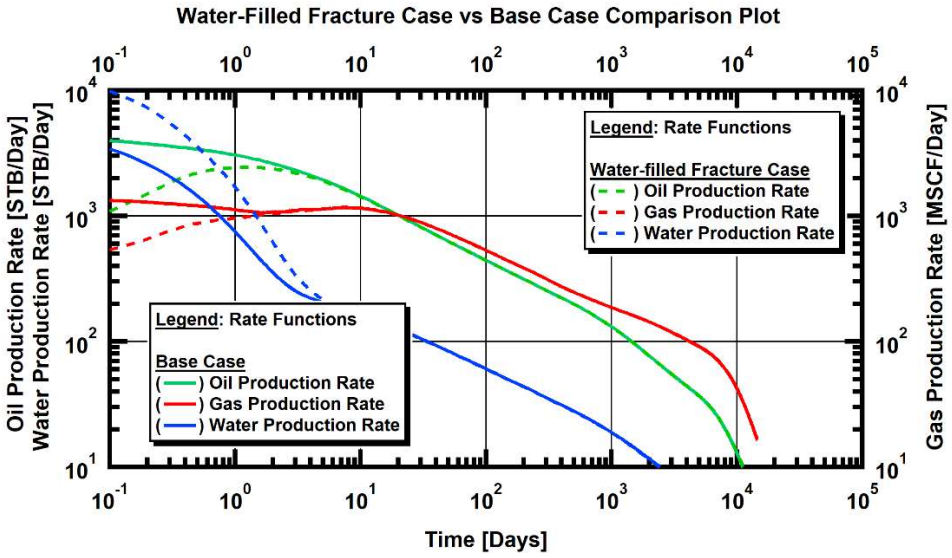

Figure 4.16—Log-log plot for the comparison of the evolution over time of the phase production rates of the base case and of the water-filled fracture case in the three-phase black oil flow problem in the Wolfcamp shale.

4.4 Effect of Fracture Degradation

Another non-mechanistic scenario I considered was the degradation of the fracture permeability. To investigate this effect on the phase production rates, I applied an anisotropic pressure-dependent permeability multiplier function to the fracture media. The results for the three-phase black oil case are presented on **Fig. 4.17**, and are compared to those in the base case in **Fig. 4.18**. The analogous results for the two-phase gas-water case are presented in **Figs. 4.19** and **4.20**, respectively.

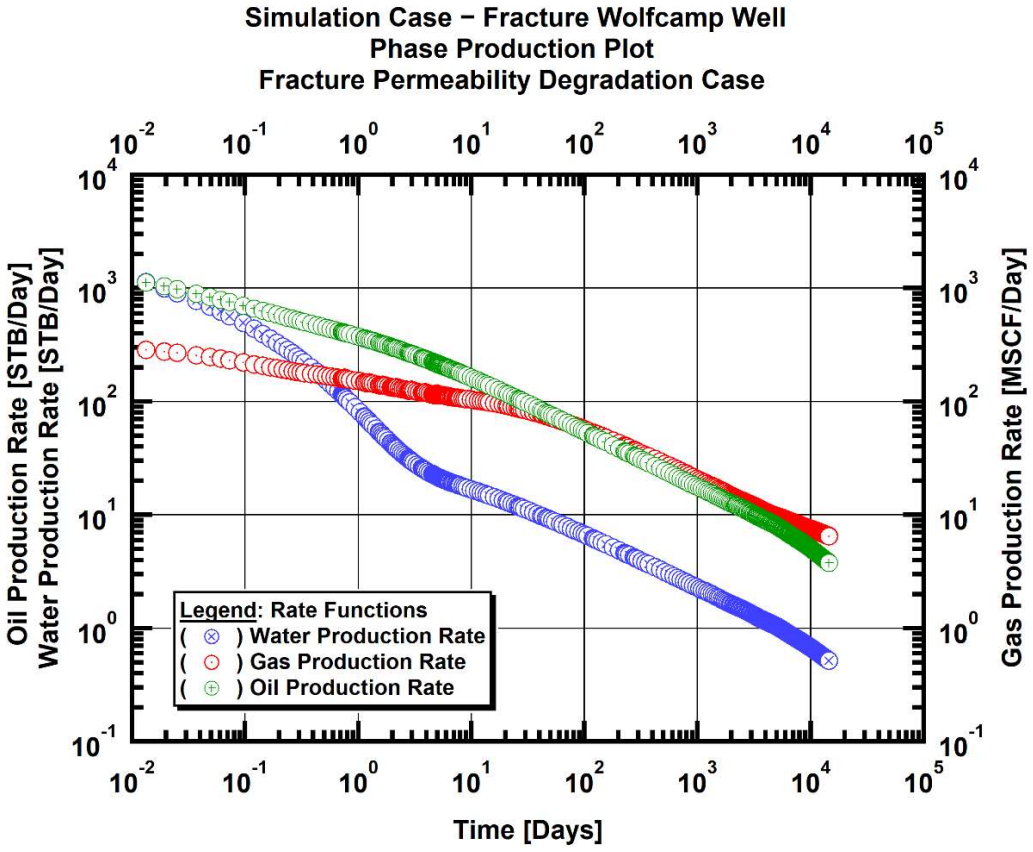

Figure 4.17—Log-log plot of the evolution over time of the phase production rates in the three-phase black oil flow problem in the Wolfcamp shale (fracture permeability degradation case).

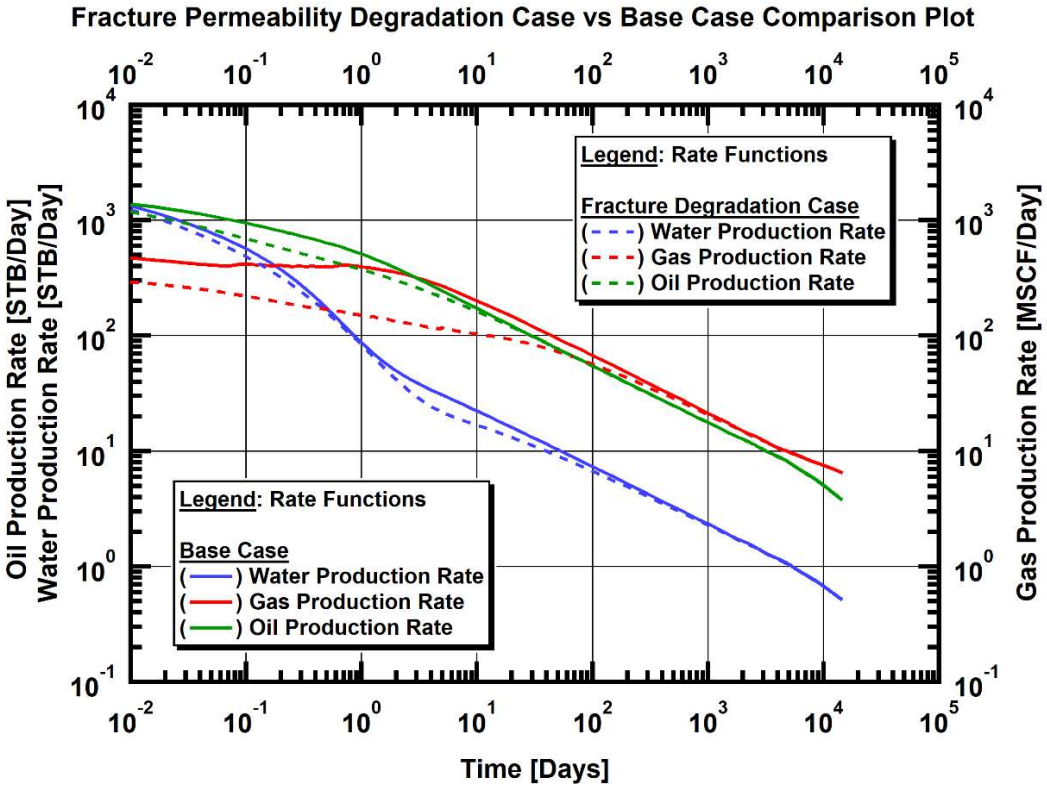

Figure 4.18—Log-log plot for the comparison of the evolution over time of the phase production rates of the base case and of the fracture permeability degradation case in the three-phase black oil flow problem in the Wolfcamp shale.

From **Fig. 4.18** shows that the effect of the fracture permeability degradation on the oil production rate is not significant, and that this production rate converges to that in the base case in the first ten days. The effect on water production rate is not very strong and converges to the base case in about 100 days. Conversely, the gas flow rate is significantly lower than that in the base case during first 100 days of production, and this is attributed to the higher compressibility of the fracture medium.

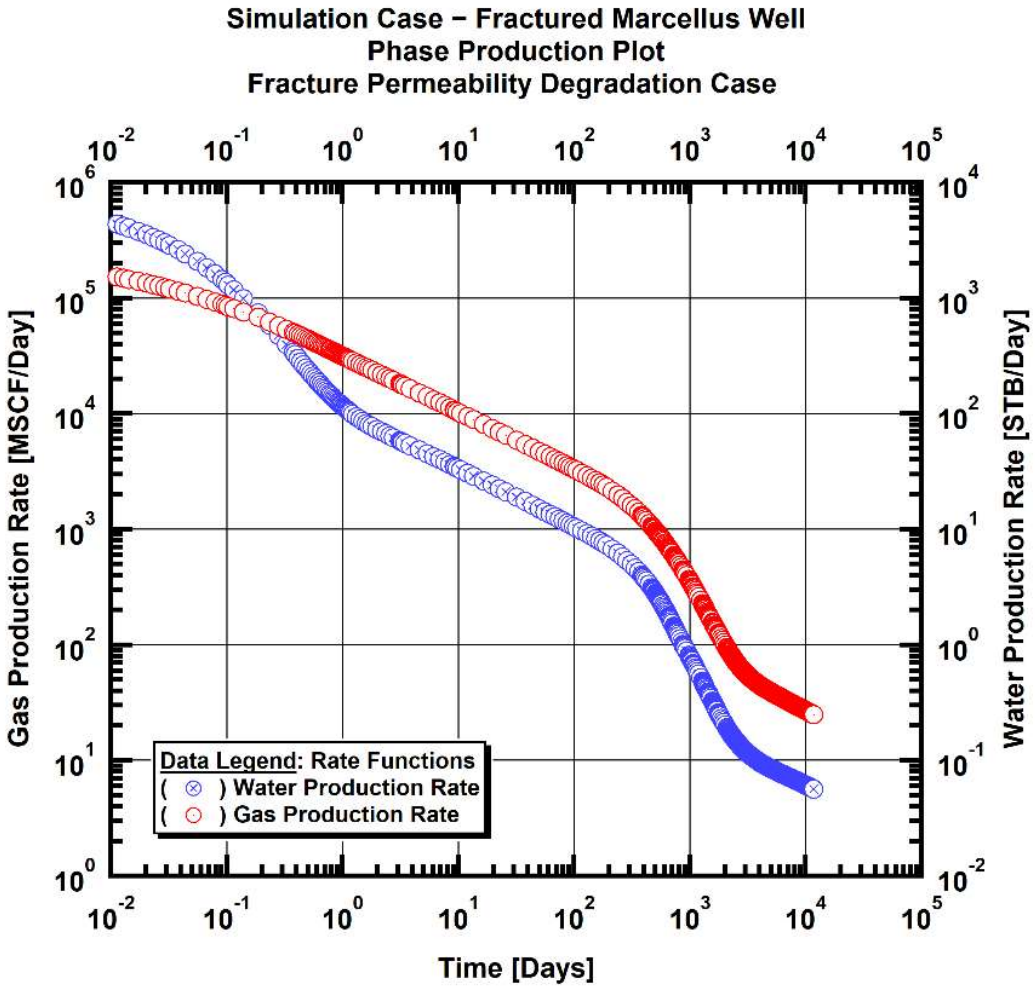

Figure 4.19—Log-log plot of the evolution over time of the phase production rates in the two-phase gas flow problem in the Marcellus shale (fracture permeability degradation case).

Fig. 4.20 slows slight differences in the production rates between the two sets of solutions change during the first 2 to 10 days of production. The effect is less significant than that in in the black-oil problem because in the oil case the fracture compressibility was eight times higher than the matrix compressibility, while in the gas problem they were the same. From these results, I concluded that the fracture-permeability degradation

does not affect the late-time behavior of the system and, therefore, is not a relevant factor for further investigation in the decline curve validation study.

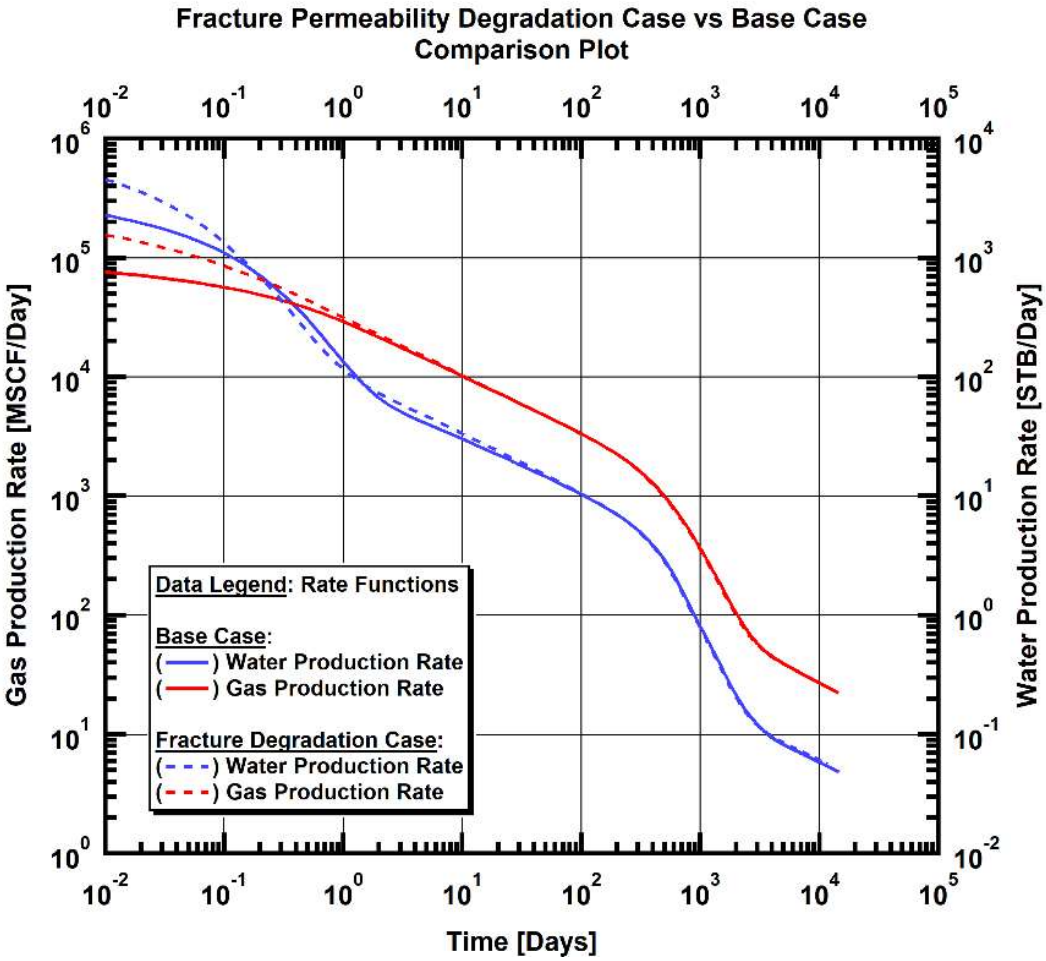

Figure 4.20—Log-log plot for the comparison of the evolution over time of the phase production rates of the base case and of the fracture permeability degradation case in the two-phase gas flow problem in the Marcellus shale.

4.5 Effect of Non-Darcy Flow

The effect of non-laminar (turbulent) flow was modeled by the Forchheimer equation (**Eq.3.83**). In the problem of multiphase flow to a multi-fractured horizontal well, the Forchheimer flow is expected to have an effect at high flow velocities during the early-time fracture depletion. To test this assumption and the overall impact of Forchheimer flow on the numerical solution, I analyzed the mechanistic model response.

The production profile for the two-phase gas-water flow in the Marcellus shale is presented on **Fig. 4.21**, and the comparison to the base case in **Fig. 4.22**. **Fig.4.22** confirms the assumption of early-time occurrence of Forchheimer gas flow, and indicates that its effect acts like a skin, limiting the flow to the wellbore. After approximately 20 days of production, the effect disappears and the numerical solution of Forchheimer flow converges to that in the base case.

I did not test the effect of Forchheimer gas flow in the three-phase black oil problem because of its high-computational cost, and because there is no reason to think that the three-phase problem would behave significantly differently from the two-phase problem.

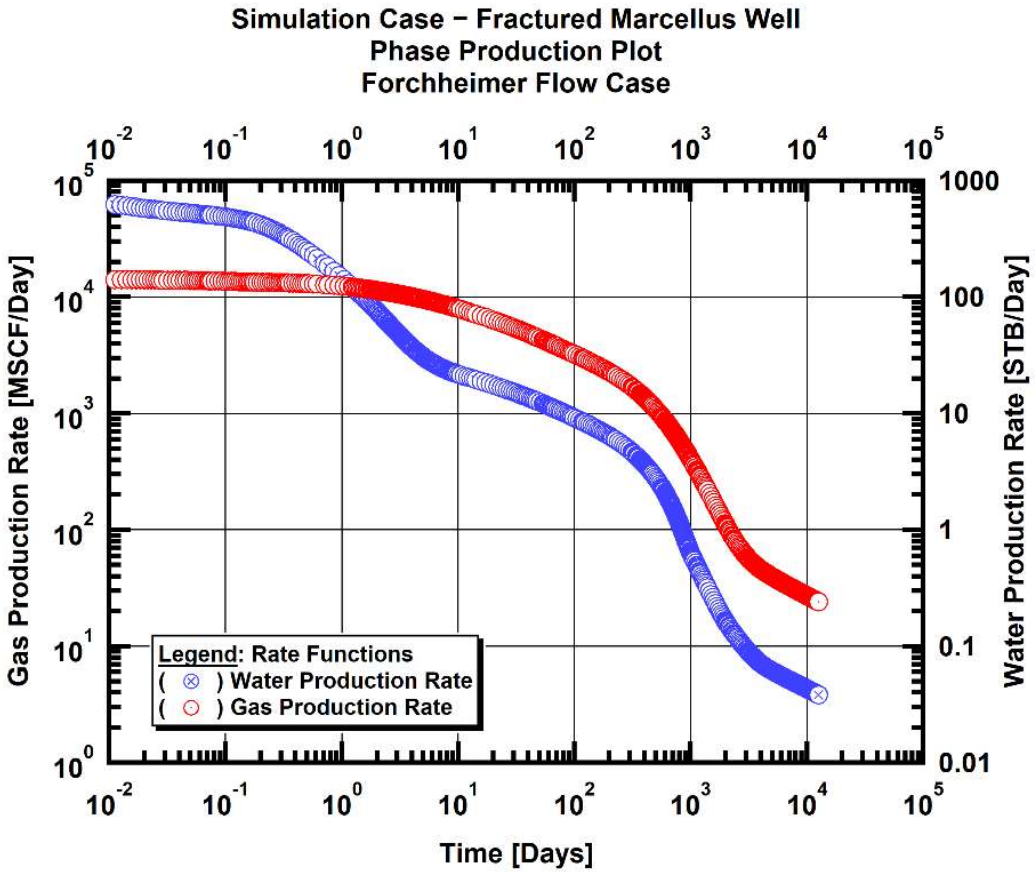

Figure 4.21— Log-log plot of the evolution over time of the phase production rates in the two-phase gas flow problem in the Marcellus shale (Forchheimer gas flow case).

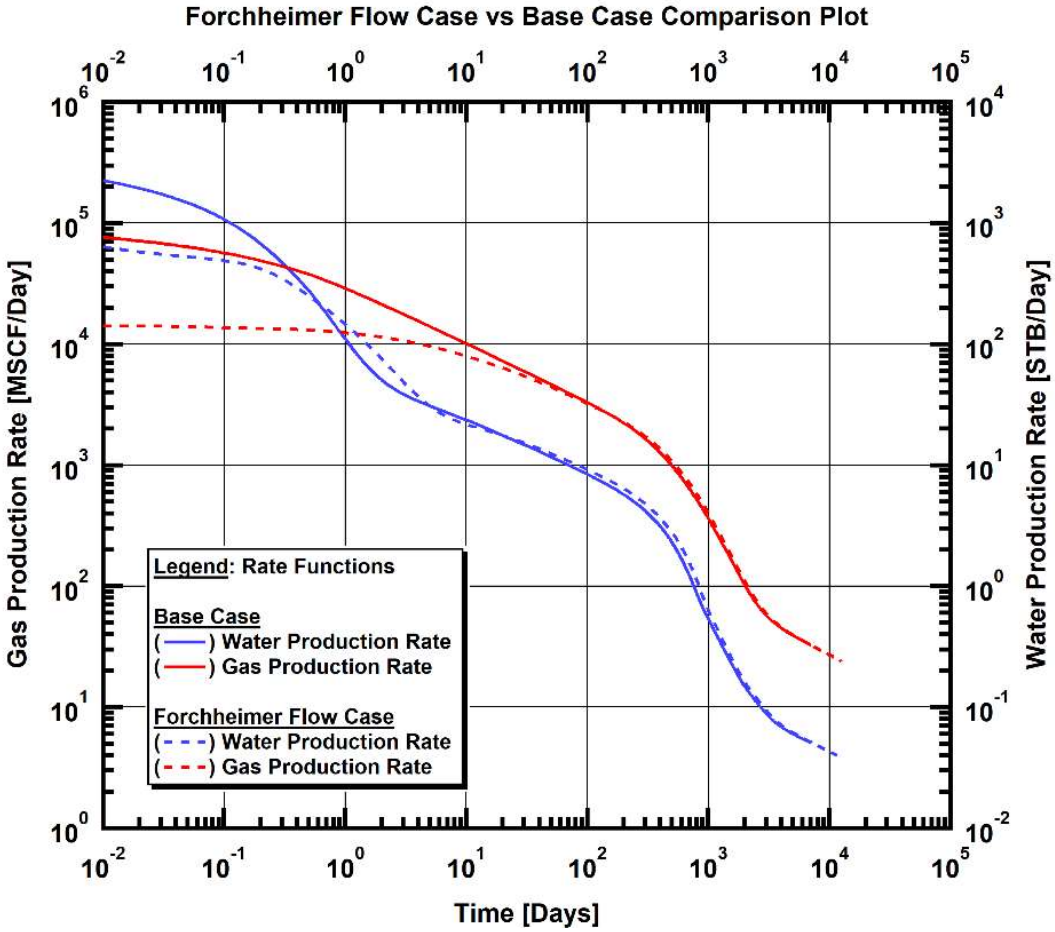

Figure 4.22— Log-log plot for the comparison of the evolution over time of the phase production rates of the base case and of the Forchheimer gas flow case in the two-phase gas flow problem in the Marcellus shale.

4.6 Effect of Adsorption

The effect of gas adsorption processes was modeled using the Langmuir isotherm (**Eq. 3.98**). Common sense indicates that the occurrence of gas adsorption would increase the ultimate recovery and postpone the terminal decline, since it adds to the gas mass in the system.

Fig. 4.23 shows the solution of the phase flow rates that were obtained from the mechanistic numerical model in the two-phase gas-water flow problem in the Marcellus shale with Langmuir adsorption. The Langmuir volume in this study was 300 scf/ton, and the Langmuir pressure 500 psi. A comparison of these results to those in the base case is shown in **Fig. 4.24**, which confirms the validity of the assumption that gas adsorption affects only the late-time behavior and postpones the emergence of the boundary-dominated flow regime. Additionally, the comparison tends to indicate that the effect of gas sorption is minor, and becomes relatively important when the phase flow rates have declined to low levels. To further investigate the gas sorption effect, I performed an analysis of the sensitivity of gas production rate to the Langmuir volume, the results of which are shown on **Fig.4.25**.

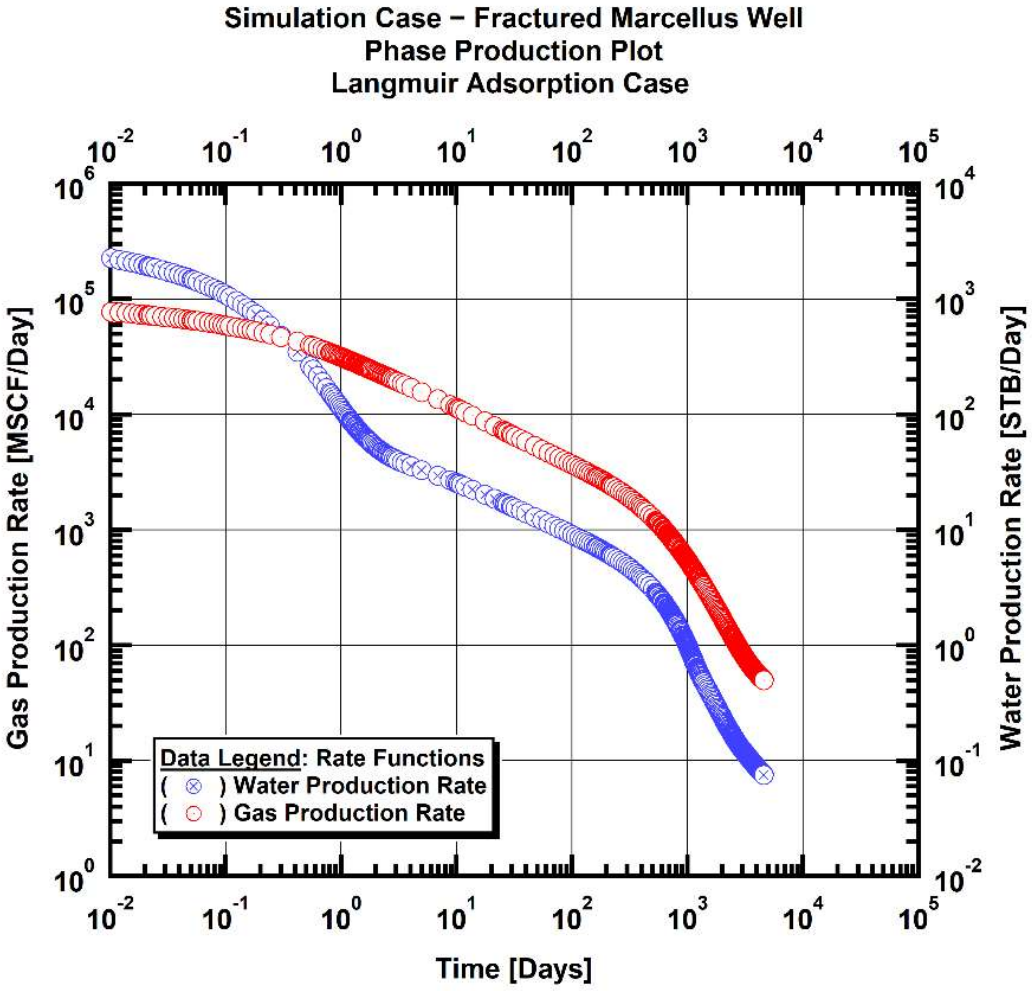

Figure 4.23— Log-log plot of the evolution over time of the phase production rates in the two-phase gas flow problem in the Marcellus shale (Langmuir adsorption case).

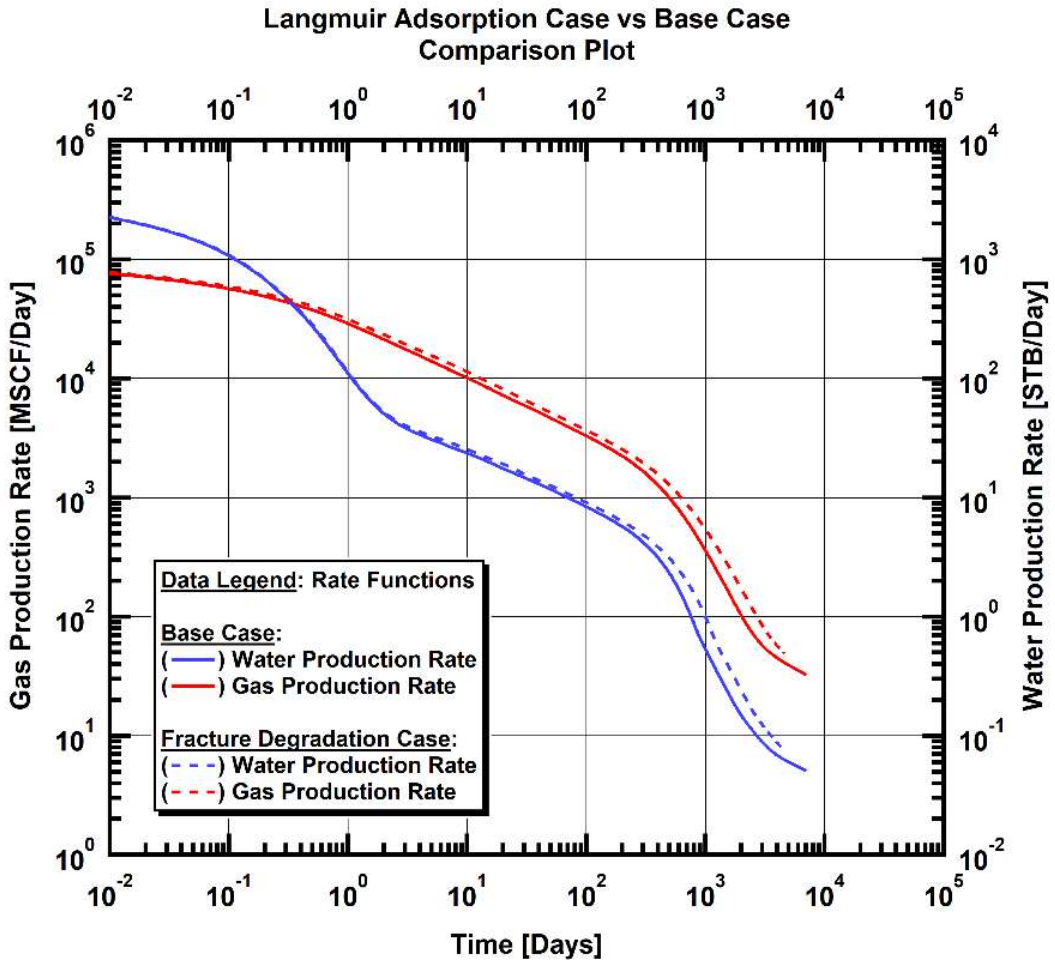

Figure 4.24— Log-log plot for the comparison of the evolution over time of the phase production rates of the base case and of the Langmuir adsorption case in the two-phase gas flow problem in the Marcellus shale.

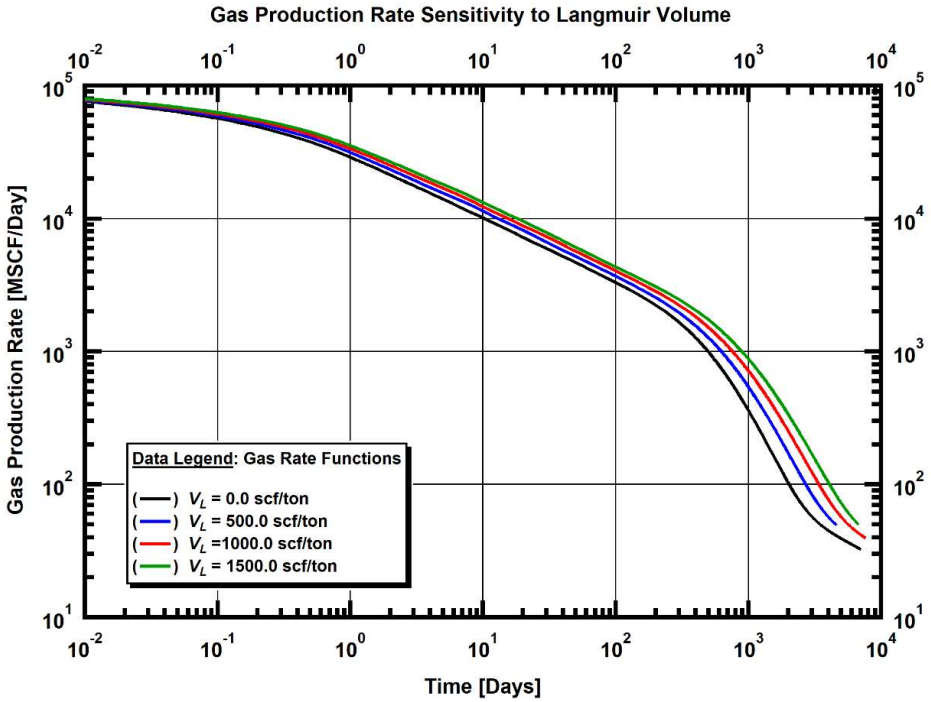

Figure 4.25—Log-log plot of the sensitivity of the production rate to the Langmuir volume in the two-phase dry gas flow problem in the Marcellus shale.

4.7 Effect of Spatial Discretization

To investigate the effect of spatial discretization on the accuracy of the numerical solution, I constructed a set of grids that discretized the same stencil in a number of elements that varied between 768 and 220,000. The latter is the grid in the base case of the Wolfcamp shale stencil and the Marcellus stencil.

A comparison plot of the effect of discretization on the evolution of the phase production rates in the three-phase black oil flow problem in the Wolfcamp shale is shown on **Fig. 4.26.** The solutions for the two coarsest grids, i.e., those comprising 768 and 1,980 elements, oscillate and, therefore, these grids are too coarse for an accurate description of the three-phase flow in the Wolfcamp shale. Another observation from the comparison plot in **Fig. 4.26** is the spread of the water production curves. For a higher resolution of

the water rate discrepancies, I plotted the first 300 days of water production in **Fig. 4.27** and observed deviations of up to 50% between the finest and the coarsest grids. The coarser grids appear to generate significantly higher water production rates, and slightly lower gas and oil production rates for the same problem. The effect is most likely caused by the specifics of the three-phase relative permeability and capillary pressure functions.

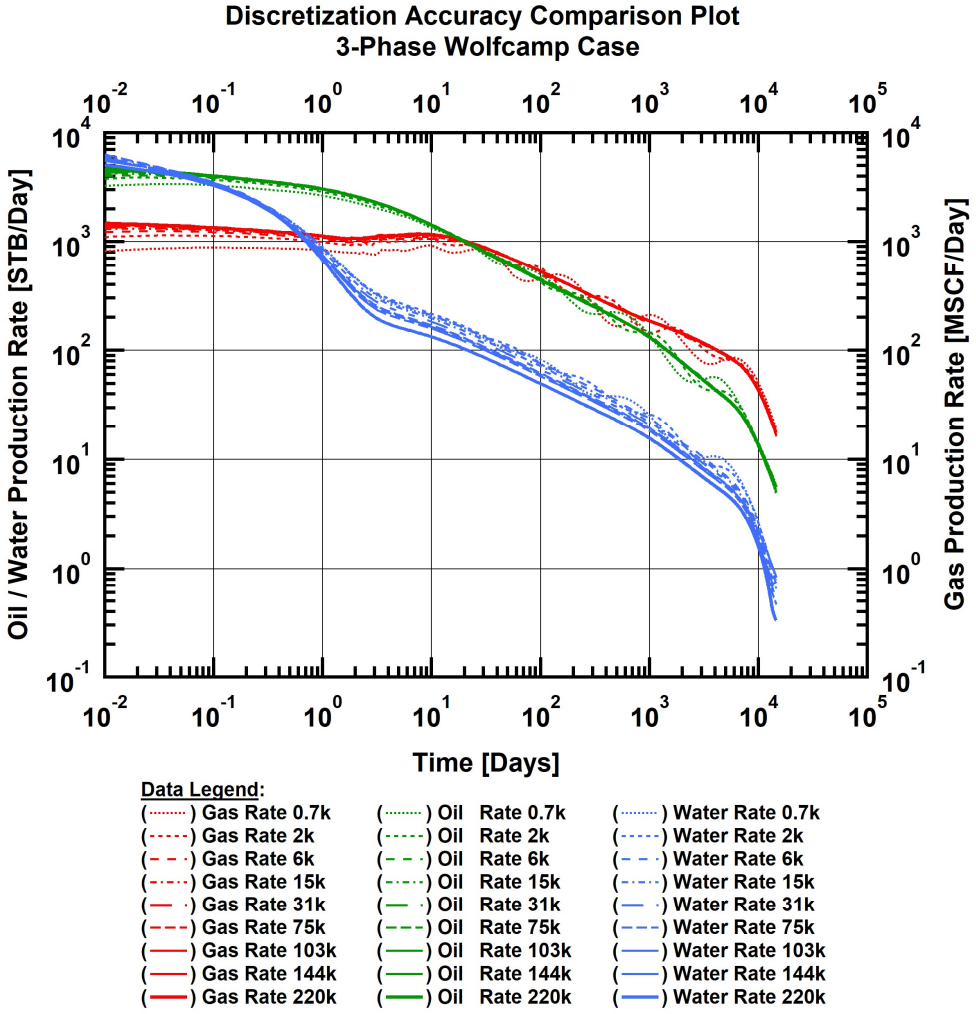

Figure 4.26— Log-log plot of the evolution over time of the phase production rates in the three-phase black oil flow problem in the Wolfcamp shale (variable domain discretizations).

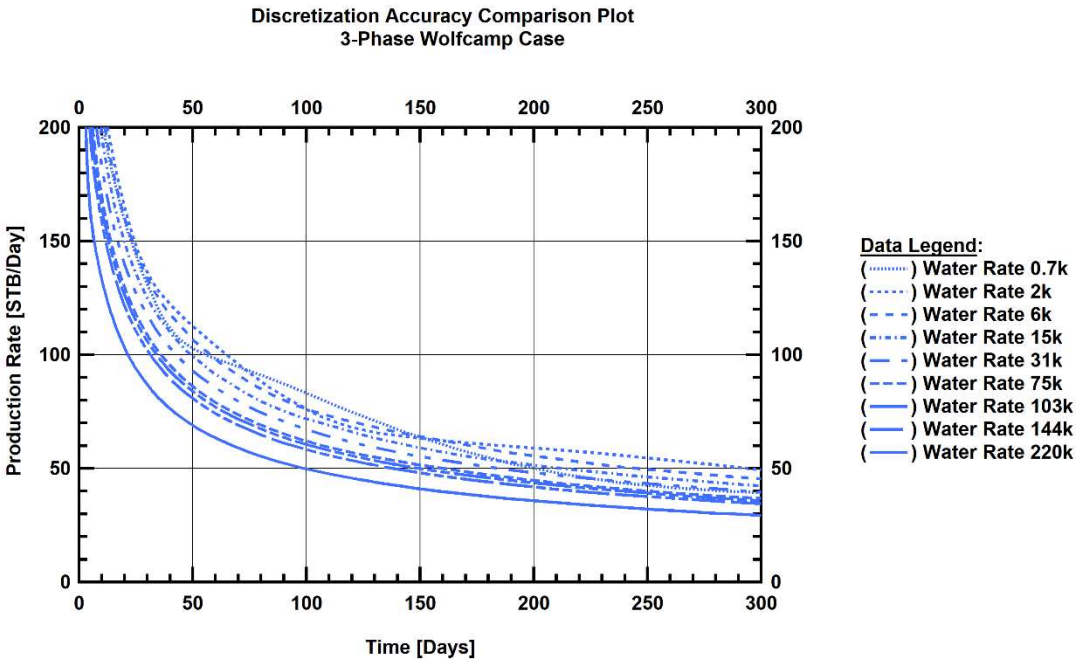

Figure 4.27— Effect of the level of domain discretization on the evolution of the water production rate in the three-phase black oil flow problem in the Wolfcamp shale.

To further investigate the accuracy of the numerical solution, I constructed error plots for the oil, gas and water rates. The finest grid solution is assumed to be accurate and was used as the reference solution. The error time series of the production rate of phase β for a grid of n blocks was calculated using the following formula:

$$\varepsilon_\beta^n(t) = \frac{\left| q_\beta^{220k}(t) - q_\beta^n(t) \right|}{q_\beta^{220k}(t)} \quad \text{.....(4.4)}$$

The error time series of the oil, gas and water rates for different domain discretizations (grid sizes) are shown on **Figs. 4.28**, **4.29** and **4.30** respectively. **Figs. 4.28** and **4.29** show that the errors for grids finer than comprising 2,000 elements do not exceed 10% when compared to the reference solution (for 200,000 elements). These solutions do not

obviously oscillate, as the ones for the 768 and 1,980 elements do in **Fig. 4.26**, however, oscillations are observed for all discretizations when plotted in the log-log error figures in **Figs. 4.28-4.29**. The minor oscillations that are observed in the oil and gas rates for very coarse discretizations need to be smoothed out in order to accurately calculate derivative-based functions like the *loss ratio* and the *loss ratio derivative* defined by **Eqs. 2.4** and **2.6**; otherwise, these oscillations can result in errors and discontinuities in the derivative functions. For such oscillations, we apply a spline-based smoothing algorithm implemented in Python.

Fig. 4.30 shows a different error trend. Solutions for grids finer than 1,980 blocks do not oscillate. However, the water production error for the second finest (144,480 elements) solution is around 20% for most of the production time, and can rise to 50-60% for coarser grids.

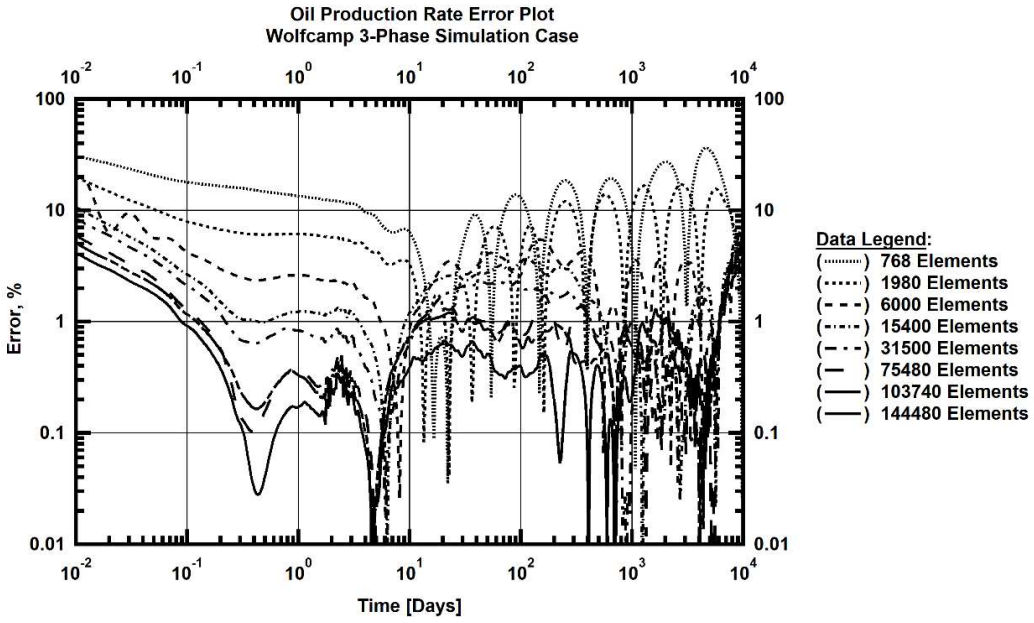

Figure 4.28— Effect of the level of domain discretization on the error in the oil production rate in the three-phase flow problem in the Wolfcamp shale.

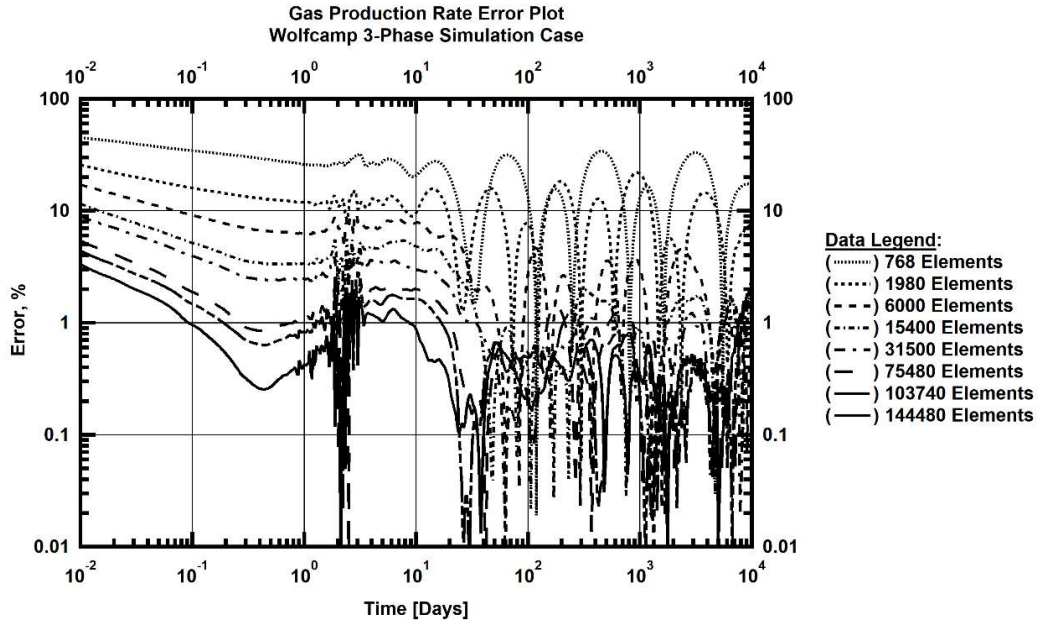

Figure 4.29— Effect of the level of domain discretization on the error in the gas production rate in the three-phase flow problem in the Wolfcamp shale.

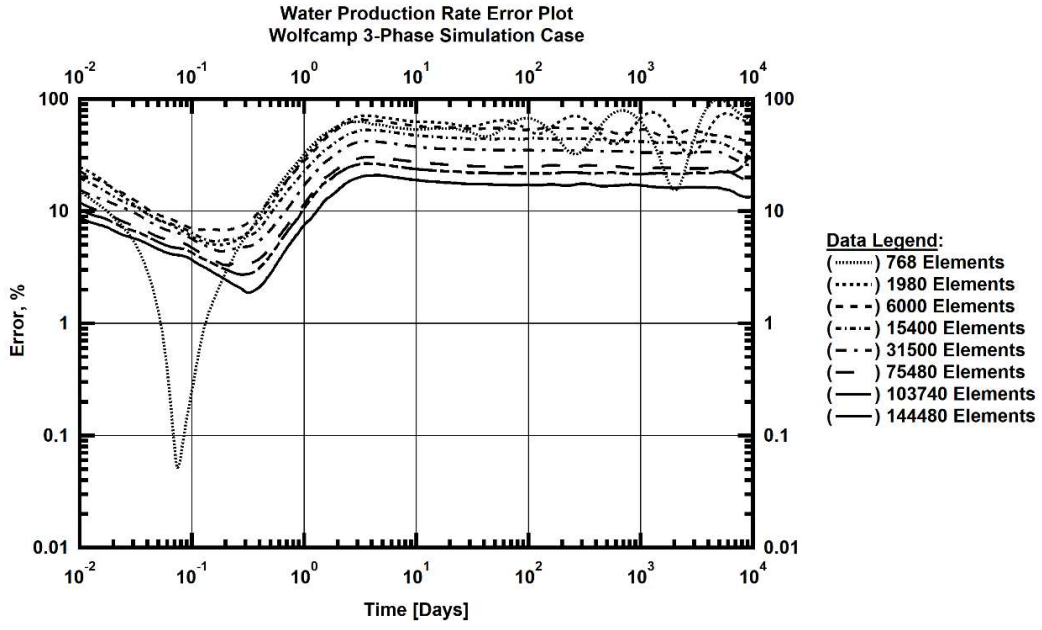

Figure 4.30— Effect of the level of domain discretization on the error in the water production rate in the three-phase flow problem in the Wolfcamp shale.

Fig. 4.31 shows the effect of domain discretization on the accuracy of the solutions of the phase production rates in the base case of the gas-water flow in the Marcellus shale. The water rates for the different discretizations show the most pronounced deviations from the reference case (involving 200,000 elements), but even the coarsest grids do not suffer from the oscillations observed in the three-phase black oil case. The lack of oscillations may be caused by the reduced complexity of the two-phase flow problem vs. that in the three-phase problem, including the relative permeability relationships. The linear scale of the vertical axis in **Fig. 4.32** reveals even higher spreads in the water production rates for varying discretizations than those in the three-phase case, which can even reach 100%.

Figs. 4.33-4.34 show the error time series (calculated using **Eq. 4.4**) corresponding to the gas and water production rate solutions, respectively, obtained for the various grid discretizations. **Fig. 4.33** exhibits oscillations in the gas rates that are not visible in **Fig. 4.31**, supporting the need for the application of smoothing techniques. The gas rate solutions for the two-phase gas-water problem appear to be the least affected by the spatial discretization, as the coarsest (768-element) solution error barely differs by 10%, from that obtained for the 220,000-element discretization.

The time series of the error in the water rate that is shown in **Fig. 4.34** demonstrates a trend similar to the one shown by **Fig. 4.30**, only greater in magnitude. The error is around 20% for the second finest grid of 144,480 blocks, but exceeds 100% for grids coarser than 6,000 blocks and reaches a high of 500% at t = 1000 days.

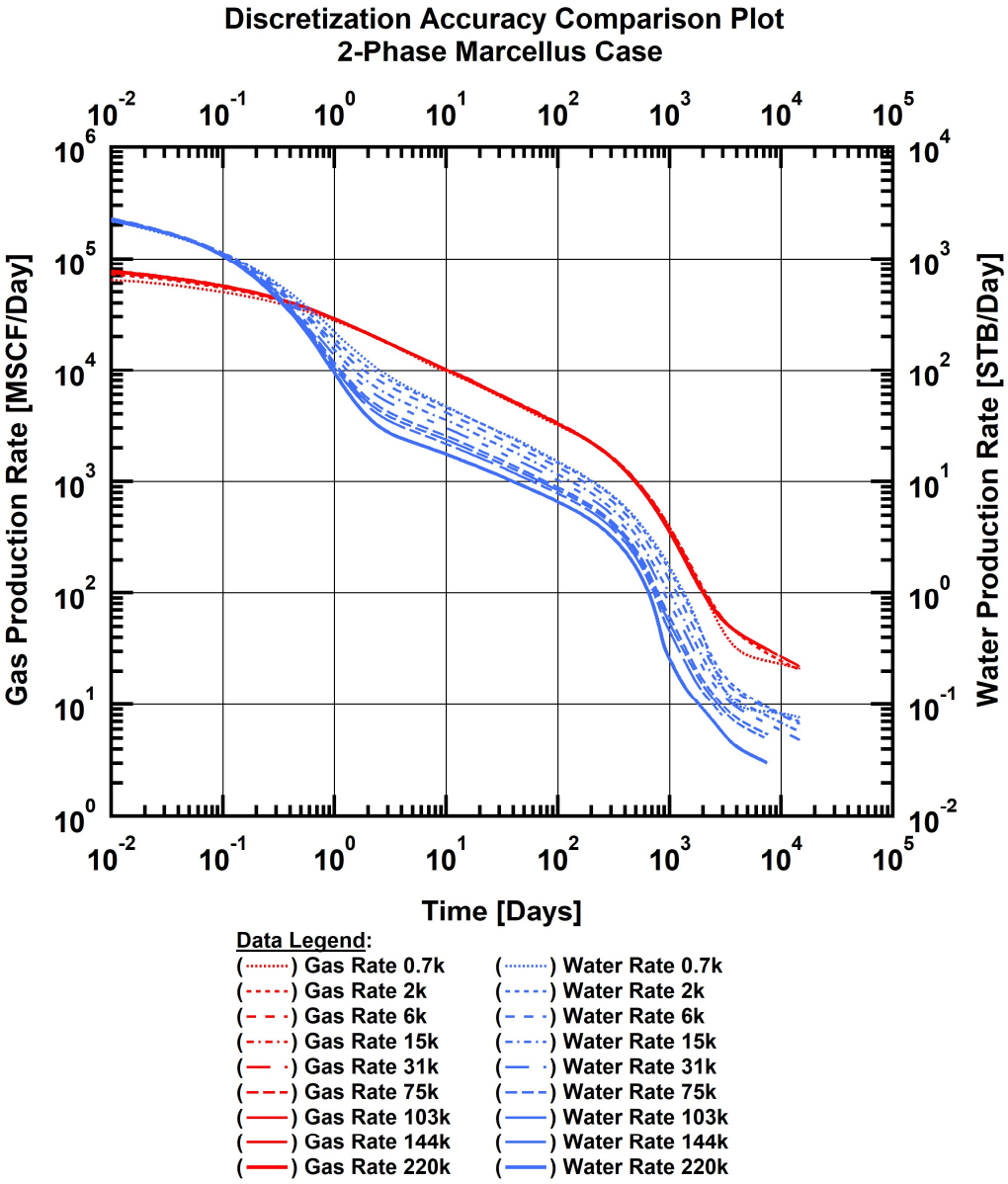

Figure 4.31— Log-log plot of the evolution over time of the phase production rates in the two-phase gas-water flow problem in the Marcellus shale (variable domain discretizations).

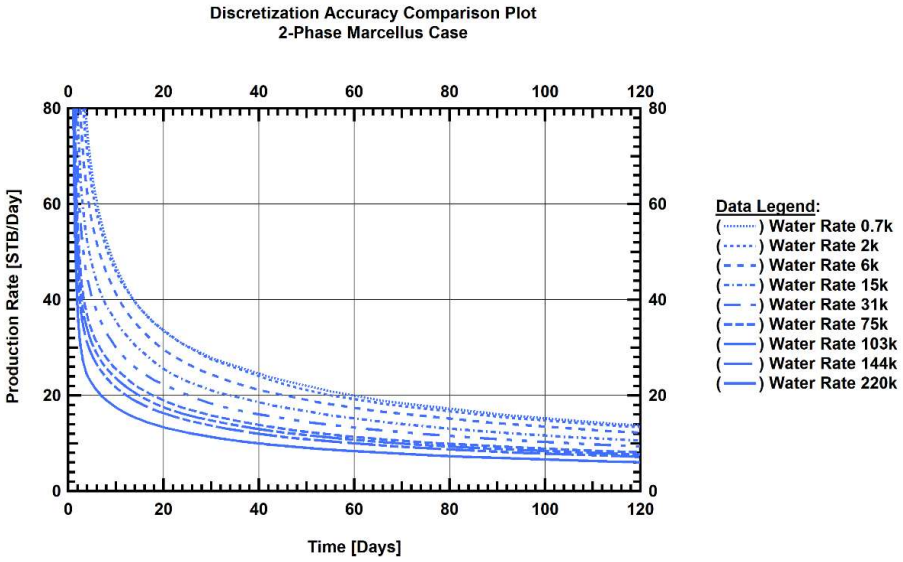

Figure 4.32— Effect of the level of domain discretization on the evolution of the water production rate in the two-phase, gas-water flow problem in the Marcellus shale (variable domain discretizations).

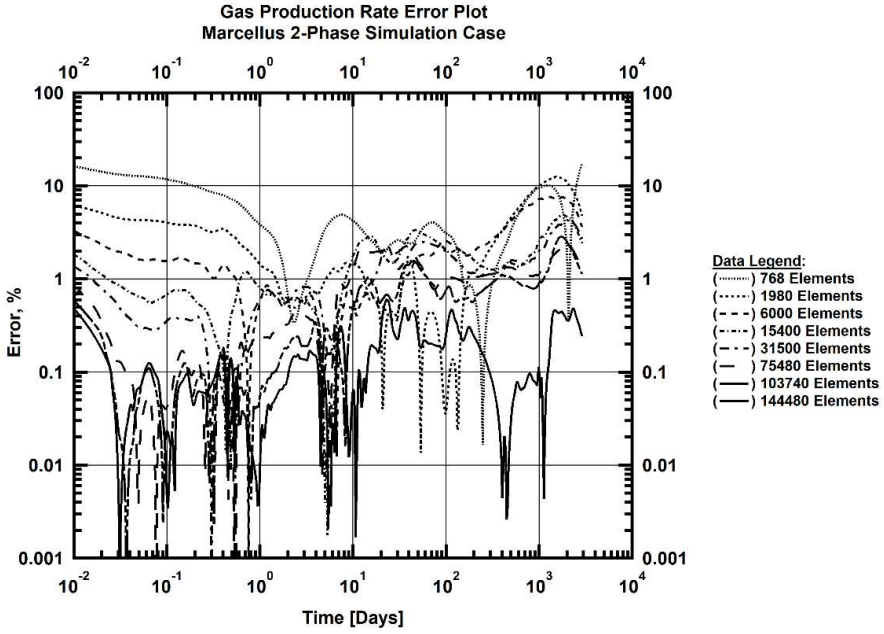

Figure 4.33— Effect of the level of domain discretization on the error in the gas production rate in the two-phase gas-water flow problem in the Marcellus shale (variable domain discretizations).

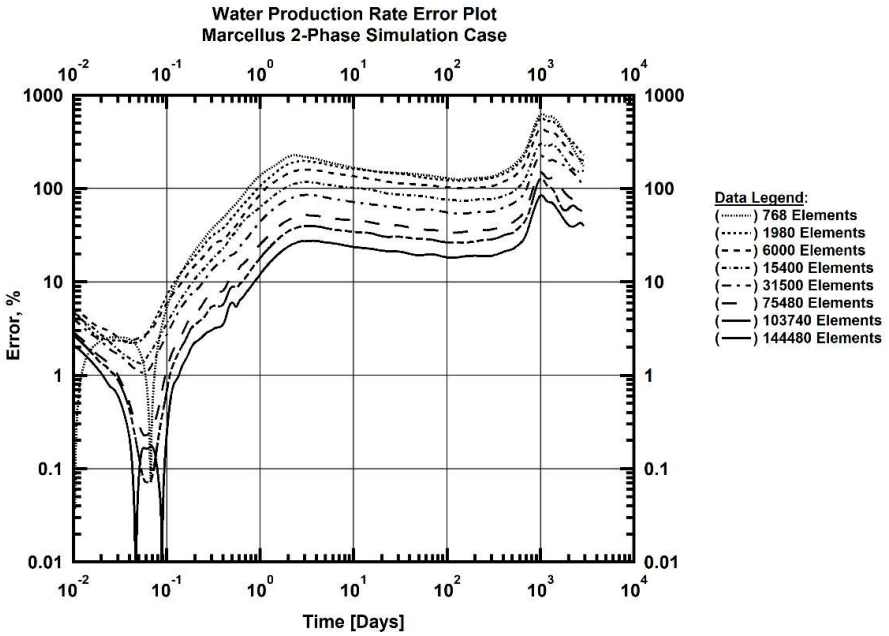

Figure 4.34— Effect of the level of domain discretization on the error in the water production rate in the two-phase gas-water flow problem in the Marcellus shale (variable domain discretizations).

I summarized the investigation of the effect of spatial discretization on the accuracy of the numerical solution by calculating the average of each error time series and plotting it versus the number of elements. The average error in a given phase rate solution for a given grid size is calculated in the following manner:

$$\bar{\varepsilon}_{\beta}^{n} = \frac{1}{m}\sum_{i=1}^{m}\frac{\left|q_{\beta}^{220k}\left(t_i\right) - q_{\beta}^{n}\left(t_i\right)\right|}{q_{\beta}^{220k}\left(t_i\right)} \quad \text{.....(4.5)}$$

Fig. 4.35 presents the log-log plot of the average error versus the number of grid-blocks for the three-phase black-oil flow problem in the Wolfcamp shale, and **Fig. 4.36** shows the analogous plot for the two-phase gas-water flow problem in the Marcellus shale. These plots can be used to estimate the error (defined as the deviation from the solution

obtained for the finest discretization of 200,000 elements) of the numerical solution for a given grid size.

Another important conclusion derived from **Figs. 4.35-4.36** is that the current relative permeability and capillary pressure models deliver solutions for the wetting phase flow that are highly dependent on grid discretization as the water error trends are much higher than those for the gas and oil. Some of this dependence on discretization may be attributed to the relative permeability and capillary pressure functions. Note that in this work water is considered the wetting phase and the error in the water may not be very important as the focus is on the gas and oil rates; however, this can be a major issue for oil-wet systems.

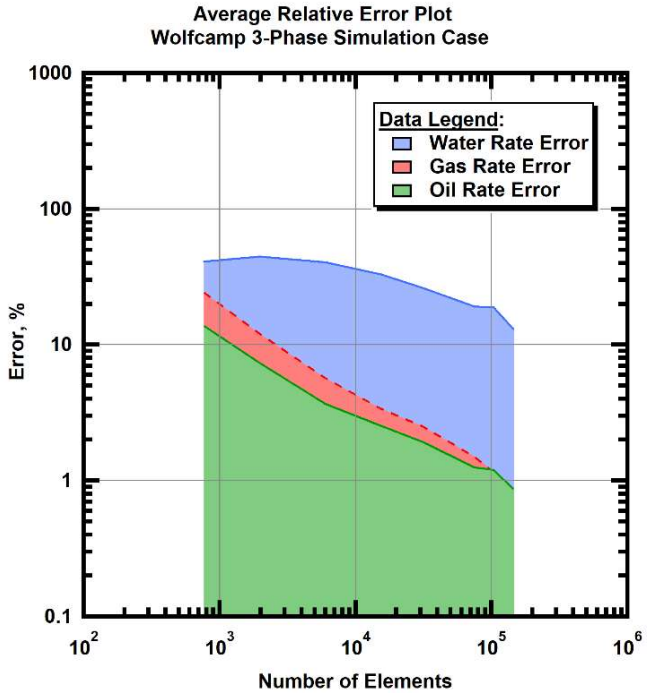

Figure 4.35— Log-log plot of the average relative error in the phase rates vs. the number of elements in the three-phase black-oil flow problem in the Wolfcamp shale.

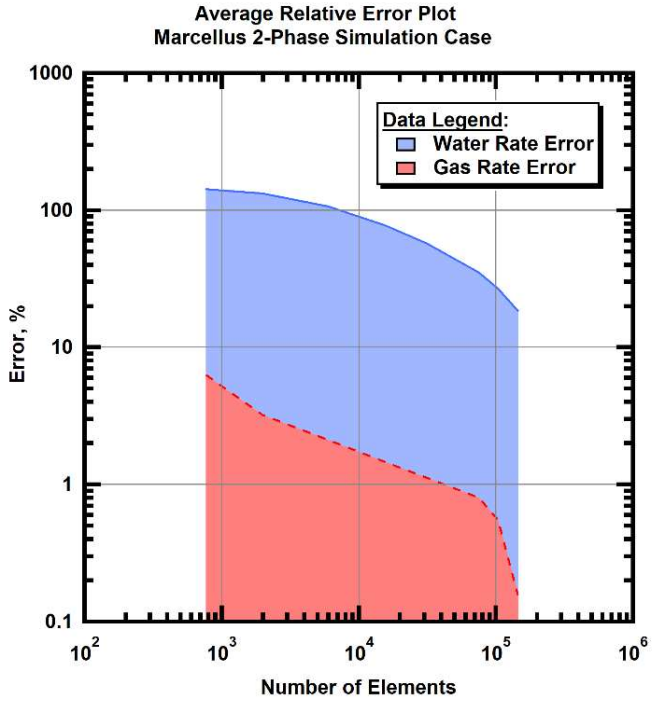

Figure 4.36— Log-log plot of the average relative error in the phase rates vs. the number of elements in the two-phase gas-water flow problem in the Marcellus shale.

CHAPTER V

PROPOSED TIME RATE MODEL

5.1 Model Description

Based on results generated in this work, a new time-rate relationship is proposed:

$$q(t) = q_i K_1(a_2 + a_3 t)\ \exp\left(a_2 + t\right), \quad (5.1)$$

where $K_1(x)$ is the modified Bessel function of the second kind, the parameter q_i is a scaling unit factor, and the parameters a_2 and a_3 control early time behavior and terminal decline, respectively. Introduction into **Eq. 5.1** the initial and the terminal decline rates that correspond to the various a_i (i = 2,3) parameters yields:

$$q(t) = q_i K_1[D_i + (1 + D_{\text{inf}})t]\ \exp\left(D_i + t\right). \quad (5.2)$$

To further investigate behavior of this model, it is necessary to derive an expression for the so-called reciprocal of the *loss-ratio* function (**Eq. 2.4**) and for the *derivative of the loss ratio* function (**Eq. 2.6**):

$$D(t) = -\frac{1}{q(t)}\frac{dq(t)}{dt} \quad (2.4)$$

Substitution of **Eq. 5.1** into **Eq. 2.4** yields:

$$D(t) = \frac{a_3}{a_2 + a_3 t} + \frac{a_3 K_0(a_2 + a_3 t)}{K_1(a_2 + a_3 t)} - 1. \quad (5.3)$$

Recall the definition of the *derivative of loss ratio* as

$$b(t) = \frac{d}{dt}\left[\frac{1}{D(t)}\right] \quad (2.6)$$

Substitution of **Eq. 5.3** into **Eq. 2.6** results in

$$b(t) = a_3^{\,2} \frac{\left[-3K_0(a_2 + a_3 t)^2 + \frac{4\,[(a_2 + a_3 t)^2 + 2]K_1(a_2 + a_3 t)^2}{(a_2 + a_3 t)^2} - K_2(a_2 + a_3 t)^2 \right]}{\left[a_3[K_0(a_2 + a_3 t) + K_2(a_2 + a_3 t)] - 2K_1(a_2 + a_3 t) \right]^2} \quad \text{..... (5.4)}$$

The full derivation of **Eqs. 5.3** and **5.4** can be found in **Appendix B**.

Eqs. 5.1, 5.3, 5.4 are used to construct type curves in the "*qDb*" diagnostic plot format to show how the proposed K_1-Exponential (K1X) DCA model behaves with respect to the model parameters. **Fig. 5.1** demonstrates the K1X model type curves with respect to variable a_2 or the D_i *initial decline parameter*. **Fig. 5.2** presents the K1X model type curves with respect to variable a_3 or the D_{inf} *terminal decline parameter*.

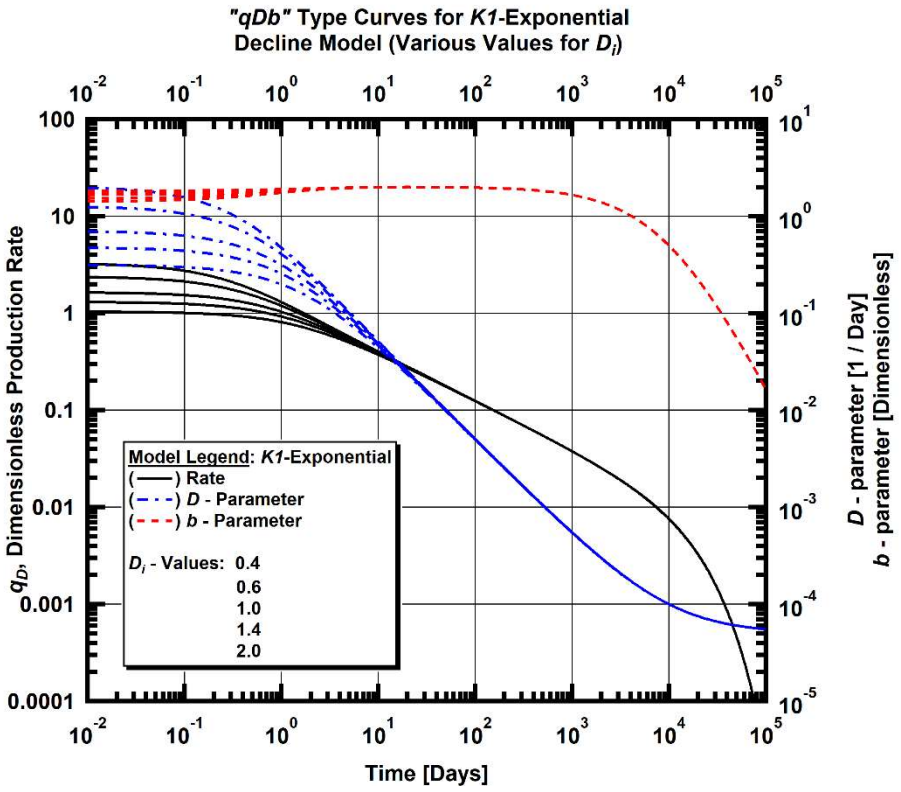

Figure 5.1— Log-log "*qDb*" plot of the proposed K1X model type curves with respect to various values of the initial decline parameter.

Fig. 5.2 shows that the proposed model degenerates into a hyperbolic decline curve when D_{inf} is equal to zero (or $a_3 = 1$).

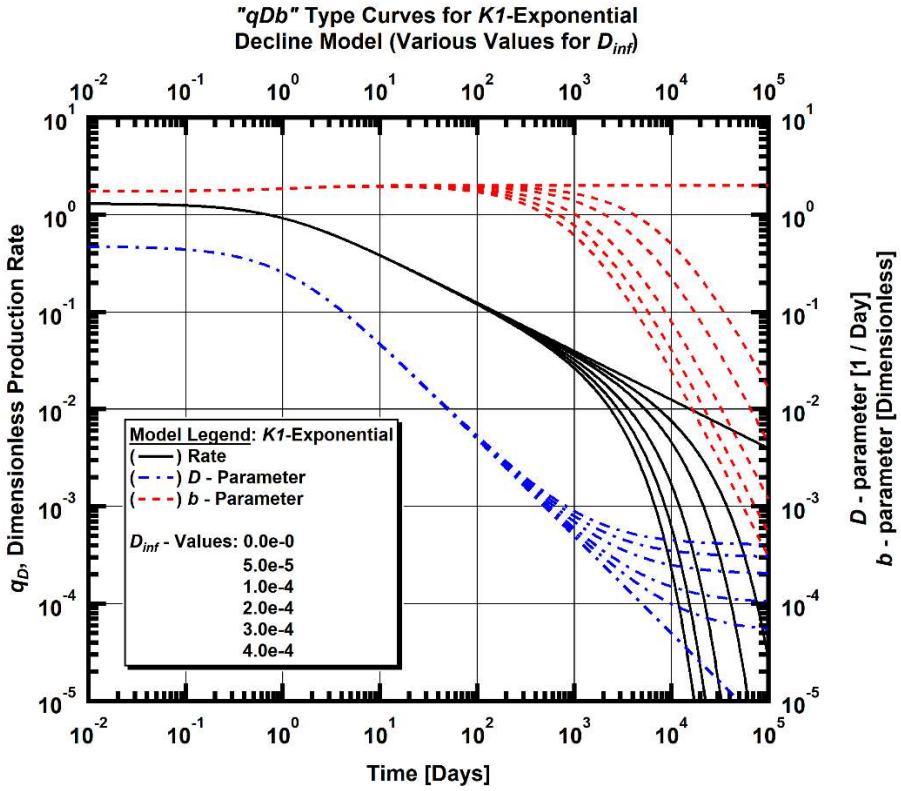

Figure 5.2— Log-log "*qDb*" plot of the proposed K1X model type curves with respect to various values of the terminal decline parameter.

5.2 Theoretical Basis

In order to validate the proposed time-rate K1X model, I compare it first to the Olarewaju and Lee (1989) analytical solution. The comparison plot against the analytical solution and the simulation data for the three-phase black-oil flow in the Wolfcamp shale is presented in **Fig. 5.3**. The comparison plot against the analytical solution and the simulation data for the two-phase gas-water flow in the Marcellus shale is presented in **Fig. 5.4**.

In **Fig. 5.3** I observe that the K1X model almost perfectly follows the 3D numerical solution, while the analytical solution conforms to the 2D numerical solution. The main deviation of the K1X model from the trilinear solution occurs during the early times. Another difference from the analytical solution is the smoother K1X transition between the *linear flow* regime and the *boundary-dominated flow*. I also note that the K1X does not model the *compound linear flow*. However, this is not a needed feature for the purpose of decline-curve analysis because the compound linear flow usually occurs beyond the economic limit. All of the above observations and comments apply also to the observations in **Fig. 5.4**.

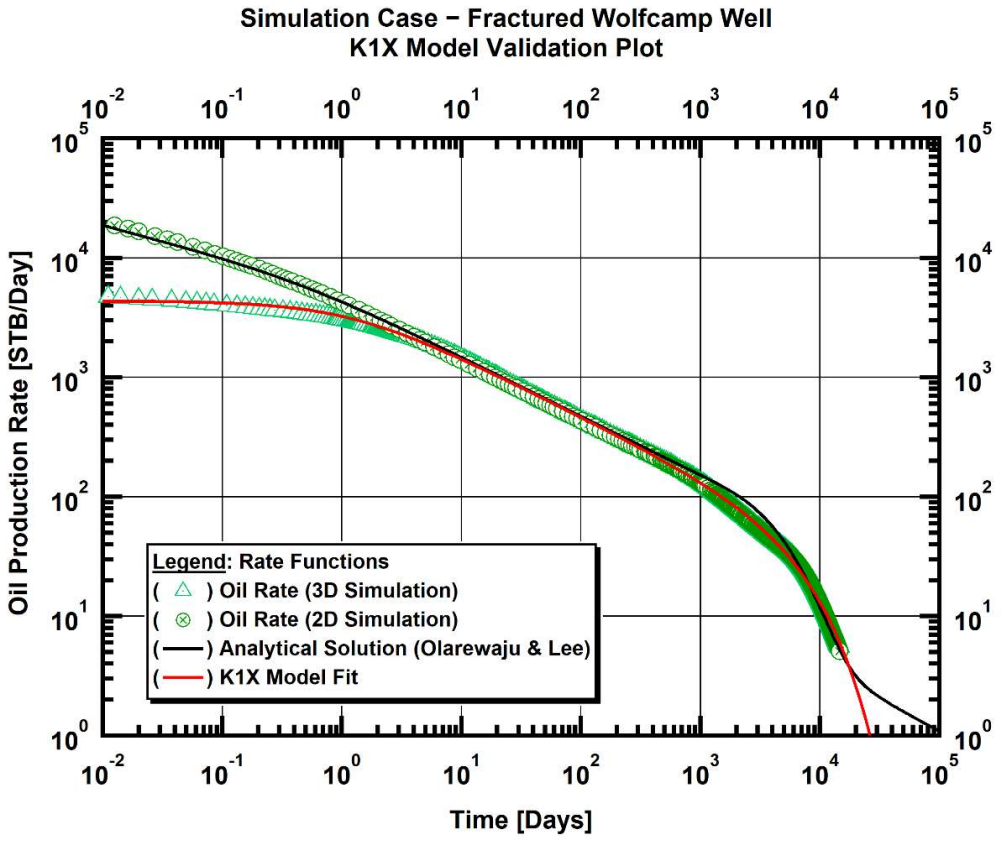

Figure 5.3 —Log-log K1X model validation plot for the three-phase black oil flow problem in the Wolfcamp shale.

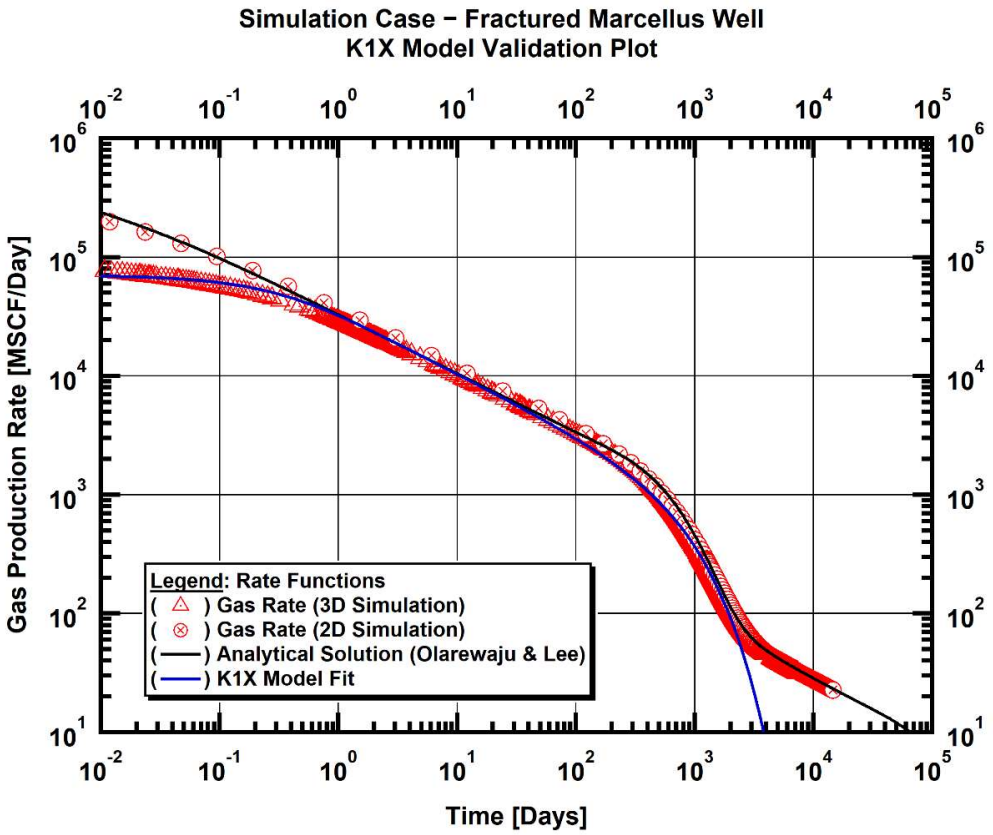

Figure 5.4 —Log-log K1X model validation plot for the two-phase gas-water flow problem in the Marcellus shale.

Because the K1X model appears capable of reproducing both the analytical and the numerical solutions up to the onset of the secondary linear flow, I attempt to relate the model parameters to the reservoir and fluid properties.

In this section I investigate possible correlations between the K1X model parameters and the reservoir and fluid properties by matching the model to the analytical solution.

Because the early-time behavior of the analytical solution does not conform with our numerical prediction or the K1X model, I focus on the late-time behavior. Inspection of

the Olarewaju and Lee (1989) solution (**Eqs. 2.48-2.54**) indicates that there are only two things affecting the terminal decline:

- Aspect ratio, y_{eD};
- Dimensionless time group, $\frac{k}{\phi\mu c_t x_f^{\,2}}$.

All other parameters only affect the early-time behavior or the magnitude of the rate function. To establish a relation between the K1X terminal decline parameter $D_{\inf}$ and the terminal decline parameters of the analytical solution, I begin by generating a set of five analytical curves with variable y_{eD} values. Then, I fit the K1X model to the analytical curves using a non-linear least-squares curve-fitting algorithm developed in Python. Finally, I plot the $D_{\inf}$ vs. y_{eD} values in a cartesian plot (**Fig. 5.5**).

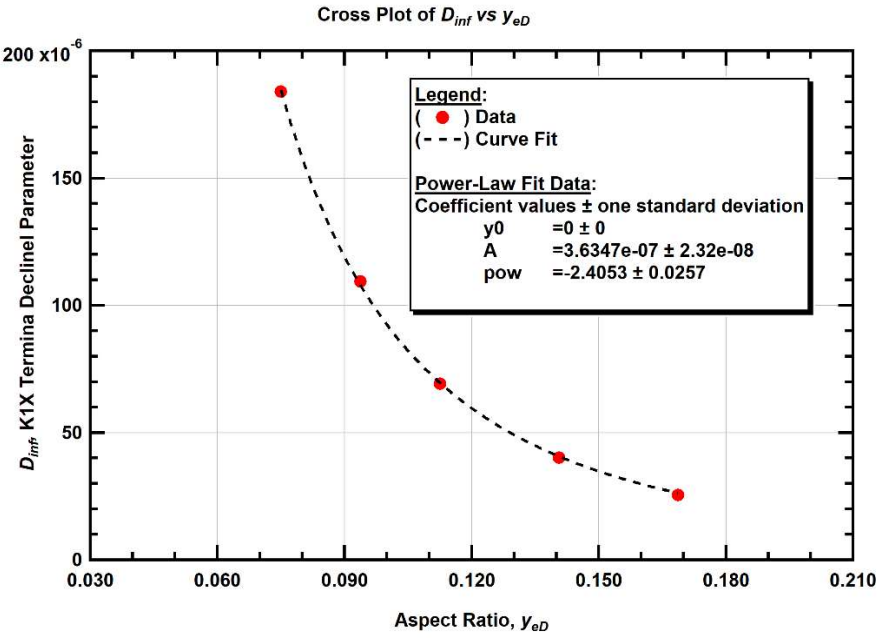

Figure 5.5 —Cross-plot of the $D_{\inf}$-parameter vs. the aspect ratio y_{eD} from the fit of the K1X model to the Olarewaju and Lee (1989) analytical solution.

Fig. 5.5 suggests a power-law relationship between D_{inf} and y_{eD}, which is confirmed by the non-linear regression. Mathematically, D_{inf} is expressed as a function of y_{eD} in the following way:

$$D_{\text{inf}} = c_1 y_{eD}^{\,c_2} . \quad (5.5)$$

Knowing that D_{inf} must be a function of dimensionless time group (τ_D) leads to the assumption that **Eq. 5.5** can be rewritten as:

$$D_{\text{inf}} = c_3 \tau_D y_{eD}^{\,c_2} , \quad (5.6)$$

where

$$\tau_D = \frac{k}{\phi \mu c_t x_f^{\,2}} . \quad (5.7)$$

The c_3 and c_2 coefficients are determined in the following manner: I construct several sets of analytical curves, with every set consisting of various y_{eD} rate solutions for a fixed τ_D; all the individual values of y_{eD} are unique, and the τ_D values are unique for each set. Then, a τ_D-normalized terminal decline parameter is defined as:

$$D_{\text{inf}-\text{D}} = \frac{D_{\text{inf}}}{\tau_D} . \quad (5.8)$$

Finally, the K1X model is fit to the analytical curves, and $D_{\text{inf}-\text{D}}$ is plotted vs. y_{eD} on a log-log scale, exploiting the known fact that the relationship is a power-law. The result is shown in **Fig. 5.6**.

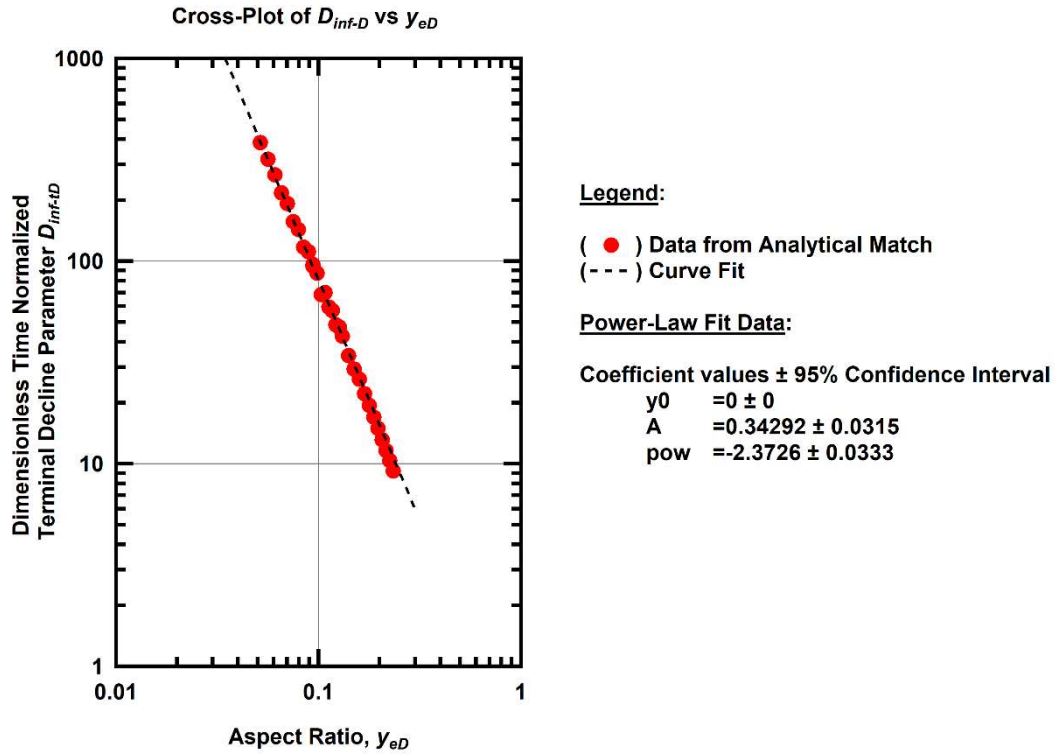

Figure 5.6 —Log-log Cross-plot of the $D_{\inf -D}$-parameter vs. the aspect ratio y_{eD}, obrained from the fit of the K1X model to the Olarewaju and Lee (1989) analytical solution.

The non-linear regression of the data presented on **Fig. 5.6** yields the relationship:

$$D_{\inf} = 0.34292 \frac{k}{\phi \mu c_t x_f^{\ 2}} y_{eD}^{\ -2.3726} \quad \text{.....(5.9)}$$

Thus, I have established a direct connection of the $D_{\inf}$ terminal decline parameter of the K1X model to the reservoir and fluid properties, as well as the system geometry, through the Olarewaju and Lee (1989) analytical solution. Moreover, the relationship appears so strong, that it suggests that the proposed time-rate model may be a form of an analytical solution itself.

5.3 Validation Against the Mechanistic Model

I now use **Eqs. 5.1, 5.3, 5.4** to construct a "*qDb*" diagnostic plot to observe how well the results from the proposed modified K1X DCA model conform to the results of the mechanistic model. To calculate the $D(t)$ and $b(t)$ functions corresponding to the results from the mechanistic model, I used cubic splines to smooth the data and to compute the derivatives. I conducted the regression of the proposed model parameters to the results of the mechanistic model using a non-linear least squares regression algorithm implemented in Python.

As can be seen from **Fig. 5.7**, the proposed K1X DCA model is successfully fitted to all of the flow regimes present in the mechanistic model response:

- The early-time fracture-dominated performance (*i.e.,* fracture (water) unloading).
- The "linear flow" regime (*i.e.,* non-interferring fractures).
- The transitional flow behavior, from linear flow to boundary-dominated flow.
- The late-time boundary-dominated flow.

It can be seen from **Fig. 5.7** that the proposed model easily describes both the hyperbolic and the exponential behavior (e.g., the Modified Hyperbolic DCA relation) in a single equation. To prove that the late time behavior of the K1X model is exponential, I plotted these data on a semilog scale and observed the expected straight line (**Fig. 5.8**).

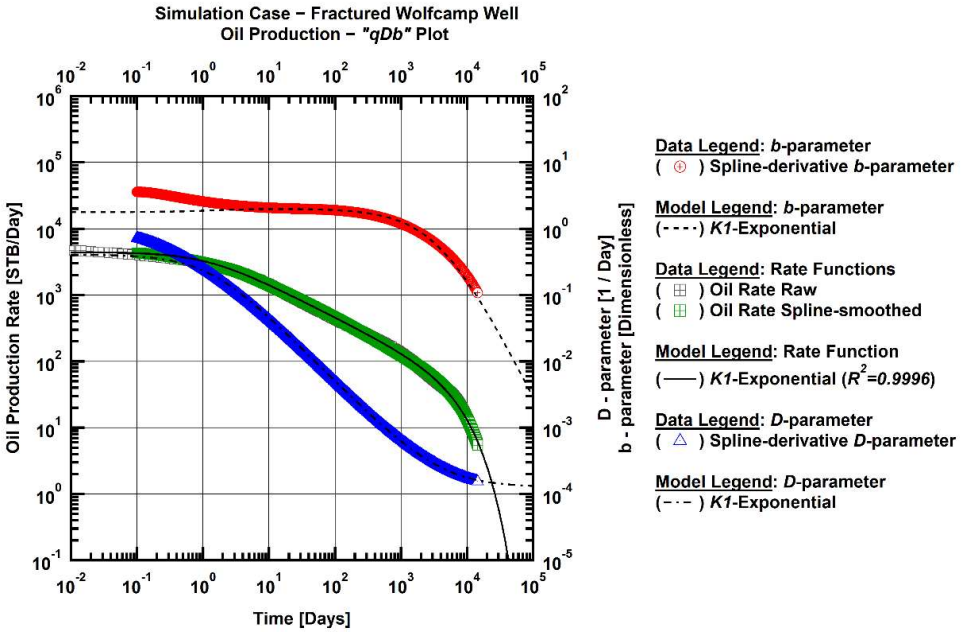

Figure 5.7 —Log-log "*qDb*" plot and K1X model fit for the three-phase black oil flow problem in the Wolfcamp shale, base case.

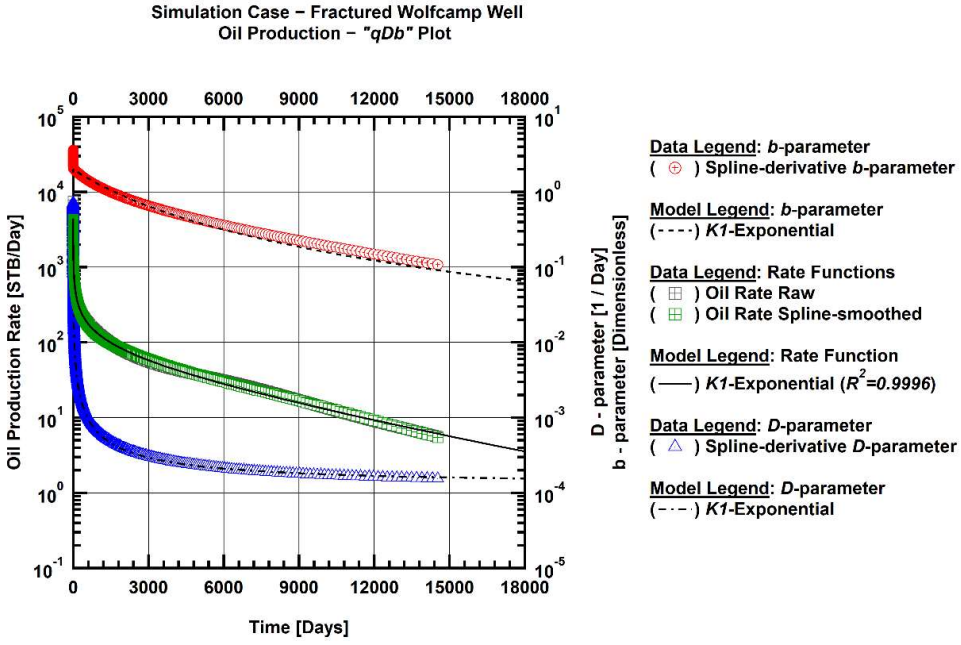

Figure 5.8 —Semi-log "*qDb*" plot and K1X model fit for the three-phase black oil flow problem in the Wolfcamp shale, base case.

The proposed K_1-Exponential model seems to match the base case mechanistic response very well, and it also matches the behavior of the derivative functions that describe the *D*- and *b*-parameters.

I continue the study of the proposed time-rate relation's applicability by matching other cases generated in this work. **Figs. 5.9-5.13** show the K1X model fit to the mechanistic model solutions to the problem of the various cases of the three-phase black-oil Wolfcamp problem presented on **Figs. 4.4-4.6,** and to the solutions of the cases of the two-phase gas-water Marcellus problem presented on **Figs. 4.10-4.11, 4.21** and **4.23**. The model provides a very good fit, with an average coefficient of determination $R^2 = 0.9988$ for the Wolfcamp cases and $R^2 = 0.9960$ for the Marcellus cases. Again, I notice that the derivative functions of the *D*- and *b*-parameters are accurately modeled by the K_1-Exponential decline curve relationship both for the three-phase black oil and the two-phase gas problems.

The K1X model, however, suffers of the same problem afflicting the Modified-Hyperbolic model, which does not need the terminal decline parameter to match the early data. Thus, it cannot be inferred from the curve fitting procedure before the start of the boundary-dominated flow regime. To mitigate this major issue, I tested the correlation for the K1X terminal decline parameter (**Eq. 5.9**) inferred from an exhaustive validation against the analytical solutions in the mechanistic model cases. I applied the same procedure I used to develop the data presented in **Fig 5.6** on the sensitivity to production to the aspect ratio cases, as shown in **Figs. 4.7, 4.12** and **4.25**. The resulting cross-plot is presented on **Fig. 5.16**.

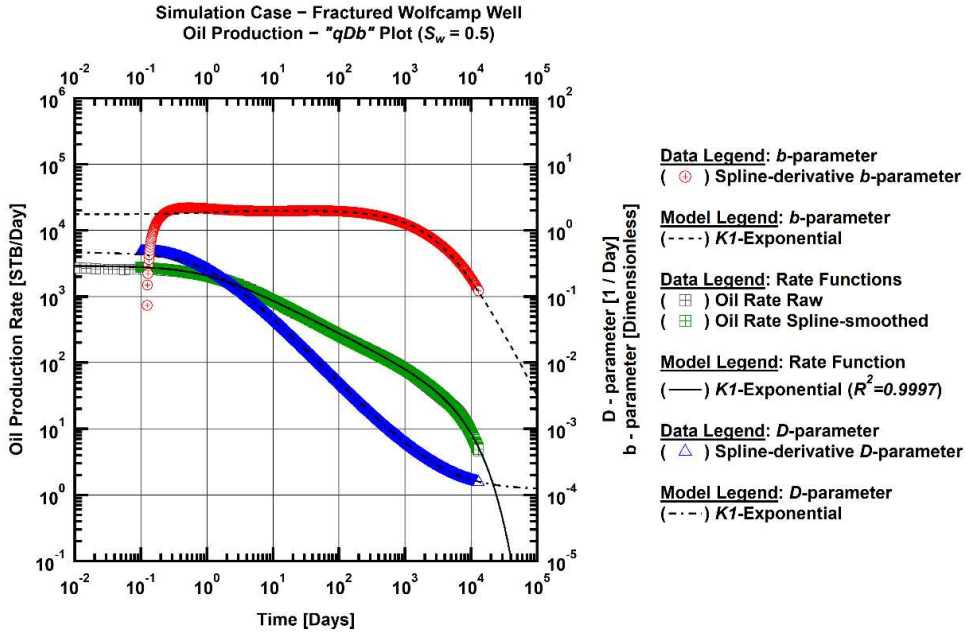

Figure 5.9 —Log-log "*qDb*" plot and K1X model fit for the three-phase black oil flow problem in the Wolfcamp shale, $S_w = 0.5$ case.

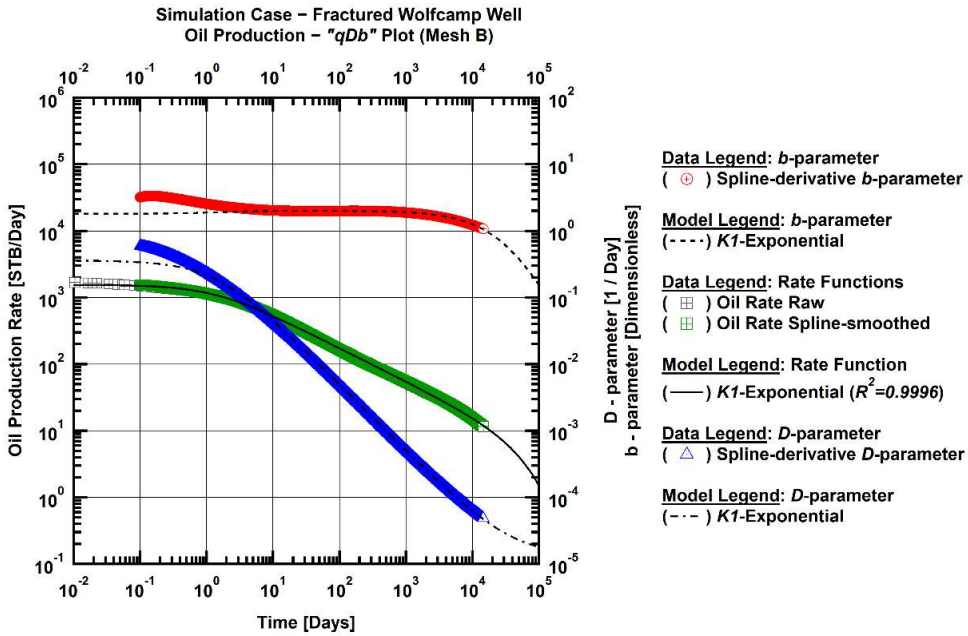

Figure 5.10—Log-log "*qDb*" plot and K1X model fit for the three-phase black oil flow problem in the Wolfcamp shale, Mesh B case.

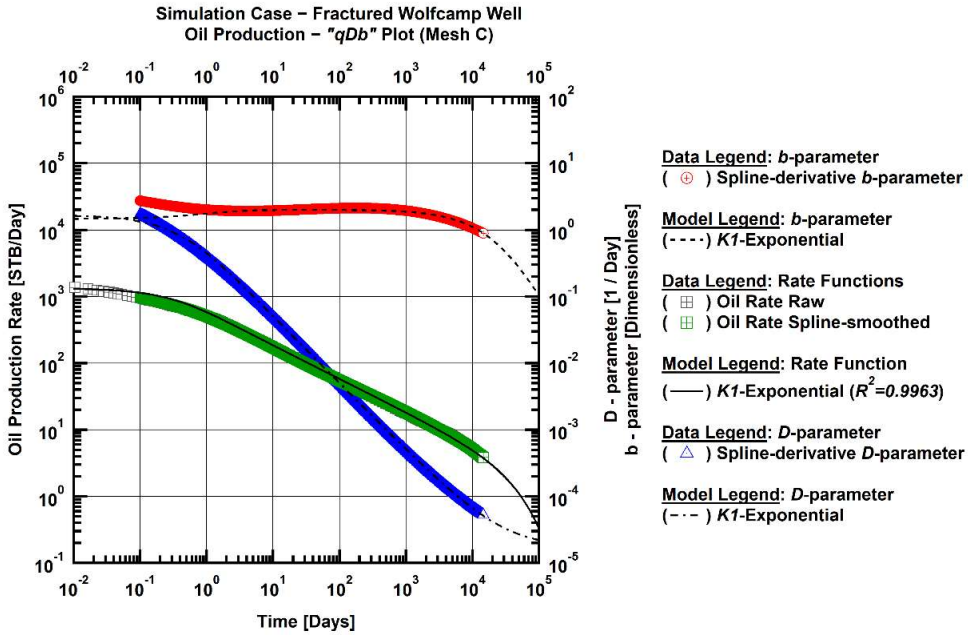

Figure 5.11—Log-log "*qDb*" plot and K1X model fit for the three-phase black oil flow problem in the Wolfcamp shale, Mesh C case.

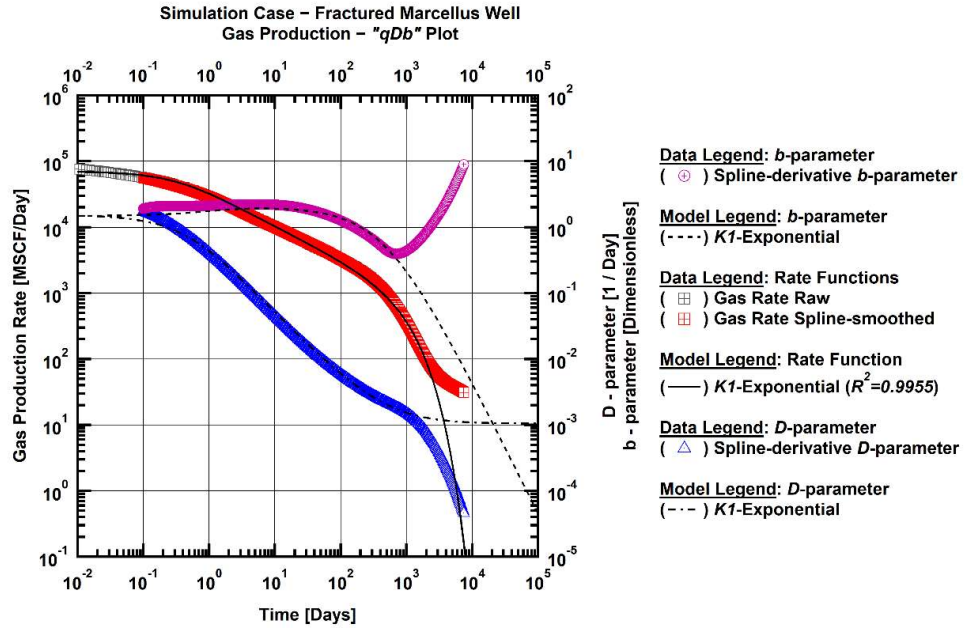

Figure 5.12—Log-log "*qDb*" plot and K1X model fit for the two-phase gas-water flow problem in the Marcellus shale, base case.

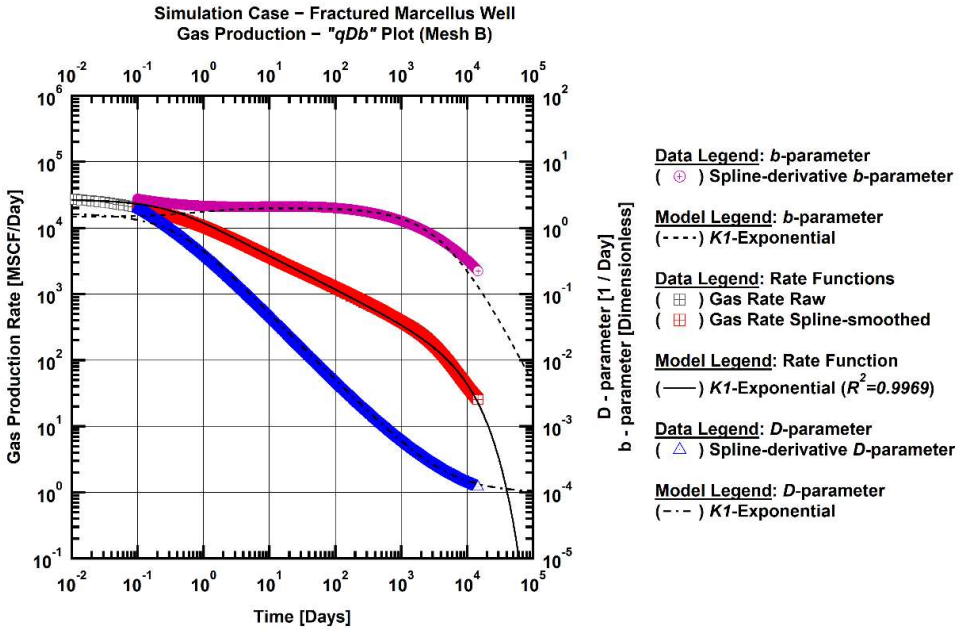

Figure 5.13— Log-log "*qDb*" plot and K1X model fit for the two-phase gas-water flow problem in the Marcellus shale, Mesh B case.

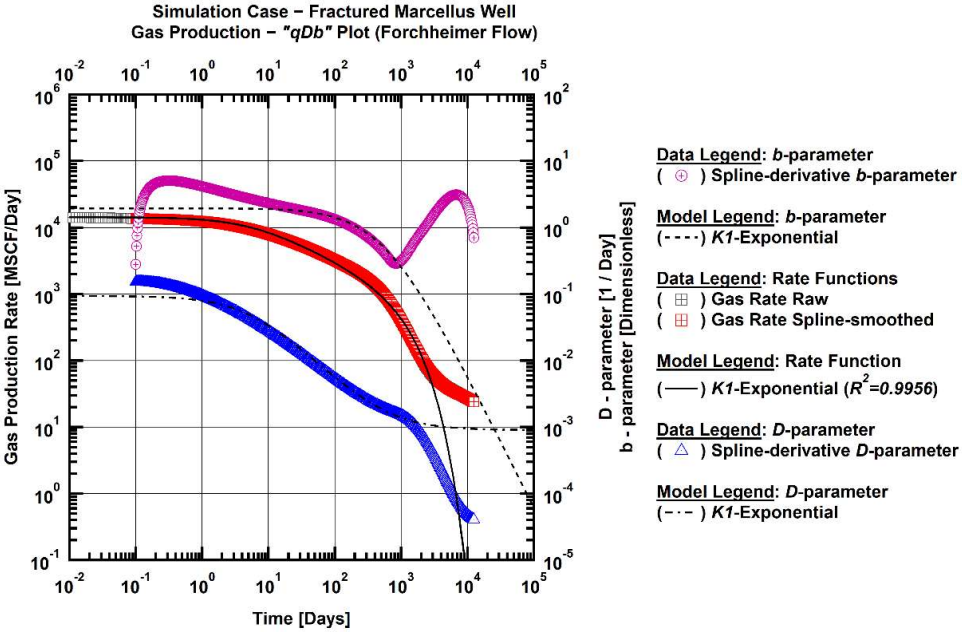

Figure 5.14— Log-log "*qDb*" plot and K1X model fit for the two-phase gas-water flow problem in the Marcellus shale, Forchheimer flow case.

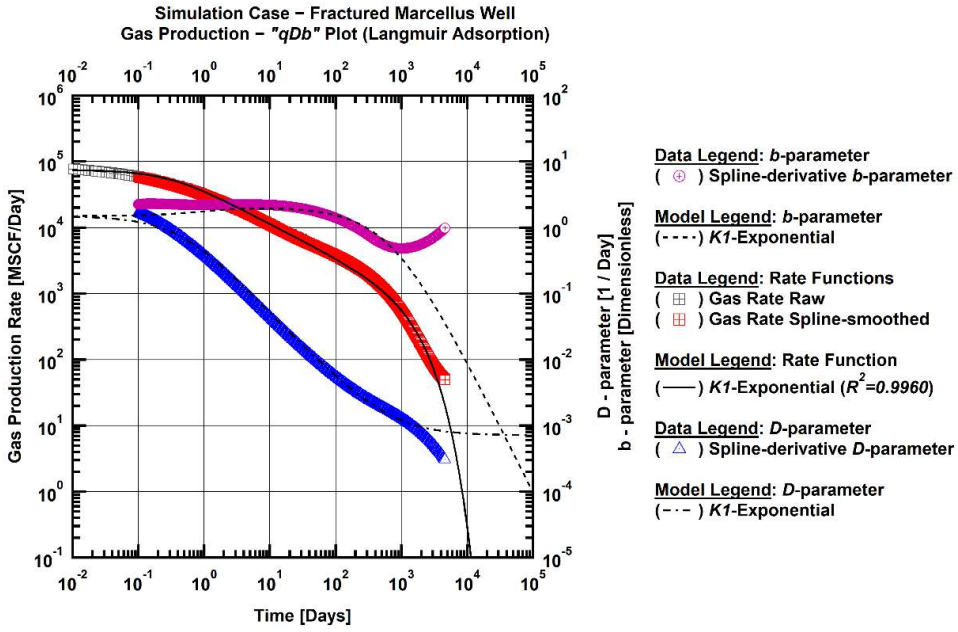

Figure 5.15— Log-log "*qDb*" plot and K1X model fit for two-phase gas-water flow in the Marcellus shale, Langmuir Adsorption case.

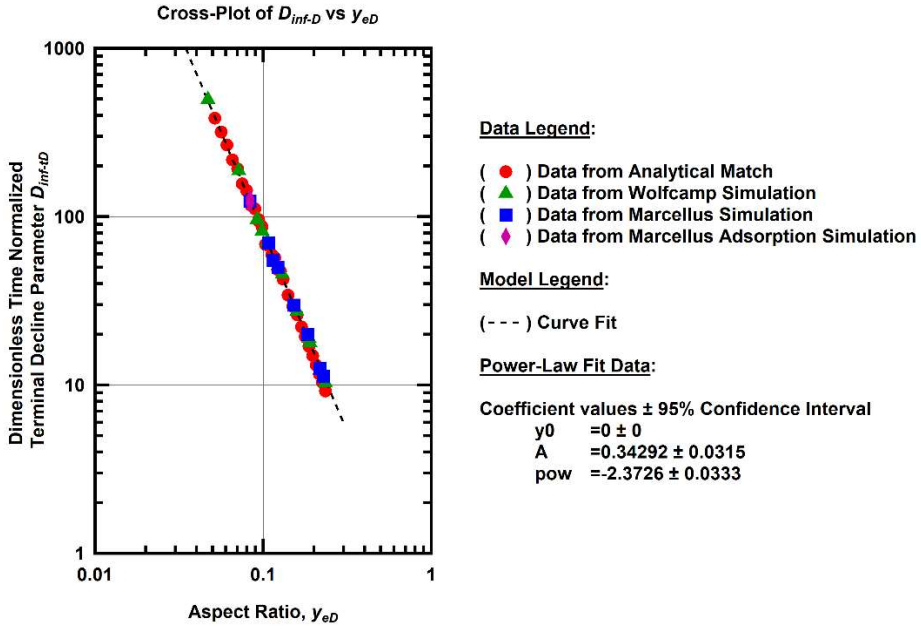

Figure 5.16— Log-log Cross-plot of the $D_{\inf -D}$-parameter vs. the aspect ratio y_{eD} from the K1X model fit of the Wolfcamp simulation cases, Marcellus simulation cases and Olarewaju and Lee (1989) analytical solution.

I propose the following correction to the dimensionless time group (**Eq. 5.7**) to incorporate the effect of adsorption on the terminal decline demonstrated in **Fig. 4.25**:

$$\tau_D = \frac{k}{\left(\phi + \phi_a\right)\mu c_t {x_f}^2}, \quad \text{.....(5.10)}$$

where

$$\phi_a = \left(1-\phi\right)\frac{\rho_R}{\rho_g}\frac{\rho_{sc} V_L p_L}{p + p_L}. \quad \text{.....(5.11)}$$

Fig. 5.16 indicates that **Eq. 5.9** holds true for the mechanistic cases, suggesting that the K1X model is a form of an analytical solution for the 3D-stencil. I am not yet able to mathematically prove that the K1X is indeed an analytical solution, however, I believe that I established a relationship of the model parameter to the reservoir and fluid properties, as well as to the system geometry, and demonstrated it using the analytical solution of Olarewaju and Lee (1989) and the numerical cases that I investigated in this work.

For the sake of consistency, I performed the same analysis using the Modified Hyperbolic and the Power-Law Exponential DCA models. The results are shown on the **Figs. 5.17** and **5.18**, respectively. The mathematical formulation of the terminal decline parameter for the Modified Hyperbolic is given by:

$$D_{\text{lim},MHYP} = 1.3386\frac{k}{\phi\mu c_t {x_f}^2} {y_{eD}}^{-2.1373} \quad \text{.....(5.12)}$$

The correlation for the Power-Law Exponential is given by:

$$D_{\text{inf,PLE}} = 0.16892\frac{k}{\phi\mu c_t {x_f}^2} {y_{eD}}^{-2.5851}. \quad \text{.....(5.13)}$$

The overall correlations seem to be well defined. However, there is a number of outliers in **Fig. 5.17** corresponding to the Wolfcamp larger spacing cases (e.g. **Fig. 4.5**). The outliers are due to the inability of the least-squares curve-fitting algorithm to capture the terminal decline behavior at very early stages for the Modified Hyperbolic DCA model. This is not an issue in the K1X and PLE models because these can obtain the decline trend from the *D*- and *b*- parameters.

The correlations depicted on **Figs. 5.16-5.18** can be used to predict the terminal decline parameters from the reservoir, fluid and geometric properties.

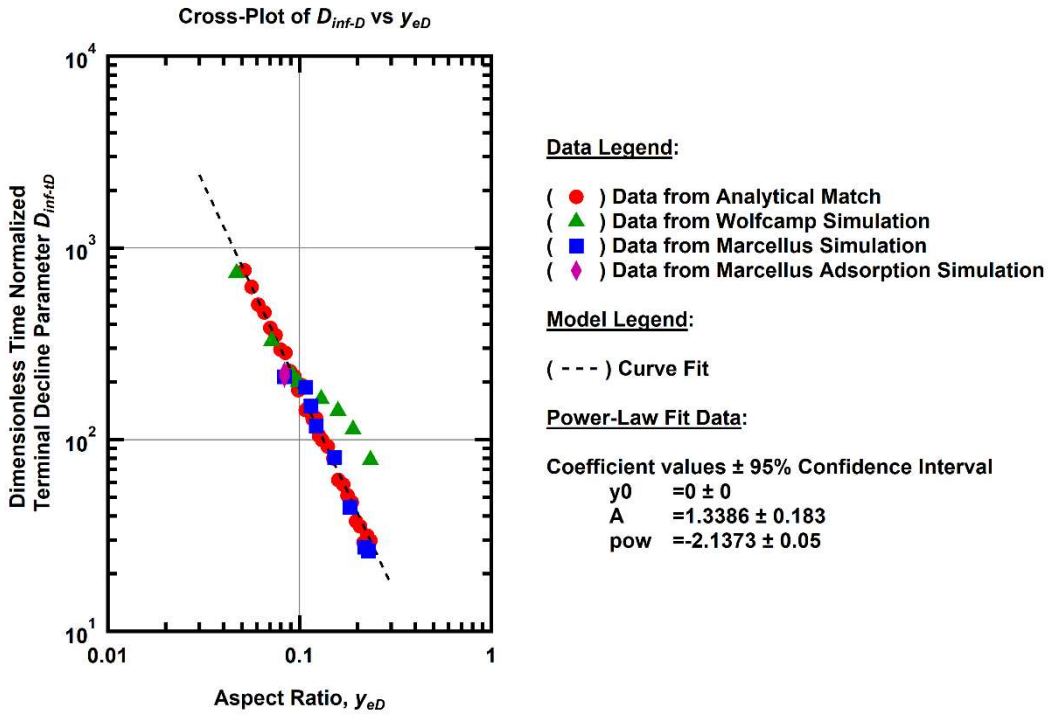

Figure 5.17— Log-log Cross-plot of the $D_{\inf-D}$ -parameter vs the aspect ratio y_{eD} from the Modified Hyperbolic DCA model fit of the Wolfcamp simulation cases, the Marcellus simulation cases and the Olarewaju and Lee (1989) analytical solution.

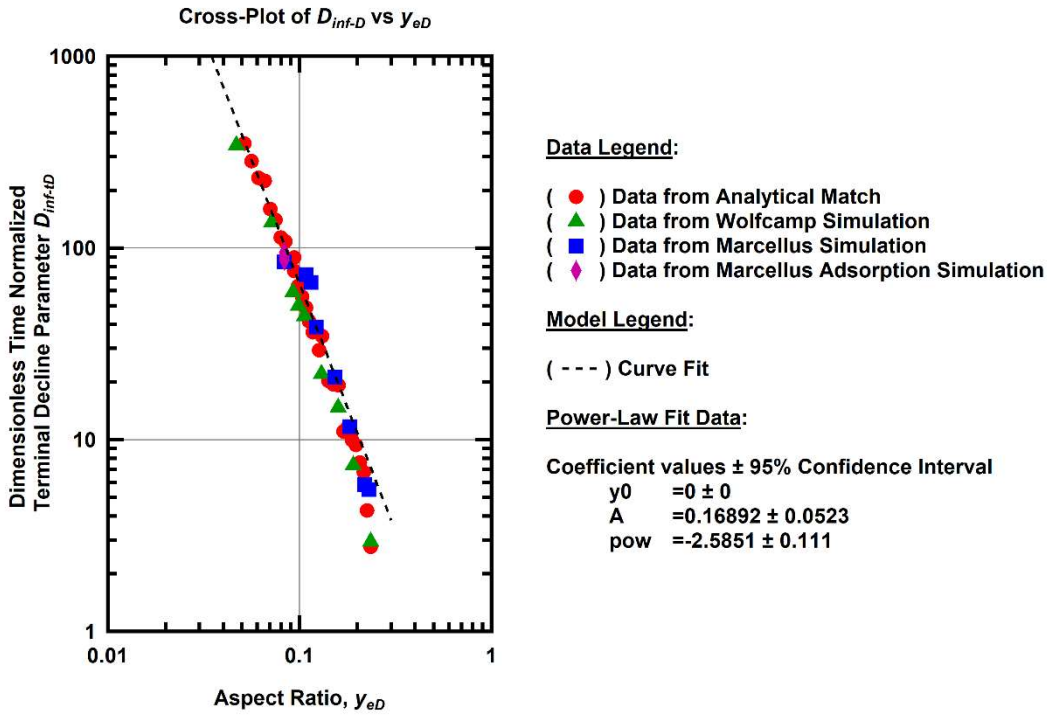

Figure 5.18— Log-log Cross-plot of the $D_{\inf-D}$-parameter vs the aspect ratio y_{eD} from the Power-Law Exponential DCA model fit of the Wolfcamp simulation cases, the Marcellus simulation cases and the Olarewaju and Lee (1989) analytical solution.

5.4 Validation Against Field Data

In this section I test the performance of the K1X model on the field data. Unfortunately, I have been unable to find publicly available production data with sufficient parameters to test **Eq. 5.9**. However, I can use another advantage of the K1X model – the characteristic behavior of the *D*- and *b*- parameters. Production data often need to be smoothed and edited in order to develop representative *D*- and *b*-functions. I describe my own methodology for preprocessing highly distorted daily-production data below.

I begin the data preprocessing procedure by calculating a weekly-average rate-time series from the daily production data. Then, I perform a numerical integration to calculate the cumulative production time series. The next step is to fit a smoothing spline *S* through the cumulative data in the following manner:

$$S = f\left[\log(Q), \log(t)\right], \quad (5.14)$$

If our spline representation of the cumulative data is accurate, the following relation holds for the derivative of the spline:

$$\frac{dS}{d\log(t)} = \frac{\mathrm{d}\log(Q)}{\mathrm{d}\log(t)}, \quad (5.15)$$

Because a spline is a piecewise polynomial function by definition, it is fairly easy to compute the derivatives of a spline, and most of programming environments have library functions for computing such spline derivatives. Denoting the spline derivative as *S′*, I apply the chain rule to **Eq. 5.15** to obtain:

$$S' = \frac{\mathrm{d}\log(Q)}{\mathrm{dt}} \frac{dt}{\log(t)} \quad (5.16)$$

Applying the derivatives to **Eq. 5.16** yields:

$$S' = \frac{q}{Q} t \,. \quad (5.17)$$

Rearranging **Eq. 5.17** for rate results in:

$$q = \frac{QS'}{t} \,. \quad (5.18)$$

The smoothed rate-time series from this procedure can be now used for calculating the *D*- and *b*-parameters.

This technique was applied to the poor-quality data from the South Texas Wells A and B, and from the East Texas Gas Well A. The results of the smoothing and fitting the K1X model to the field data are presented in **Figs. 5.19-5.24**.

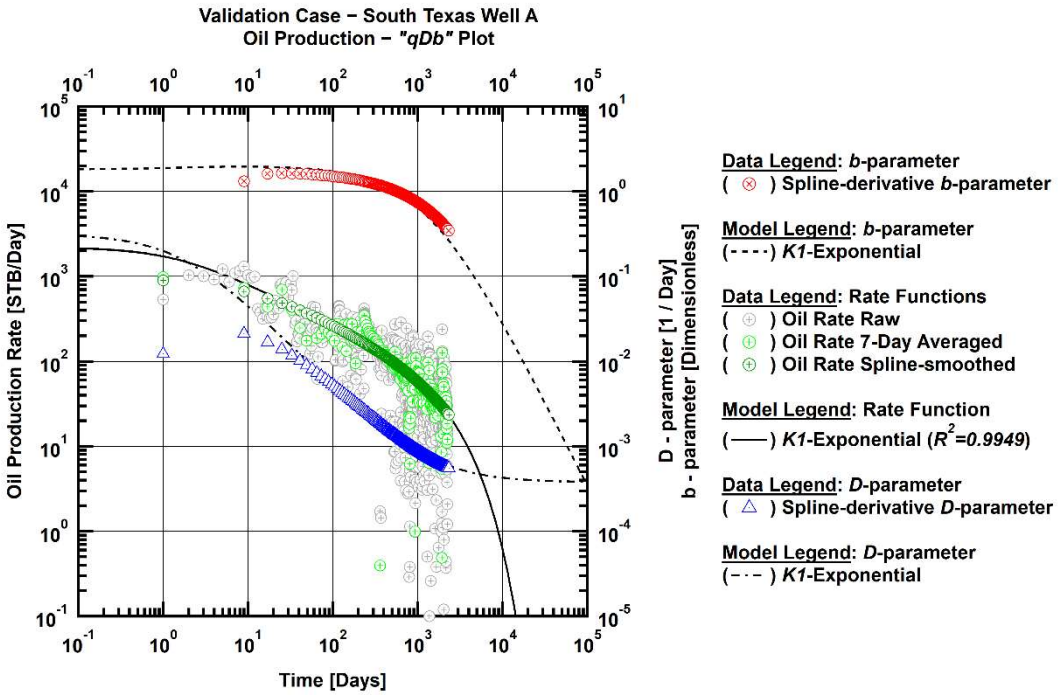

Figure 5.19— Log-log "*qDb*" plot and K1X model fit for the three-phase oil flow problem in the South Texas Well A.

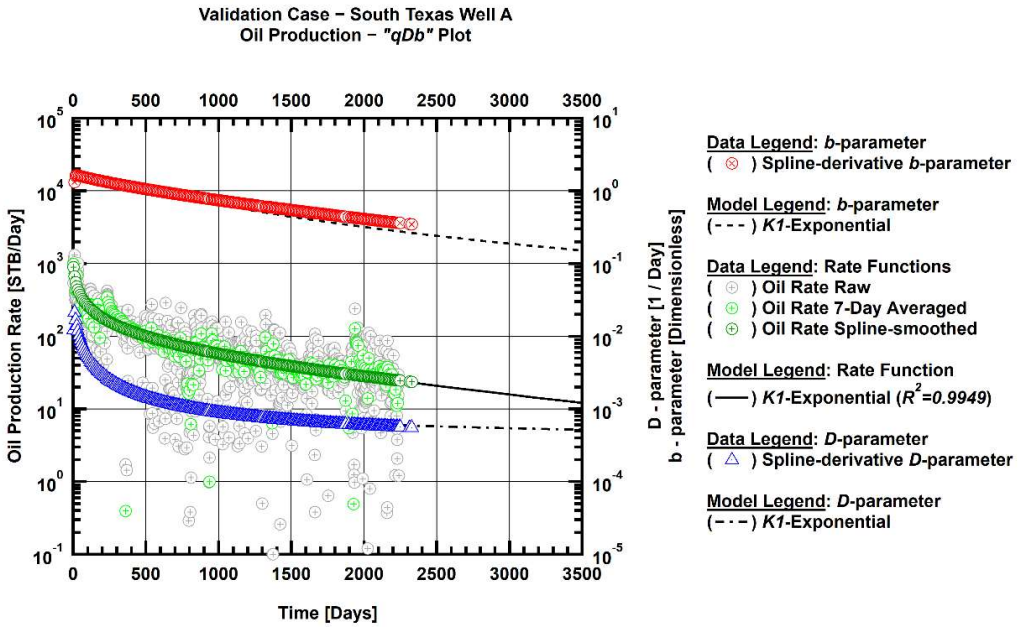

Figure 5.20— Semi-log "*qDb*" plot and K1X model fit for the three-phase oil flow problem in the South Texas Well A.

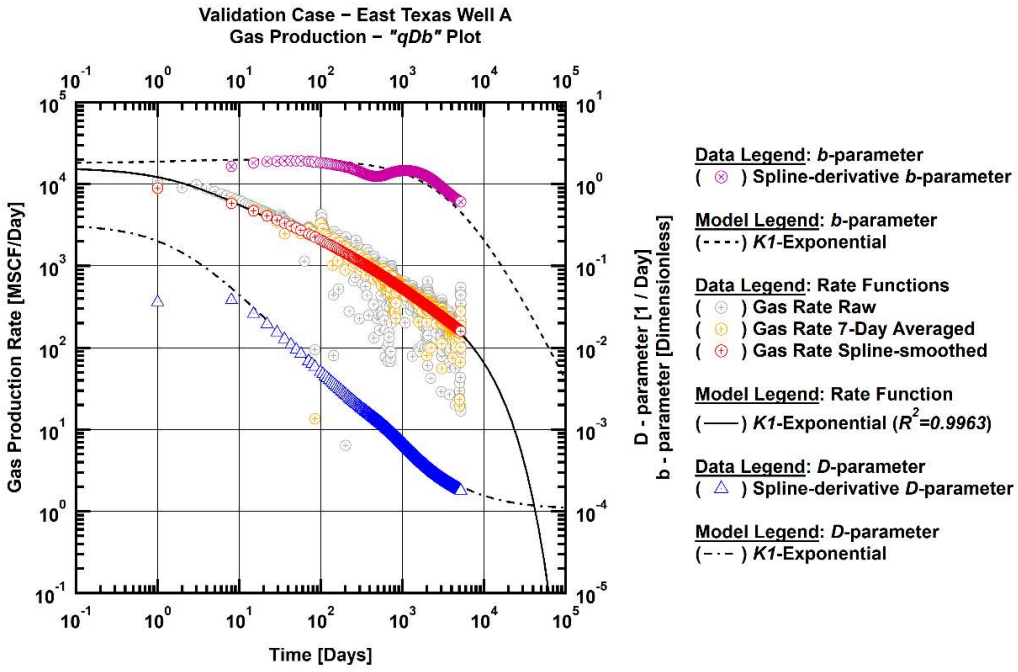

Figure 5.21— Log-log "*qDb*" plot and K1X model fit for the gas flow problem in the East Texas Well A.

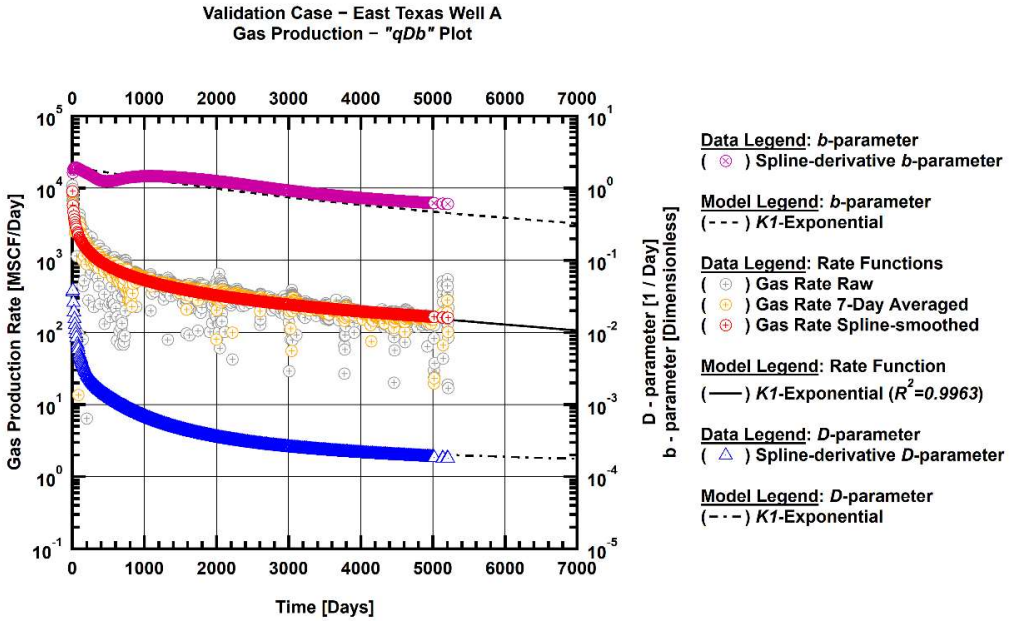

Figure 5.22— Semi-log "*qDb*" plot and K1X model fit for the gas flow problem in the East Texas Well A.

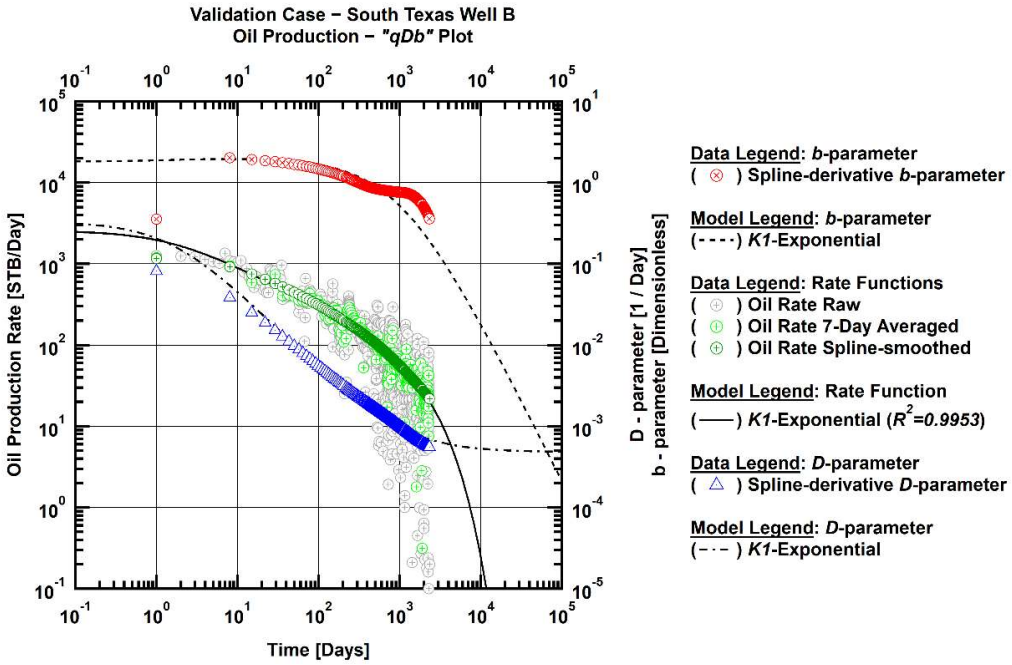

Figure 5.23— Log-log "*qDb*" plot and K1X model fit for the three-phase oil flow problem in the South Texas Well B.

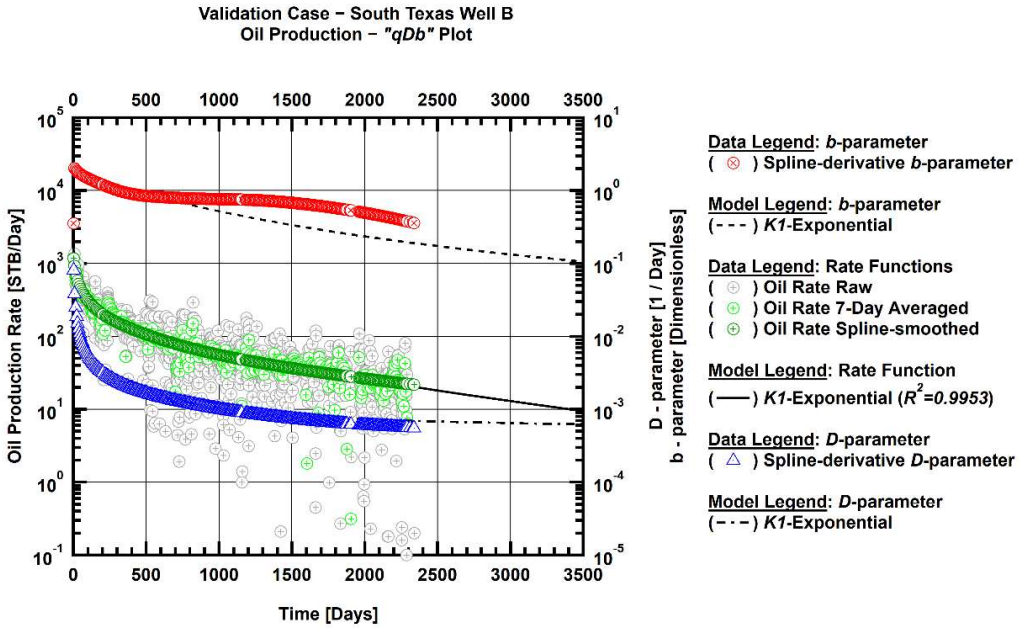

Figure 5.24— Semi-log "*qDb*" plot and K1X model fit for the three-phase oil flow problem in the South Texas Well B.

5.5 Comparison to Standard Decline Models

In this section, the proposed K1X model is compared to the industry *standard* models: the Modified Hyperbolic (MHYP) and the Power-Law Exponential (PLE) applied to the mechanistic and the field cases.

It is important to mention the metric used to describe the model *goodness of fit*. The standard measure of a model fit is the coefficient of determination R^2, given by:

$$R^2 = 1 - \frac{SS_{err}}{SS_{tot}}, \quad \text{.....(5.19)}$$

$$SS_{err} = \sum_{i=1}^{N} \left(y_i - \hat{y}_i \right)^2, \quad \text{.....(5.20)}$$

$$SS_{tot} = \sum_{i=1}^{N} \left(y_i - \bar{y} \right)^2, \quad \text{.....(5.21)}$$

where y is the observed data vector, $\hat{y}_i$ is the predicted data vector and $\bar{y}$ is the mean of the observed data, given by:

$$\bar{y} = \frac{1}{N}\sum_{i=1}^{N} y_i \quad \text{.....(5.22)}$$

However, this is not the best metric for our specific problem that involves rapidly declining functions, because the sums of squares in **Eqs. 5.20-5.21** and the mean in the **Eq. 5.22** will be inflated by the large values of the early-time rates. On the other hand, the contribution of the late time rates in the sums of squares and in the mean will be minimal, meaning that the best fit of the early-time data will yield the highest R^2. To equalize the impact of the data on the statistic, I modified **Eqs. 5.20-5.22** in the following manner:

$$SS_{err} = \sum_{i=1}^{N}\left(\log(y_i) - \log(\hat{y}_i)\right)^2 , \quad \text{.....(5.23)}$$

$$SS_{tot} = \sum_{i=1}^{N}\left(\log(y_i) - \bar{y}\right)^2 , \quad \text{.....(5.24)}$$

$$\bar{y} = \frac{1}{N}\sum_{i=1}^{N}\log(y_i) . \quad \text{.....(5.25)}$$

Figs. 5.25-5.26 show the comparison of the goodness of fit of the various models in the "*qDb*" format using the Wolfcamp simulation cases. **Figs. 5.27-5.30** present the comparison of the goodness of fit of the models in the "*qDb*" format using the Marcellus simulation cases. **Figs. 5.31-5.36** show the comparison of the fit of the models in the "*qDb*" format using the field cases described in the previous section.

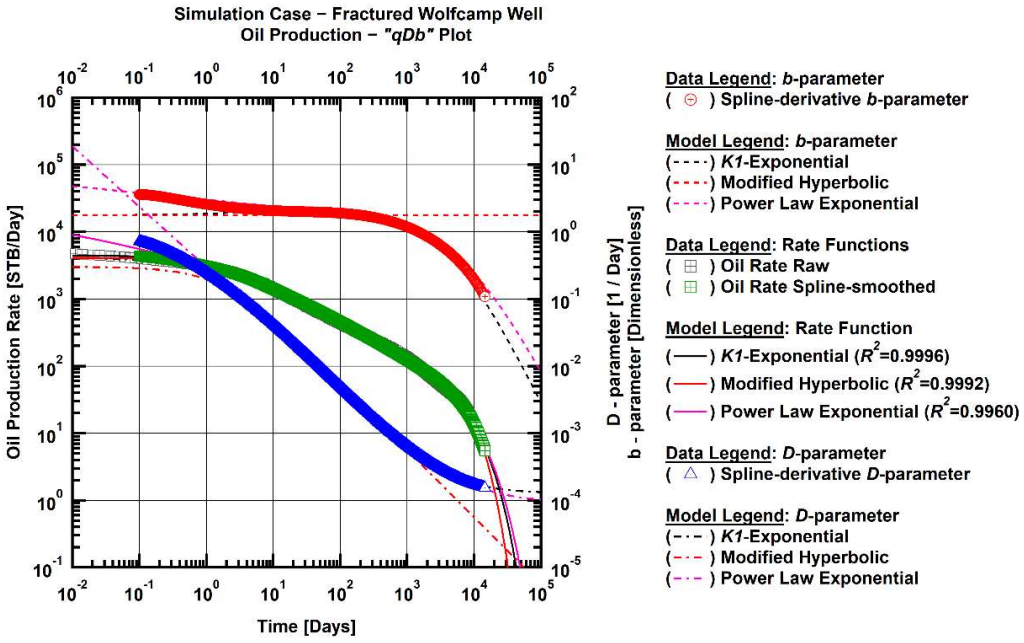

Figure 5.25— Log-log "*qDb*" plot and DCA model fit for the three-phase black-oil flow problem in the Wolfcamp shale (base case).

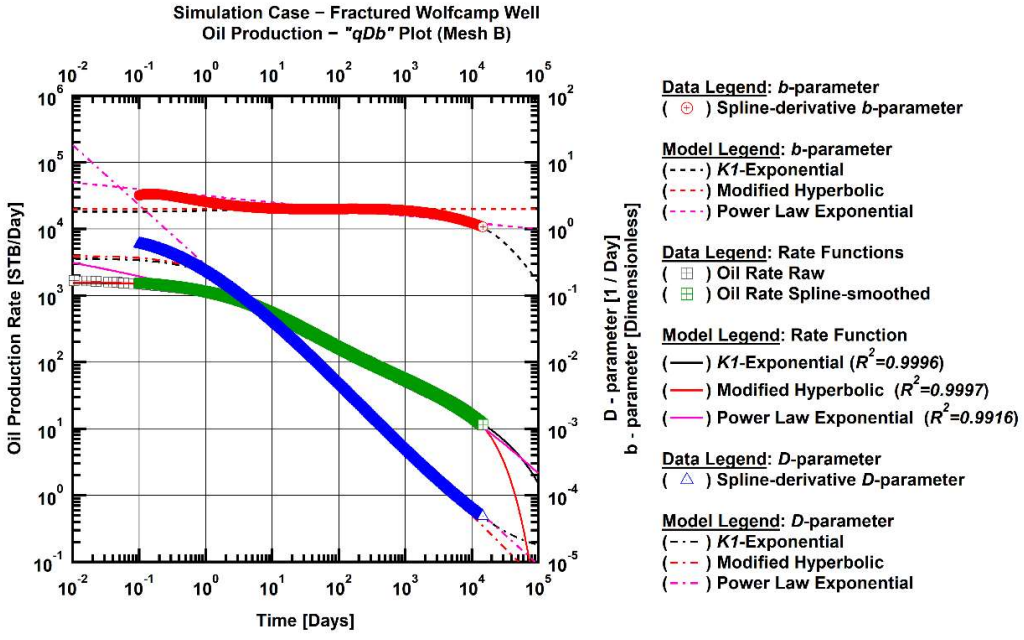

Figure 5.26— Log-log "*qDb*" plot and DCA model fit for the three-phase black-oil flow problem in the Wolfcamp shale (Mesh B).

In the Wolfcamp simulation cases that are shown in **Figs. 5.25-5.26**, all the models yield very high R^2 values that are larger than 0.99. That does not mean however that all of them predict the same EUR. For example, the MHYP fit shown in **Fig. 5.26** clearly underestimates production for the reasons mentioned in **Section 5.3**.

In the Marcellus simulation cases that are shown in **Figs. 5.27-5.30,** all the models also yield very high R^2 values that exceed 0.99. The EUR discrepancies are minimal for the gas-water cases. K1X provides the best representation of the *D*- and *b*-parameter functions compared to the standard models. In fact, the K1X model accurately describes the behavior of the derivatives until the onset of the compound linear flow at very late times.

The field cases described in **Figs. 5.31-5.33** also yield R^2 values larger than 0.99 and similar EUR predictions. The more complicated case described by **Figs. 5.34-5.35** shows overfitting of the PLE model. Automatic fitting algorithm ignore the slope change described by the stepwise change in the *b*-parameter from two to one, leading to overestimation of recovery.

Comparison of the K1X model to the MHYP and PLE models leads to the following conclusions:

- Given a full production history with established terminal decline, all three models can accurately model the production rate behavior of a multi-fractured horizontal well in an unconventional (ultra-tight) reservoir with R^2 greater than 0.99.
- Without the established terminal decline or the estimate from **Eq. 5.12**, MHYP cannot accurately predict ultimate recovery and should not be used for diagnostics.

- Both K1X and PLE can be used for EUR estimation when the terminal decline is signaled by the derivative functions *D*- and *b*- parameters.
- PLE model can be subject to overfitting because of the power-law behavior of the model *b*- parameter, unsupported by the mechanistic model.
- Without sufficient production data to signal the terminal decline in the *D*- and *b*- parameters, the EUR should be estimated using the correlations given by **Eqs. 5.9, 5.12, 5.13**.
- K1X appears to be the most powerful model out of three, as it captures and models the characteristic behavior of the rate function as well as the characteristic behavior of the derivative functions *D*- and *b*- parameters.

Further study of the K1X model revealed that it may be approximated by a much simpler limiting form, not involving special functions. The full derivation of the limiting form, as well as the comparison to the original K1X model is given in **Appendix C**. The limiting form of K1X can be easily extended to model other forms of transient flow regimes. The extended form is given in **Appendix D**.

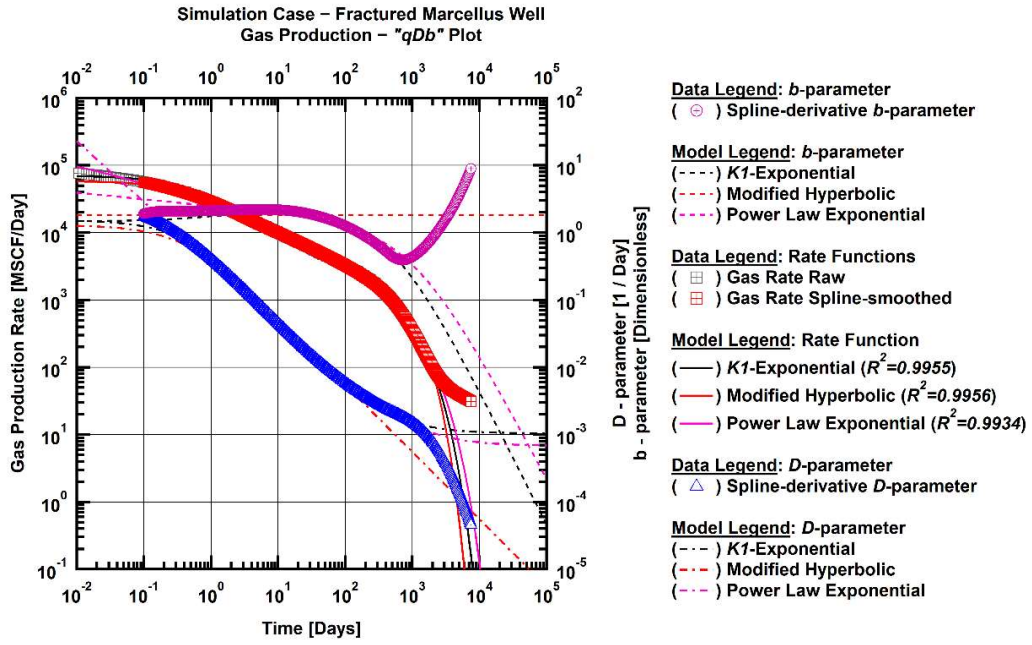

Figure 5.27— Log-log "*qDb*" plot and DCA model fit for the two-phase gas-water flow problem in the Marcellus shale (base case).

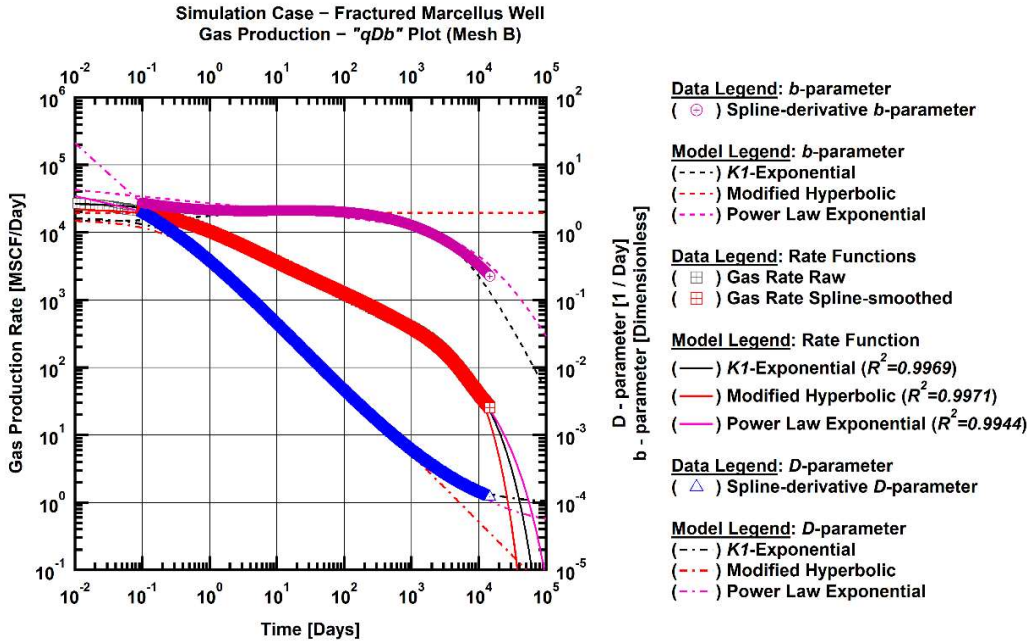

Figure 5.28— Log-log "*qDb*" plot and DCA model fit for the two-phase gas-water flow problem in the Marcellus shale (Mesh B).

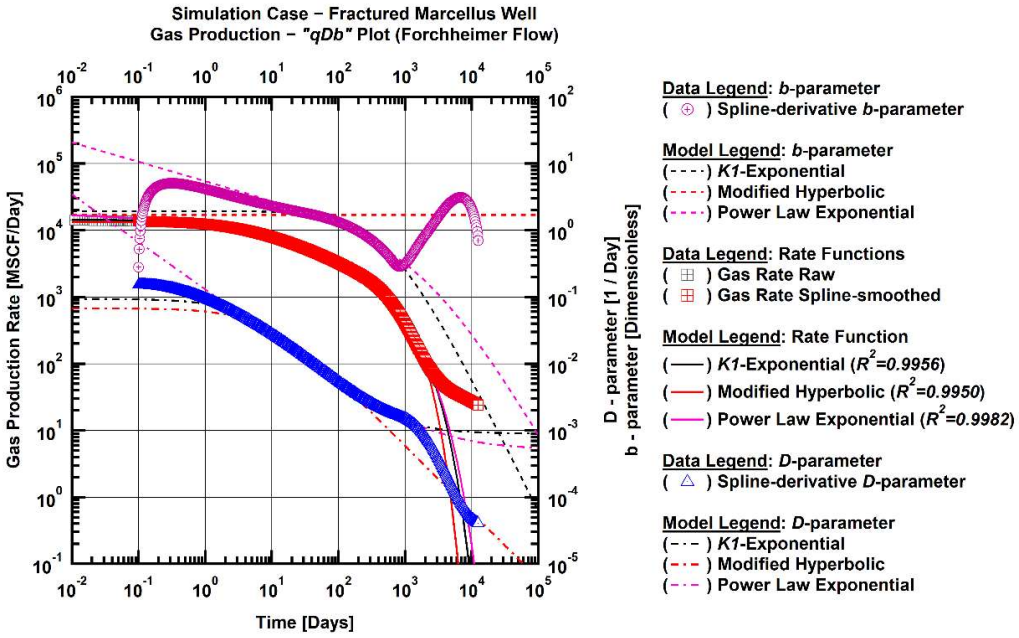

Figure 5.29— Log-log "*qDb*" plot and DCA model fit for the two-phase gas-water flow problem in the Marcellus shale (Forchheimer Flow).

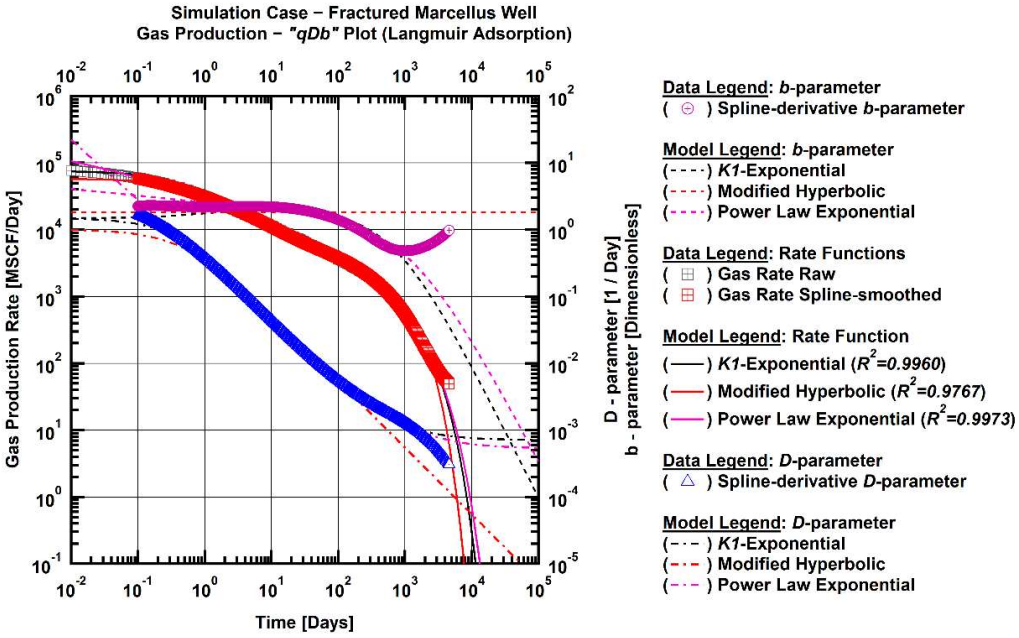

Figure 5.30— Log-log "*qDb*" plot and DCA model fit for the two-phase gas-water flow problem in the Marcellus shale (Langmuir Adsorption).

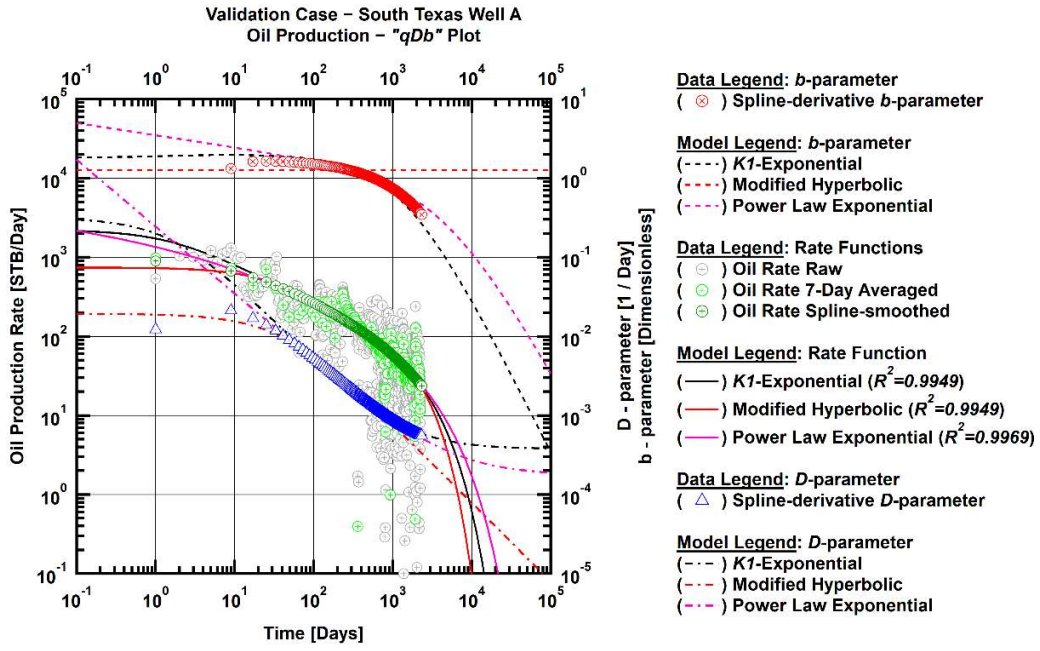

Figure 5.31— Log-log "*qDb*" plot and DCA model fit for the three-phase oil flow problem in the South Texas Well A.

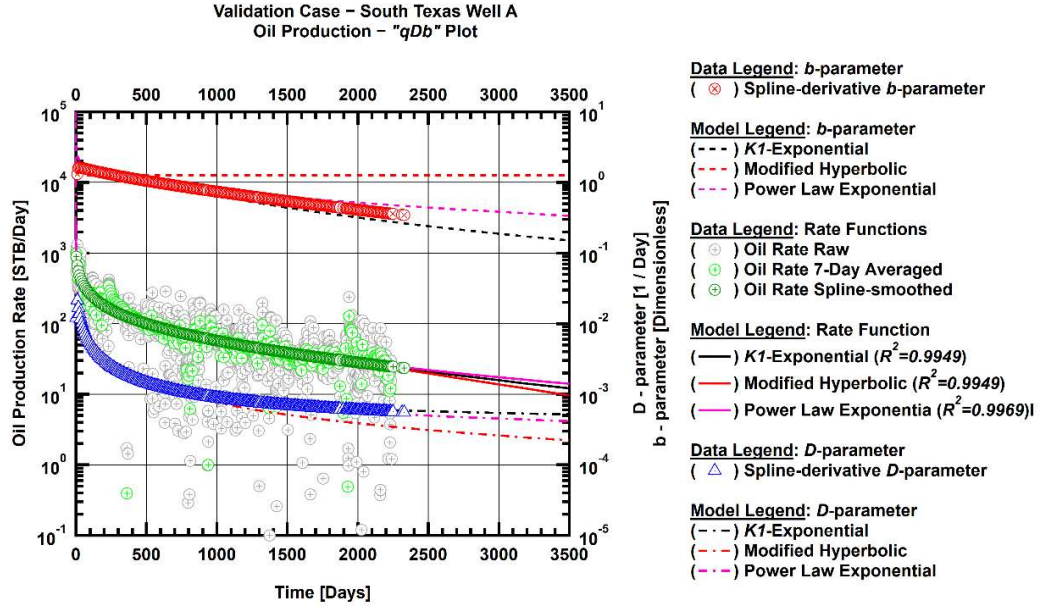

Figure 5.32— Semi-log "*qDb*" plot and DCA model fit for the three-phase oil flow problem in the South Texas Well A.

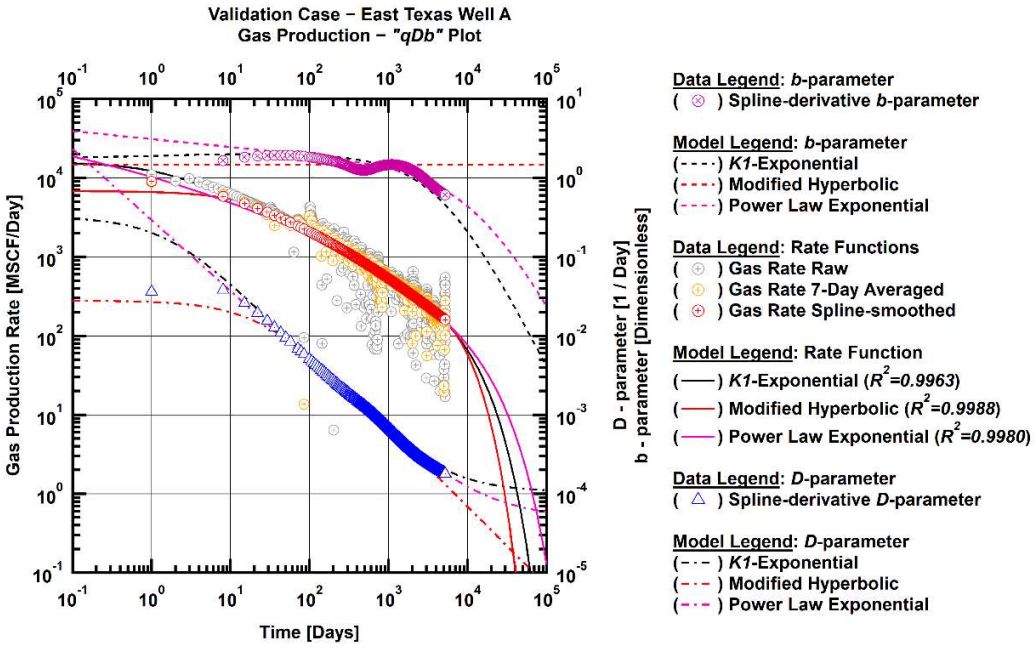

Figure 5.33— Log-log "*qDb*" plot and DCA model fit for the gas flow problem in the East Texas Well A.

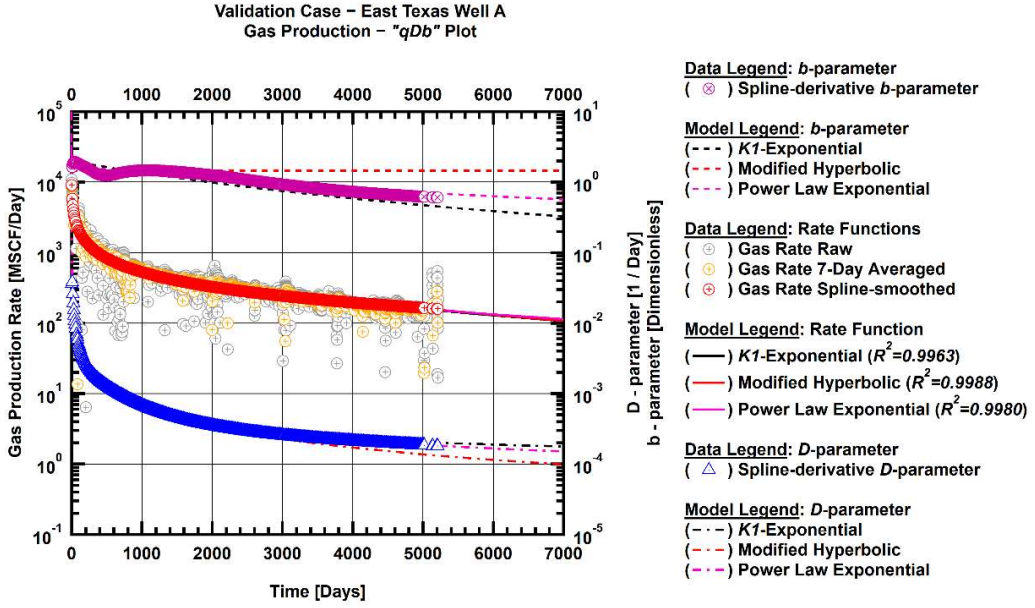

Figure 5.34— Semi-log "*qDb*" plot and DCA model fit for the gas flow problem in the East Texas Well A.

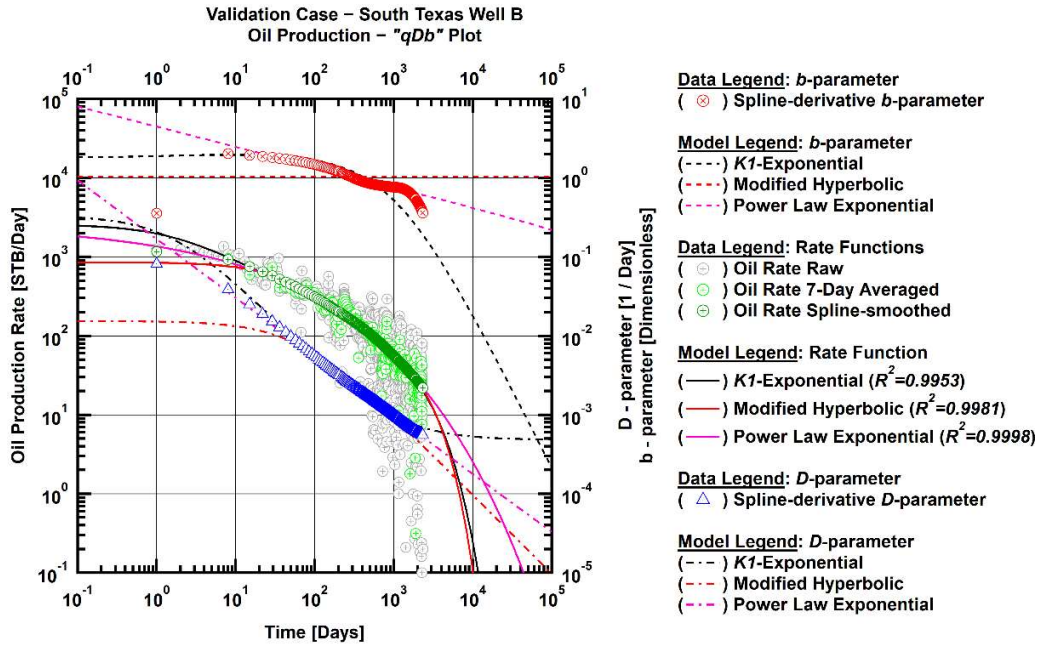

Figure 5.35— Log-log "*qDb*" plot and DCA model fit for the three-phase oil flow problem in the South Texas Well B.

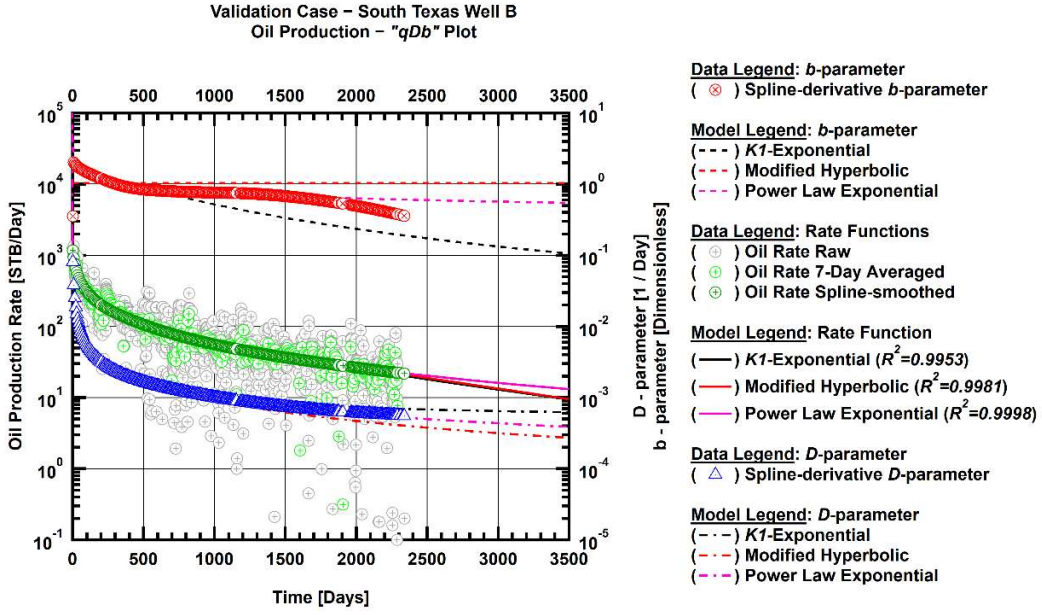

Figure 5.36— Semi-log "*qDb*" plot and DCA model fit for the three-phase oil flow problem in the South Texas Well B.

CHAPTER VI

SUMMARY AND CONCLUSIONS

6.1 Summary

In this work I developed a mechanistic (stencil-based) model for a multi-fractured horizontal well in unconventional (*i.e.,* ultra-low permeability) reservoirs. The model was validated using the Olarewaju and Lee (1989) analytical solution. The model was used to generate production profiles for a 3-phase black-oil flow problem in the Wolfcamp shale oil play, and for the 2-phase gas-water flow problem in the Marcellus shale gas reservoir. Five flow regimes were successfully generated:

- Early-time *fracture-dominated performance* (*i.e.,* fracture (water) unloading).
- *Linear flow* regime (*i.e.,* non-interferring fractures).
- *Transitional flow* behavior, from linear flow to boundary-dominated flow.
- Late-time *boundary-dominated flow*.
- Late-time *compound linear flo*w regime.

For completeness, a large variety of stencil configurations and reservoir and fluid properties were evaluated for a wide range of black-oil and dry gas reservoir cases.

In addition to various *mechanistic effects*, I also investigated the effect of spatial discretization on the production predictions and concluded that coarser gridding yields higher production of the wetting phase in the 3-phase black oil and the 2-phase gas-water cases.

The non-mechanistic behavior scenarios that I modeled included:

- Early-time performance dominated by very high-water production (*i.e.,* flowback).
- Degradation of fracture permeability during well production.
- Non-laminar flow.
- Effects of gas adsorption.

I proposed a *K_1-Exponential* (K1X) DCA model based on the results generated in this work. The K1X model was validated against the analytical solution and the mechanistic cases. This model was also compared to the *standard* DCA models that include the Modified Hyperbolic (MHYP) and Power Law Exponential (PLE) models, and was tested and validated using both synthetic and field well performance data.

Using analytical solutions and data from simulation cases, I developed a correlation for the estimation of the terminal decline parameter for the K1X model from reservoir and fluid properties, as well as geometric characteristics of the system. I also developed similar correlations for the MHYP and the PLE models.

I also derived a *limiting form* (approximation) of the K1X model and demonstrated its accuracy. Based on the limiting form of the K1X model, I proposed a *generalized form*. Both the limiting form and the generalized form models appear to have theoretical bases (see **Appendices B, C, and D**).

6.2 Conclusions

Parametric studies of the analytical, mechanistic, and non-mechanistic cases helped determine the geometric, reservoir and fluid properties that affect the late-time terminal decline behavior. These include:

- The stencil aspect ratio (fracture spacing)
- The fracture half-length
- The reservoir porosity and permeability
- The total compressibility
- The fluid viscosity
- The Langmuir adsorption parameters (Langmuir volume and Langmuir pressure)

All the other mechanistic and non-mechanistic parameters and scenarios were found to have minor to negligible effects and/or to only affect the early-time performance — these include:

- The fracture height
- The fracture conductivity
- The early-time water flowback from the fracture
- The fracture permeability degradation
- Non-laminar flow

My in-depth study of the effect of spatial discretization on the accuracy of the numerical solution revealed that the use of coarser grids leads to a significant overprediction of the wetting phase production.

I proposed a new *K_1-Exponential* (K1X) DCA model based on results generated in this work. The primary form of this model (based on the $K_1(x)$ and $\exp(x)$ functions) is shown to match the expected flow regimes very well. The K1X DCA model was tested against the analytical solution, as well as to the *standard* DCA models, i.e., the Modified Hyperbolic and the Power-Law/Stretched Exponential model, and performed as well or better in the prediction of the phase flow rate, as well as in the description of the *D*- and *b*-parameter functions. There were very few cases where this model did not produce a superior match of the data, hinting that the K1X DCA model may become a standard for the analysis and interpretation of time-rate data from wells in unconventional reservoirs.

In addition to the comparative performance studies, I conducted another to develop correlations estimating the terminal decline parameters for the K1X, Modified Hyperbolic, and Power-Law Exponential DCA models. Conceptually, the proposed correlations can be used for reserves estimation in unconventional plays and for fracture spacing design.

The appearance of a modified Bessel function in the proposed model suggests a relation to a form of analytical solution to diffusivity equation for a fractured well (*e.g.*, the Ozkan and Raghavan solution (1988)). A significant effort was made to mathematically establish the K1X DCA model as either an analog to, or a part of an analytical solution. no uniquely theoretical (analytical) result could be obtain. However, the observation that the K1X DCA model can accurately model the production behavior, as well as its first and second derivative functions, suggests that this method may have an underlying mathematical proof.

In addition, the limiting forms and the general extension formulations of the K1X DCA model (see **Appendices B, C, and D**) suggest a strong relation to an analytical solution/formulation. As an example, the cumulative production expression for the *limiting form* contains error functions, while the cumulative production expression for the *generalized form* contains exponential integrals — both these special functions are found in the real domain solutions of flow in bounded reservoirs, line sources, and fractured wells.

6.3 Recommendations for Future Research

Further investigations of the *K_1-Exponential* (K1X) DCA model should be conducted, with the specific objective of establishing a link to analytical solutions for flow to wells in fractured reservoirs (a wide array of possibilities should be considered, including the case of a multi-fractured horizontal well).

In addition, the *limiting form* of the K1X model should be deconstructed to provide a theoretical proof that this form represents an analytical solution or approximation to the rectangular reservoir problem. Lastly, the proposed correlations for the terminal decline parameters should be tested and validated against field data.

REFERENCES

Abramowitz, M., & Stegun, I. A. (1970). Handbook of Mathematical Functions with Formulas, Graphs, and Mathematical Tables. Washington, D.C.: United States Government Printing Office.

Ali, W. (2012). Modeling Gas Production from Shales and Coal-Beds (M.Sc. Thesis). Energy Resources Engineering Department, Stanford University.

Arps, J.J. (1945). Analysis of Decline Curves. Trans. AIME 160: 228–247.

Chung, T. H., Lee, L. L., & Starling, K. E. (1984). Applications of Kinetic Gas Theories and Multiparameter Correlation for Prediction of Dilute Gas Viscosity and Thermal Conductivity. Industrial & Engineering Chemistry Fundamentals, 23(1), 8–13. doi: 10.1021/i100013a002.

Chung, T. H., Ajlan, M., Lee, L. L., & Starling, K. E. (1988). Generalized Multiparameter Correlation for Nonpolar and Polar Fluid Transport Properties. Industrial & Engineering Chemistry Research, 27(4), 671–679. doi: 10.1021/ie00076a024

Dietrich, J. K., & Bondor, P. L. (1976). Three-Phase Oil Relative Permeability Models. SPE Annual Fall Technical Conference and Exhibition. doi: 10.2118/6044-MS

Economou, I. G., Heidman, J. L., Tsonopoulos, C., & Wilson, G. M. (1997). Mutual Solubilities of Hydrocarbons and Water: III. 1-Hexene; 1-Octene; C10-C12 Hydrocarbons. AIChE Journal, 43(2), 535–546. doi: 10.1002/aic.690430226

Egbogah, E.O., Ng, J.T. (1990). An Improved Temperature-Viscosity Correlation for Crude-Oil Systems. J. Pet. Sci. Eng. 4 (3): 197–200. doi:10.1016/0920-4105(90)900009-R

El Sgher, M., Aminian, K., & Ameri, S. (2018). The Impact of Stress on Propped Fracture Conductivity and Gas Recovery in Marcellus Shale. Society of Petroleum Engineers. doi:10.2118/189899-MS

Forchheimer, P. (1901). Wasserbewegung durch Boden, ZVDI. Vol. 45, 1781.

Frederick, D., & Graves, R. (1994). New Correlations to Predict Non-Darcy Flow Coefficients at Immobile and Mobile Water Saturation. SPE Annual Technical Conference and Exhibition. doi: 10.2118/28451-MS

Freeman, C. M., Moridis, G. J., & Blasingame, T. A. (2011). A Numerical Study of Microscale Flow Behavior in Tight Gas and Shale Gas Reservoir Systems. Transport in Porous Media, 90 (1), 253–268. doi: 10.1007/s11242-011-9761-6

Gringarten, A. C., Ramey, H. J., & Raghavan, R. (1974). Unsteady-State Pressure Distributions Created by a Well with a Single Infinite-Conductivity Vertical Fracture. Society of Petroleum Engineers Journal, 14(04), 347–360. doi: 10.2118/4051-PA

de Hemptinne, J-C, Dhima, A., Shakir, S. (2000). The Henry Constant for 20 hydrocarbons, CO2 and H2S in Water as a Function of Pressure and Temperature. Paper presented at the Fourteenth Symposium on Thermophysical Properties, Boulder, CO, 25-30 June 2000.

Ilk, D., Rushing, J.A., and Blasingame, T.A. (2009). Decline Curve Analysis for HP/HT Gas Wells: Theory and Applications. Paper SPE 125031 presented at the SPE Annual Technical Conference and Exhibition, New Orleans, LA, 04–07 October 2009.

Ilk, D., Rushing, J.A., Perego, A.D., and Blasingame, T.A. (2008) Exponential vs. Hyperbolic Decline in Tight Gas Sands: Understanding the Origin and Implications for Reserve Estimates Using Arps' Decline Curves. Society of Petroleum Engineers. doi:10.2118/116731-MS.

International Association for the Properties of Water and Steam, IAPWS R6-95(2018), Revised Release on the IAPWS Formulation 1995 for the Thermodynamic Properties of Ordinary Water Substance for General and Scientific Use (2018).

Johnson, R.H. and Bollens, A.L. (1927). The Loss Ratio Method of Extrapolating Oil Well Decline Curves. Trans. AIME 77: 771.

Katz, D. L., et al, (1959). Handbook of Natural Gas Engineering. New York: McGraw-Hill.

Kohlrausch, R. (1854). Theorie des elektrischen Rückstandes in der Leidner Flasche. Annalen Der Physik Und Chemie. 91 (1): 56–82, 179–213. doi:10.1002/andp.18541670103.

Langmuir, I. (1918). The Adsorption of Gases on Plane Surfaces of Glass, Mica and Platinum. J. Am. Chem. Soc. 40: 1361-1403. https://doi.org/10.1021/ja02242a004.

Lee, S.-T., & Brockenbrough, J. R. (1986). A New Approximate Analytic Solution for Finite-Conductivity Vertical Fractures. SPE Formation Evaluation, 1(01), 75–88. doi: 10.2118/12013-PA

Moridis, G. J., & Freeman, C. M. (2014). The RealGas and RealGasH2O options of the TOUGH+ code for the simulation of coupled fluid and heat flow in tight/shale gas systems. Computers & Geosciences, 65, 56–71. doi: 10.1016/j.cageo.2013.09.010

Narasimhan, T. N., & Witherspoon, P. A. (1976). An integrated finite difference method for analyzing fluid flow in porous media. Water Resources Research, 12(1), 57–64. doi: 10.1029/wr012i001p00057

NIST. (2011). Thermophysical Properties of Fluid Systems. http://webbook.nist.gov/chemistry/fluid/.

Olarewaju, J.S., & Lee, W.J. (1989). A New Analytical Model of Finite-Conductivity Hydraulic Fracture in a Finite Reservoir. SPE Gas Technology Symposium. doi: 10.2118/19093-MS

Olorode, O. (2011). Numerical Modeling and Analysis of Shale-Gas Reservoir Performance Using Unstructured Grids (M.Sc.thesis). Petroleum Engineering Department, Texas A&M University.

Olorode, O.M., Freeman, C.M., G.J. Moridis, and T.A. Blasingame. (2013). High-Resolution Numerical Modeling of Complex and Irregular Fracture Patterns in Shale Gas and Tight Gas Reservoirs, SPE Reservoir Evaluation & Engineering, 16(4), 443–455. https://doi.org/10.2118/152482-PA.

Ozkan, E., & Raghavan, R. (1988). Some New Solutions to Solve Problems in Well Test Analysis: Part 1 - Analytical Considerations. Society of Petroleum Engineers

Parker, J. C., Lenhard, R. J., & Kuppusamy, T. (1987). Correction to "A Parametric Model for Constitutive Properties Governing Multiphase Flow in Porous Media" by J. C. Parker, R. J. Lenhard, and T. Kuppusamy. Water Resources Research, 23(9), 1805–1805. doi: 10.1029/wr023i009p01805

Peng, D. Y.; Robinson, D. B. (1976). "A New Two-Constant Equation of State". Industrial and Engineering Chemistry: Fundamentals. 15: 59–64. doi:10.1021/i160057a011

Poling, B. E., Prausnitz, J. M., & OConnell, J. P. (2007). The Properties of Gases and Liquids (5th ed.). Boston: McGraw-Hill.

Pruess, K., Oldenburg, C., & Moridis, G. (1999). TOUGH2 User's Guide, Version 2.0, Report LBNL-43134, Lawrence Berkeley National Laboratory, Berkeley, California. doi: 10.2172/751729

Raghavan, R. (1993). Well test analysis. Englewood Cliffs, NJ: PTR Prentice Hall.

Robertson, S. (1988). Generalized Hyperbolic Equation. Paper SPE 18731 available from SPE, Richardson, Texas.

Stehfest, H. (1970). Algorithm 368: Numerical Inversion of Laplace Transforms [D5]. Communications of the ACM, 13(1), 47–49. doi: 10.1145/361953.361969

Stone, H.L. (1973). Estimation of Three-Phase Relative Permeability and Residual Oil Data. Journal of Canadian Petroleum Technology, 12(04). doi: 10.2118/73-04-06

Tsonopoulos, C., & Wilson, G. M. (1983). High-Temperature Mutual Solubilities of Hydrocarbons and Water. Part I: Benzene, Cyclohexane and n-Hexane. AIChE Journal, 29(6), 990–999. doi: 10.1002/aic.690290618

Tsonopoulos, C. (1999). Thermodynamic Analysis of The Mutual Solubilities of Normal Alkanes and Water. Fluid Phase Equilibria, 156(1-2), 21–33. doi: 10.1016/s0378-3812(99)00021-7

Valko, P.P. (2009). Assigning Value to Stimulation in the Barnett Shale: A Simultaneous Analysis of 7000 Plus Production Histories and Well Completion Records. Paper SPE 119369 presented at the SPE Hydraulic Fracturing Technology Conference, College Station, TX, 19-21 January 2009.

Valko, P. P., & Lee, W. J. (2010). A Better Way to Forecast Production from Unconventional Gas Wells. Society of Petroleum Engineers. doi:10.2118/134231-MS

Van Everdingen, A. F., & Hurst, W. (1949). The Application of the Laplace Transformation to Flow Problems in Reservoirs. Society of Petroleum Engineers. doi:10.2118/949305-G

Van Genuchten, M. T. (1980). A Closed-form Equation for Predicting the Hydraulic Conductivity of Unsaturated Soils. Soil Science Society of America Journal, 44(5), 892–898. doi: 10.2136/sssaj1980.03615995004400050002x

Vazquez, M., & Beggs, H. D. (1977). Correlations for Fluid Physical Property Prediction. Society of Petroleum Engineers. doi:10.2118/6719-MS

Wattenbarger, R. A., & Ramey, H. J. (1968). Gas Well Testing With Turbulence, Damage and Wellbore Storage. Journal of Petroleum Technology, 20(08), 877–887. doi: 10.2118/1835-PA

Ye, Z., Chen, D., Pan, Z., Zhang, G., Xia, Y., Ding X. 2016.An improved Langmuir model for evaluating methane adsorption capacity in shale under various pressures and temperatures. Journal of Natural Gas Science and Engineering. 31: 658-680.https://doi.org/10.1016/j.jngse.2016.03.070.

NOMENCLATURE

Field Variables

$\tilde{A}$ = Surface area, [m^2]

A_f = Fracture surface area, [m^2] or [ft^2]

a_R = Rock thermal expansivity, [K^{-1}] or [R^{-1}]

B_o = Oil formation volume factor, [RB/STB]

B_{ob} = Oil formation volume factor at the bubble-point conditions, [RB/STB]

b_k = Klinkenberg parameter, [Pa] or [psi]

C = Heat capacity, [J kg^{-1} K^{-1}]

c = Compressibility, [Pa^{-1}] or [psi^{-1}]

D_f = Fracture spacing, [m] or [ft]

F = Mass or heat flux, [kg m^{-2} s^{-1}] or [J m^{-2} s^{-1}]

g = Gravitational acceleration vector, [m/s^2] or [ft/s^2]

H = Phase specific enthalpy, [J/kg]

h = Specific enthalpy of a component in phase, [J/kg]

K = Watson characterization factor, [$K^{1/3}$] or [$R^{1/3}$]

K_n = Knudsen number, [dimensionless]

k = Rock intrinsic permeability tensor, [m^2] or [mD]

k_r = Phase relative permeability, [dimensionless]

M = Mass or heat accumulation, [kg/m^3] or [J/m^3]

MW = Molecular weight

q = Mass or volumetric flow rate, [kg/s] or [STB/day] or [scf/day]

P = Pressure, [Pa] or [psi]

P_c = Phase capillary pressure, [Pa] or [psi]

p = Pressure, [Pa] or [psi]

p_b = Bubble-point pressure, [Pa] or [psi]

p_c = Critical pressure, [Pa] or [psi]

p_L = Langmuir pressure, [Pa] or [psi]

R = Universal gas constant, [J kg^{-1} mol^{-1}]

R_s = Solution gas-oil ratio, [scf/STB]

R_{sb} = Solution gas-oil ratio at the bubble-point conditions, [scf/STB]

S = Phase saturation, [dimensionless]

S_{irr} = Irreducible phase saturation, [dimensionless]

T = Reservoir temperature, [°C] or [°F]

T_c = Critical temperature, [°C] or [°F]

T_r = Reduced temperature, [dimensionless]

U = Phase specific internal energy [J/kg]

u = Specific internal energy of a component in phase [J/kg]

V = Volume, [m^3] or [scf]

V_c = Critical volume, [m^3] or [scf]

V_L = Langmuir volume, [m^3/kg] or [scf/ton]

v = Pore velocity, [m/s] or [ft/s]

v_m = Molar volume, [m^3/mol]

X = Mass fraction, [kg/kg]

Y = Mole fraction, [mol/mol]

Z = Real gas Z-factor, [dimensionless]

Decline Curve Model Variables

a_2 = K1X model initial decline parameter, also denoted D_i [dimensionless]

a_3 = K1X model decline parameter, [1/day]

b = Arps "*b*-parameter" function, derivative of the loss-ratio, [dimensionless]

D = Arps "*D*-parameter" function or loss-ratio, [1/day]

D_i = Arps initial decline rate, [1/day]

D_1 = PLE model initial decline at 1 time-unit, [1/day]

D_∞ = PLE model infinite decline, [1/day]

$\hat{D}_i$ = PLE model decline constant defined by $\hat{D}_i = D_1 / n$, [1/day]

D_{inf} = K1X model terminal decline parameter defined by $D_{\text{inf}} = a_3 - 1$, [1/day]

D_{lim} = MHYP model terminal decline rate, [1/day]

n = PLE/STE/K1X model time exponent, [dimensionless]

Q = Cumulative production function, [STB] or [MSCF]

q = Production rate function, [STB/day] or [MSCF/day]

q_i = Initial production rate, [STB/day] or [MSCF/day]

$\hat{q}_i$ = PLE/STE model rate intercept, [STB/day] or [MSCF/day]

q_{lim} = MHYP model rate at the time of the terminal decline, [STB/day] or [MSCF/day]

$t_{\lim}$ = MHYP model time to the terminal decline, [days]

Dimensionless Field Variables

C_1 = Dimensionless fracture storage factor, inverse of fracture diffusivity

C_{fD} = Dimensionless fracture conductivity

p_{wD} = Dimensionless wellbore pressure

q_D = Dimensionless production rate

Q_D = Dimensionless cumulative production

t_{DA} = Dimensionless time based on drainage area

t_{Dxf} = Dimensionless time based on fracture half-length

u = Laplace transformation variable

w_{fD} = Dimensionless fracture width

x_D = Dimensionless coordinate in *x*-direction

x_{eD} = Dimensionless coordinate of the outer boundary in *x*-direction

x_{wD} = Dimensionless coordinate of the inner boundary in *x*-direction

y_D = Dimensionless coordinate in *y*-direction

y_{eD} = Dimensionless coordinate of the outer boundary in *y*-direction

y_{wD} = Dimensionless coordinate of the inner boundary in *y*-direction

Greek Variables

β = Turbulence correction factor, [m^{-1}] or [ft^{-1}]

γ_{API} = Oil API gravity, [°API]

γ_g = Gas specific gravity, [air = 1]

γ_o = Specific gravity, [water = 1]

λ = Thermal conductivity, [W m^{-1} K^{-1}]

μ = Viscosity, [Pa s] or [cp]

ρ = Density, [kg/m^3] or [lbm/scf]

ξ = Fracture conductivity multiplier tensor, [dimensionless]

ϕ = Porosity, [fraction]

ω = Acentric factor, [dimensionless]

Subscripts

A = Aqueous phase

G = Gaseous phase

R = Rock

O = Organic phase

Superscripts

o = Oil component

g = Methane component

w = Water component

θ = Heat pseudo-component

Mathematical Functions

E_m = General form of the exponential integral

erf = Error function

Γ = Gamma function

K_v = Modified Bessel function of the second kind of the order v

APPENDIX A

SIMULATION INPUT PARAMETERS

Table A1 — Simulation inputs for the three-phase black oil flow problem in the Wolfcamp shale.

Reservoir Properties	
Net pay thickness, h	91.44 m
Formation permeability, k	1.5e-19 m^2
Fracture permeability, k_f	2.0e-12 m^2
Wellbore Radius, r_w	0.05 m
Formation compressibility, c_f	1.0e-9 Pa^{-1}
Porosity, ϕ	0.06 (fraction)
Initial reservoir pressure, p_i	3.15e7 Pa
Initial water saturation, S_w	0.4 (fraction)
Reservoir temperature, T	120 °C
Fluid properties:	
Oil API gravity, γ_{API}	42 °API
Oil bubble-point pressure, p_b	2.07e7 Pa
Oil bubble-point GOR, R_{sb}	1,200 scf/bbl
Initial GOR, R_s	1,100 scf/bbl
Hydraulically fractured well model parameters:	
Fracture half-length, x_f	106.68 m
Number of fractures	200
Fracture spacing, $D_f = 2y_e$	15.24 m
Horizontal well length	3,048 m
Production parameters:	
Flowing pressure, p_{wf}	1.21e7 Pa
Production time, t	14,600 days (~40 years)

Table A2 — Simulation inputs for the two-phase gas-water flow problem in the Marcellus shale.

Reservoir Properties	
Net pay thickness, h	45.72 m
Formation permeability, k	1.5e-19 m^2
Fracture permeability, k_f	2.0e-12 m^2
Wellbore Radius, r_w	0.05 m
Formation compressibility, c_f	1.0e-9 Pa^{-1}
Porosity, ϕ	0.08 (fraction)
Initial reservoir pressure, p_i	3.15e7 Pa
Initial water saturation, S_w	0.4 (fraction)
Reservoir temperature, T	120 °C
Fluid properties:	
PR-EOS for CH_4	
Hydraulically fractured well model parameters:	
Fracture half-length, x_f	91.44 m
Number of fractures	110
Fracture spacing, $D_f = 2y_e$	15.24 m
Horizontal well length	1,676 m
Production parameters:	
Flowing pressure, p_{wf}	1.21e7 Pa
Production time, t	14,600 days (~40 years)

Table A3 — Domain discretization table for the Wolfcamp and Marcellus shale plays.

Discretization Table (Number of Elements)			
N_X	N_Y	N_Z	TOTAL
50	80	55	220000
43	70	48	144480
38	65	42	103740
34	60	37	75480
25	45	28	31500
20	35	22	15400
15	25	16	6000
10	18	11	1980
8	12	8	768

Table A4 —Grid specifications for the Wolfcamp and Marcellus shale plays.

PLAY	Cluster Half Spacing $D_f / 2$		Well Half Spacing L_y		Fracture Half Height $h_f / 2$		Fracture Half Width $w_f / 2$		Fracture Half Length x_f		Wellbore Radius r_w
	ft	m	ft	m	ft	m	in	m	ft	m	m
Wolfcamp	25.0	7.6	656.0	200.0	150.0	45.7	0.05	0.00127	370.0	112.8	0.05
Wolfcamp b	65.6	20.0	656.0	200.0	150.0	45.7	0.05	0.00127	370.0	112.8	0.05
Wolfcamp c	65.6	20.0	656.0	200.0	49.2	15.0	0.05	0.00127	370.0	112.8	0.05
Marcellus	25.0	7.6	600.0	182.9	75.0	22.9	0.05	0.00127	300.0	91.4	0.05
Marcellus b	65.6	20.0	600.0	182.9	75.0	22.9	0.05	0.00127	300.0	91.4	0.05

APPENDIX B

DERIVATION OF THE K1X DECLINE CURVE MODEL PARAMETERS

Here I present the derivation of the *D*- and *b*-parameter functions of the K1X decline curve analysis model.

Recalling the formulation of the K1X model given by **Eq. 5.1**:

$$q(t) = q_i K_1(a_2 + a_3 t)\ \exp\left(a_2 + t\right). \quad (5.1)$$

The definition of the *D*-parameter is given by **Eq. 2.4**:

$$D(t) = -\frac{1}{q(t)}\frac{dq(t)}{dt}. \quad (2.4)$$

Substituting **Eq. 5.1** into **Eq. 2.4** yields:

$$D(t) = -\frac{\frac{d}{dt}\left[q_i K_1(a_2 + a_3 t)\ \exp\left(a_2 + t\right)\right]}{q_i K_1(a_2 + a_3 t)\ \exp\left(a_2 + t\right)}. \quad (B1)$$

Applying the product rule to **Eq. B1** results in:

$$D(t) = -\frac{\exp\left(a_2 + t\right)\frac{d}{dt}\left[K_1(a_2 + a_3 t)\ \right] + K_1(a_2 + a_3 t)\frac{d}{dt}\left[\ \exp\left(a_2 + t\right)\right]}{K_1(a_2 + a_3 t)\ \exp\left(a_2 + t\right)}. \quad (B2)$$

Differentiating the exponential function leads to:

$$D(t) = -\frac{\exp\left(a_2 + t\right)\frac{d}{dt}\left[K_1(a_2 + a_3 t)\ \right] + K_1(a_2 + a_3 t)\exp\left(a_2 + t\right)}{K_1(a_2 + a_3 t)\ \exp\left(a_2 + t\right)}. \quad (B3)$$

Simplifying **Eq. B3** yields:

$$D(t) = -\frac{\frac{d}{dt}\left[K_1(a_2 + a_3 t)\right]}{K_1(a_2 + a_3 t)} - 1 \quad \text{(B4)}$$

Now I can focus on differentiating the modified Bessel function. From Abramowitz and Stegun, Handbook of Mathematical Functions (**p. 376, Eq. 9.6.26(III)**) the recurrence relation between the modified Bessel functions is given by:

$$2\frac{d}{dz}\left[\exp(v\pi i)K_v(z)\right] = \exp\left[(v-1)\pi i\right]K_{v-1}(z) + \exp\left[(v+1)\pi i\right]K_{v+1}(z) \quad \text{(B5)}$$

Substituting the arguments of the Bessel function in **Eq. B4** into **Eq. B5** leads to:

$$2\frac{d}{dt}\left[\exp(\pi i)K_1(a_2 + a_3 t)\right] = a_3\left[K_0(a_2 + a_3 t) + \exp(2\pi i)K_2(a_2 + a_3 t)\right] \quad \text{(B6)}$$

Recalling the Euler's Identity:

$$\exp(\pi i) + 1 = 0 \quad \text{(B7)}$$

Rearranging **Eq. B7** results in:

$$\exp(\pi i) = -1. \quad \text{(B8)}$$

Taking **Eq. B8** to the power of two yields:

$$\exp(2\pi i) = 1. \quad \text{(B9)}$$

Substituting **Eqs. B8-B9** into **Eq. B7** and dividing by two yields:

$$\frac{d}{dt}\left[K_1(a_2 + a_3 t)\right] = -\frac{a_3}{2}\left[K_0(a_2 + a_3 t) + K_2(a_2 + a_3 t)\right]. \quad \text{(B10)}$$

Substituting **Eq. B10** into **Eq. B4** we get the formulation for the K1X *D*-parameter:

$$D(t) = \frac{\frac{a_3}{2}\left[K_0\left(a_2 + a_3 t\right) + K_2\left(a_2 + a_3 t\right)\right]}{K_1(a_2 + a_3 t)} - 1 \quad \text{.....(B11)}$$

I can further simplify **Eq. B11** by using another recurrence relation from Abramowitz and Stegun, Handbook of Mathematical Functions (**p. 376, Eq. 9.6.26(I)**) given by:

$$\exp\left[\left(v-1\right)\pi i\right] K_{v-1}\left(z\right) - \exp\left[\left(v+1\right)\pi i\right] K_{v+1}\left(z\right) = \frac{2v}{z}\exp\left(v\pi i\right) K_v\left(z\right). \quad \text{.....(B12)}$$

Rearranging **Eq. B12** for the highest order Bessel function leads to:

$$\exp\left[\left(v+1\right)\pi i\right] K_{v+1}\left(z\right) = \exp\left[\left(v-1\right)\pi i\right] K_{v-1}\left(z\right) - \frac{2v}{z}\exp\left(v\pi i\right) K_v\left(z\right). \quad \text{.....(B13)}$$

Substituting $v = 1$ and $z = a_2 + a_3 t$ into **Eq. B13** results in:

$$\exp\left(2\pi i\right) K_2\left(a_2 + a_3 t\right) = K_0\left(a_2 + a_3 t\right) - \frac{2}{a_2 + a_3 t}\exp\left(\pi i\right) K_1\left(a_2 + a_3 t\right). \quad \text{.....(B14)}$$

Substituting **Eqs. B8-9** into **Eq. B14** yields:

$$K_2\left(a_2 + a_3 t\right) = K_0\left(a_2 + a_3 t\right) + \frac{2}{a_2 + a_3 t} K_1\left(a_2 + a_3 t\right). \quad \text{.....(B15)}$$

Substituting **Eq. B15** into **Eq. B11**, I dispose of the K_2 Bessel function to obtain:

$$D(t) = \frac{a_3\left[K_0\left(a_2 + a_3 t\right) + K_0\left(a_2 + a_3 t\right) + \frac{2}{a_2 + a_3 t} K_1\left(a_2 + a_3 t\right)\right]}{2K_1(a_2 + a_3 t)} - 1 \quad \text{.....(B16)}$$

Simplifying **Eq. B16** yields the final formulation of the K1X *D*-parameter as given by **Eq. 5.3**:

$$D(t) = \frac{a_3}{a_2 + a_3 t} + \frac{a_3 K_0 \left(a_2 + a_3 t\right)}{K_1 (a_2 + a_3 t)} - 1 \quad \text{.....(5.3)}$$

I can now proceed with the derivation of the *b*-parameter formulation for the K1X DCA model. I begin by recalling the formulation of the *b*-parameter function given by **Eq. 2.6**:

$$b(t) = \frac{d}{dt}\left[\frac{1}{D(t)}\right] \quad \text{.....(2.6)}$$

Eq. 5.3 is not well suited for direct substitution into the definition given by **Eq. 2.6**, since it is not in a full fraction form. I find that **Eq. B11** is more suitable for the substitution, but I need to turn it into the full fraction form given by:

$$D(t) = \frac{a_3\left[K_0\left(a_2 + a_3 t\right) + K_2\left(a_2 + a_3 t\right)\right] - 2K_1(a_2 + a_3 t)}{2K_1(a_2 + a_3 t)} \quad \text{.....(B17)}$$

Substituting **Eq. B17** into **Eq. 2.6** yields:

$$b(t) = \frac{d}{dt}\left[\frac{2K_1(a_2 + a_3 t)}{a_3\left[K_0\left(a_2 + a_3 t\right) + K_2\left(a_2 + a_3 t\right)\right] - 2K_1(a_2 + a_3 t)}\right] \quad \text{.....(B18)}$$

To simplify the derivation, I introduce the following substitution functions:

$$A = K_1(a_2 + a_3 t)\,, \quad \text{.....(B19)}$$

$$B = K_0\left(a_2 + a_3 t\right), \quad \text{.....(B20)}$$

$$C = K_2\left(a_2 + a_3 t\right) \quad \text{.....(B21)}$$

Rewriting **Eq. B18** in terms of the substitution functions given by **Eqs. B19-B21** yields:

$$b(t) = \frac{d}{dt}\left[\frac{2A}{a_3B + a_3C - 2A}\right]. \quad \text{(B22)}$$

Applying the quotient rule to the **Eq. B22** results in:

$$b(t) = \frac{2\left(\frac{d}{dt}A\right)\left(a_3B + a_3C - 2A\right) - 2A\frac{d}{dt}\left(a_3B + a_3C - 2A\right)}{\left(a_3B + a_3C - 2A\right)^2}. \quad \text{(B23)}$$

Applying the sum rule to the **Eq. B23** yields:

$$b(t) = \frac{2\left(\frac{d}{dt}A\right)\left(a_3B + a_3C - 2A\right) - 2A\left(a_3\frac{d}{dt}B + a_3\frac{d}{dt}C - 2\frac{d}{dt}A\right)}{\left(a_3B + a_3C - 2A\right)^2} \quad \text{(B24)}$$

Now I need to differentiate the substitution functions A, B and C. I begin with the function A. The derivative of the **Eq. B19** is given by:

$$\frac{d}{dt}A = \frac{d}{dt}K_1(a_2 + a_3t). \quad \text{(B25)}$$

Notice that **Eq. B25** is equivalent to the **Eq. B10**. Therefore **Eq. B25** becomes:

$$\frac{d}{dt}A = -\frac{a_3}{2}\left[K_0\left(a_2 + a_3t\right) + K_2\left(a_2 + a_3t\right)\right]. \quad \text{(B26)}$$

Taking the derivative of **Eq. B20** yields:

$$\frac{d}{dt}B = \frac{d}{dt}K_0\left(a_2 + a_3t\right). \quad \text{(B27)}$$

From Abramowitz and Stegun, Handbook of Mathematical Functions (**p. 376, Eq. 9.6.27(II)**):

$$\frac{d}{dz}K_0(z) = -K_1(z) \quad \text{(B28)}$$

Using the identity given by **Eq. B28** to the **Eq. B27** and applying the chain rule yields:

$$\frac{d}{dt}B = -a_3 K_1(a_2 + a_3 t) \quad \text{(B29)}$$

The derivative of **Eq. B21** is given by:

$$\frac{d}{dt}C = \frac{d}{dt}K_2(a_2 + a_3 t). \quad \text{(B30)}$$

Substituting $v = 2$ and $z = a_2 + a_3 t$ into **Eq. B5** leads to:

$$2\frac{d}{dt}\left[\exp(2\pi i)K_2(a_2 + a_3 t)\right] = a_3\begin{bmatrix}\exp(\pi i)K_1(a_2 + a_3 t)\\ +\exp(3\pi i)K_3(a_2 + a_3 t)\end{bmatrix} \quad \text{(B31)}$$

Substituting **Eqs. B8-B9** and their product into **Eq. B31** yields:

$$\frac{d}{dt}\left[K_2(a_2 + a_3 t)\right] = \frac{a_3}{2}\left[-K_1(a_2 + a_3 t) - K_3(a_2 + a_3 t)\right]. \quad \text{(B32)}$$

Notice that **Eq. B32** is equivalent to **Eq. B30**. Therefore **Eq. B30** becomes:

$$\frac{d}{dt}C = \frac{a_3}{2}\left[-K_1(a_2 + a_3 t) - K_3(a_2 + a_3 t)\right]. \quad \text{(B33)}$$

However, I do not need the third order Bessel function in my derivation, so I apply the order reduction recurrence relation given by **Eq. B13**. Substituting $v=2$ and $z=a_2+a_3t$ into **Eq. B13** results in:

$$\exp(3\pi i)K_3(a_2+a_3t)=\exp(\pi i)K_1(a_2+a_3t) -\frac{4}{a_2+a_3t}\exp(2\pi i)K_2(a_2+a_3t) \quad \text{.....(B34)}$$

Substituting **Eqs. B8-B9** and their product into **Eq. B34** yields:

$$K_3(a_2+a_3t)=K_1(a_2+a_3t)+\frac{4}{a_2+a_3t}K_2(a_2+a_3t). \quad \text{.....(B35)}$$

Substituting **Eq. B35** into **Eq. B33** leads to:

$$\frac{d}{dt}C=\frac{a_3}{2}\left[-2K_1(a_2+a_3t)-\frac{4}{a_2+a_3t}K_2(a_2+a_3t)\right] \quad \text{.....(B36)}$$

Opening the brackets in **Eq. B36** yields:

$$\frac{d}{dt}C=-a_3K_1(a_2+a_3t)-\frac{2a_3}{a_2+a_3t}K_2(a_2+a_3t) \quad \text{.....(B37)}$$

Now I write out all the results needed to complete the derivation:

$$b(t)=\frac{2\frac{d}{dt}(A)(a_3B+a_3C-2A)-2A\left(a_3\frac{d}{dt}B+a_3\frac{d}{dt}C-2\frac{d}{dt}A\right)}{(a_3B+a_3C-2A)^2}, \quad \text{.....(B24)}$$

$$A=K_1(a_2+a_3t), \quad \text{.....(B19)}$$

$$B=K_0(a_2+a_3t), \quad \text{.....(B20)}$$

$$C = K_2\left(a_2 + a_3 t\right), \quad \text{(B21)}$$

$$\frac{d}{dt}A = -\frac{a_3}{2}\left[K_0\left(a_2 + a_3 t\right) + K_2\left(a_2 + a_3 t\right)\right], \quad \text{(B26)}$$

$$\frac{d}{dt}B = -a_3 K_1\left(a_2 + a_3 t\right), \quad \text{(B29)}$$

$$\frac{d}{dt}C = -a_3 K_1\left(a_2 + a_3 t\right) - \frac{2a_3}{a_2 + a_3 t}K_2\left(a_2 + a_3 t\right) \quad \text{(B37)}$$

I am ready to substitute **Eqs. B19-B21, B26, B29, B37** into **Eq. B24**. Note that, since all the arguments of the modified Bessel functions are equivalent, I will not write them out until the final stage of the derivation procedure to avoid overcrowding. After the substitution **Eq. B24** becomes:

$$b(t) = \frac{\begin{array}{l} 2\left[-\frac{a_3}{2}\left(K_0 + K_2\right)\right]\left(a_3 K_0 + a_3 K_2 - 2K_1\right) - \\ 2K_1\left[a_3\left(-a_3 K_1\right) + a_3\left(-a_3 K_1 - \frac{2a_3}{a_2 + a_3 t}K_2\right) - 2\left(-\frac{a_3}{2}\left(K_0 + K_2\right)\right)\right] \end{array}}{\left(a_3 K_0 + a_3 K_2 - 2K_1\right)^2}. \quad \text{(B38)}$$

Opening the first round of brackets yields:

$$b(t) = \frac{\begin{array}{l} -a_3\left(K_0 + K_2\right)\left(a_3 K_0 + a_3 K_2 - 2K_1\right) \\ -2K_1\left[-2{a_3}^2 K_1 - \frac{2{a_3}^2}{a_2 + a_3 t}K_2 + a_3 K_0 + a_3 K_2\right] \end{array}}{\left(a_3 K_0 + a_3 K_2 - 2K_1\right)^2}. \quad \text{(B39)}$$

Opening the second round of brackets yields:

$$b(t)=\frac{\left(-a_3K_0-a_3K_2\right)\left(a_3K_0+a_3K_2-2K_1\right)-2K_1\left[-2a_3{}^2K_1-\frac{2a_3{}^2}{a_2+a_3t}K_2+a_3K_0+a_3K_2\right]}{\left(a_3K_0+a_3K_2-2K_1\right)^2} \quad \text{.....(B40)}$$

Opening the brackets of the first term of the numerator of the **Eq. B40** leads to:

$$\begin{aligned}\left(-a_3K_0-a_3K_2\right)\left(a_3K_0+a_3K_2-2K_1\right)=&-a_3{}^2K_0{}^2-a_3{}^2K_0K_2+2a_3K_0K_1\\&-a_3{}^2K_0K_2-a_3{}^2K_2{}^2+2a_3K_1K_2\end{aligned} \quad \text{.....(B41)}$$

Adding similar terms yields:

$$\begin{aligned}\left(-a_3K_0-a_3K_2\right)\left(a_3K_0+a_3K_2-2K_1\right)=&-a_3{}^2K_0{}^2-2a_3{}^2K_0K_2+2a_3K_0K_1\\&-a_3{}^2K_2{}^2+2a_3K_1K_2\end{aligned} \quad \text{.....(B42)}$$

Substituting **Eq. B42** into the numerator of the **Eq. B40** and opening the last round of brackets results in:

$$\begin{aligned}Numerator=&-a_3{}^2K_0{}^2-2a_3{}^2K_0K_2+2a_3K_0K_1-a_3{}^2K_2{}^2+2a_3K_1K_2\\&+4a_3{}^2K_1{}^2+\frac{4a_3{}^2}{a_2+a_3t}K_1K_2-2a_3K_0K_1-2a_3K_1K_2\end{aligned} \quad \text{.....(B43)}$$

Cancelling the similar terms yields:

$$Numerator=-a_3{}^2K_0{}^2-2a_3{}^2K_0K_2-a_3{}^2K_2{}^2+4a_3{}^2K_1{}^2+\frac{4a_3{}^2}{a_2+a_3t}K_1K_2 \quad \text{.....(B44)}$$

Simplification of **Eq. B44** results in:

$$Numerator=-a_3{}^2\left[K_0{}^2+2K_0K_2+K_2{}^2-4K_1{}^2-\frac{4}{a_2+a_3t}K_1K_2\right] \quad \text{.....(B45)}$$

Recall **Eq. B15** given by:

$$K_2\left(a_2+a_3t\right)=K_0\left(a_2+a_3t\right)+\frac{2}{a_2+a_3t}K_1\left(a_2+a_3t\right). \quad \text{(B15)}$$

Substituting **Eq. B15** into the combined terms of **Eq. B45** yields:

$$Numerator=-a_3{}^2\left[\begin{array}{l} K_0{}^2+2K_0\left(K_0+\frac{2}{a_2+a_3t}K_1\right)+K_2{}^2 \\ -4K_1{}^2-\frac{4}{a_2+a_3t}K_1\left(K_0+\frac{2}{a_2+a_3t}K_1\right)\end{array}\right]. \quad \text{(B46)}$$

Opening the brackets leads to:

$$\begin{aligned}-\frac{Numerator}{a_3{}^2}=&K_0{}^2+2K_0{}^2+\frac{4}{a_2+a_3t}K_0K_1+K_2{}^2\\ &-4K_1{}^2-\frac{4}{a_2+a_3t}K_0K_1-\frac{8}{\left(a_2+a_3t\right)^2}K_1{}^2\end{aligned}. \quad \text{(B47)}$$

Cancelling out the similar terms in **Eq. B47** results in:

$$-\frac{Numerator}{a_3{}^2}=3K_0{}^2+K_2{}^2-4K_1{}^2-\frac{8}{\left(a_2+a_3t\right)^2}K_1{}^2. \quad \text{(B48)}$$

Combining the similar terms yields:

$$-\frac{Numerator}{a_3{}^2}=3K_0{}^2-\left[4+\frac{8}{\left(a_2+a_3t\right)^2}\right]K_1{}^2+K_2{}^2. \quad \text{(B49)}$$

Simplifications of **Eq. B49** results in:

$$Numerator = a_3^{\,2}\left[-3K_0^{\,2} + \frac{4\left[\left(a_2 + a_3 t\right)^2 + 2\right]K_1^{\,2}}{\left(a_2 + a_3 t\right)^2} - K_2^{\,2}\right] \quad \text{.....(B50)}$$

Finally, I substitute **Eq. B50** into **Eq. B40** to get the formulation of the *b*-parameter of the K1X model as given by **Eq. 5.4**:

$$b(t) = a_3^{\,2}\frac{\left[-3K_0\left(a_2 + a_3 t\right)^2 + \frac{4[(a_2 + a_3 t)^2 + 2]K_1\left(a_2 + a_3 t\right)^2}{\left(a_2 + a_3 t\right)^2} - K_2\left(a_2 + a_3 t\right)^2\right]}{\left[a_3[K_0\left(a_2 + a_3 t\right) + K_2\left(a_2 + a_3 t\right)] - 2K_1\left(a_2 + a_3 t\right)\right]^2} \quad \text{.....(5.4)}$$

APPENDIX C

DERIVATION OF THE LIMITING FORM OF THE K1X DECLINE CURVE MODEL

The *D*-parameter function for the K1X model is given by **Eq. 5.3**:

$$D(t)=\frac{a_3}{a_2+a_3t}+\frac{a_3K_0(a_2+a_3t)}{K_1(a_2+a_3t)}-1. \quad \text{(C1)}$$

Now let us inspect the second term containing the modified Bessel functions. Recall the Hankel's asymptotic expansion of the modified Bessel function of the second kind for a large argument:

$$K_v(z)\sim\sqrt{\frac{\pi}{2z}}e^{-z}\left[1+\frac{4v^2-1}{8z}+\frac{\left(4v^2-1\right)\left(4v^2-9\right)}{2!\left(8z\right)^2}+\frac{\left(4v^2-1\right)\left(4v^2-9\right)\left(4v^2-25\right)}{3!\left(8z\right)^3}+\ldots\right] \quad \text{(C2)}$$

Since the second term of **Eq. C1** is not dominant, I substitute the first order expansion given in **Eq. C2** to find a limiting form of the ratio of the Bessel functions in **Eq. C1** yielding:

$$\frac{K_0(z)}{K_1(z)}=\frac{\sqrt{\frac{\pi}{2z}}e^{-z}\left(1+\frac{4\cdot0^2-1}{8z}\right)}{\sqrt{\frac{\pi}{2z}}e^{-z}\left(1+\frac{4\cdot1^2-1}{8z}\right)} \quad \text{(C3)}$$

Simplification of **Eq. C3** yields:

$$\frac{K_0(z)}{K_1(z)}=\frac{1-\frac{1}{8z}}{1+\frac{3}{8z}}=\frac{8z-1}{8z+3}=1-\frac{4}{8z+3}. \quad \text{(C4)}$$

Substituting the argument into **Eq. C4** and further simplifying yields:

$$\frac{K_0\left(a_2+a_3t\right)}{K_1\left(a_2+a_3t\right)}=1-\frac{1}{2\left(a_2+a_3t\right)+3/4} \quad \text{(C5)}$$

To simplify further operations, I discard the ¾ term as it is not significant for large values of *t* and obtain:

$$\frac{K_0\left(a_2+a_3t\right)}{K_1\left(a_2+a_3t\right)}=1-\frac{1}{2\left(a_2+a_3t\right)} \quad \text{(C6)}$$

Substituting **Eq. C6** into **Eq. C1** I get:

$$D(t)=\frac{a_3}{a_2+a_3t}+a_3-\frac{a_3}{2\left(a_2+a_3t\right)}-1. \quad \text{(C7)}$$

Performing simple algebraic operations on **Eq. C7** yields:

$$D(t)=a_3+\frac{a_3}{2\left(a_2+a_3t\right)}-1, \quad \text{(C8)}$$

Eq. C8 is a limiting form of the *D*-parameter of the K1X model. Taking the limit of **Eq. C8** as *t* approaches infinity, I obtain the expression for the terminal decline parameter as:

$$D_{\text{inf}}=a_3-1 \quad \text{(C9)}$$

Notice that **Eq. C9** is identical to the K1X terminal decline formulation.

To get the expression for the rate-time relationship, I substitute **Eq. C8** into the definition of the *D*-parameter given by **Eq. 2.4**, yielding:

$$-\frac{1}{q(t)}\frac{dq(t)}{dt}=a_3+\frac{a_3}{2(a_2+a_3t)}-1\,. \quad \text{(C10)}$$

Separating and integrating **Eq. C10** results in:

$$-\int\frac{1}{q(t)}dq(t)=\int\left(a_3+\frac{a_3}{2(a_2+a_3t)}-1\right)dt\,, \quad \text{(C11)}$$

$$-\ln\left[q(t)\right]+c=a_3t+\frac{1}{2}\ln(a_2+a_3t)-t\,, \quad \text{(C12)}$$

Introducing the initial production rate q_i as the integration constant *c* yields:

$$-\ln\left[q(t)/q_i\right]=a_3t+\frac{1}{2}\ln(a_2+a_3t)-t \quad \text{(C13)}$$

Exponentiation of **Eq. C13** leads to:

$$q(t)/q_i=\exp\left(-a_3t-\frac{1}{2}\ln(a_2+a_3t)+t\right) \quad \text{(C14)}$$

Simplifying **Eq. C14** yields:

$$q(t)/q_i=\frac{\exp(-a_3t+t)}{\exp\left(\frac{1}{2}\ln(a_2+a_3t)\right)}, \quad \text{(C15)}$$

$$q(t)=q_i\frac{\exp\left[-(a_3-1)t\right]}{(a_2+a_3t)^{1/2}}\,. \quad \text{(C16)}$$

Eq. C16 is the limiting form of the K1X rate-time relationship given by **Eq. 5.1**. Substituting **Eq. C9** into **Eq. C16,** I obtain the formulation of the limiting form of the K1X model in terms of terminal decline given by:

$$q(t) = q_i \frac{\exp\left[-D_{\text{inf}} t\right]}{\left[a_2 + (1 + D_{\text{inf}})t\right]^{1/2}} \quad \text{(C17)}$$

I continue by deriving the formulation for the *b*-parameter. In order to do so, I begin by manipulating **Eq. C8** in the following manner:

$$D(t) = \frac{2a_3(a_2 + a_3 t) + a_3 - 2(a_2 + a_3 t)}{2(a_2 + a_3 t)}, \quad \text{(C18)}$$

$$D(t) = \frac{2(a_3 - 1)(a_2 + a_3 t) + a_3}{2(a_2 + a_3 t)} \quad \text{(C19)}$$

Now I substitute **Eq. C19** into the definition of the *b*-parameter given by **Eq. 2.6**, yielding:

$$b(t) = \frac{d}{dt}\left[1 \Big/ \frac{2(a_3 - 1)(a_2 + a_3 t) + a_3}{2(a_2 + a_3 t)}\right], \quad \text{(C20)}$$

$$b(t) = \frac{d}{dt}\left[\frac{2(a_2 + a_3 t)}{2(a_3 - 1)(a_2 + a_3 t) + a_3}\right]. \quad \text{(C21)}$$

The derivative of **Eq. C21** results in:

$$b(t) = \frac{2\frac{d(a_2 + a_3 t)}{dt}\left[2(a_3 - 1)(a_2 + a_3 t) + a_3\right] - 2(a_2 + a_3 t)\frac{d}{dt}\left[2(a_3 - 1)(a_2 + a_3 t) + a_3\right]}{\left[2(a_3 - 1)(a_2 + a_3 t) + a_3\right]^2} \quad \text{(C22)}$$

$$b(t) = \frac{2a_3\left[2(a_3 - 1)(a_2 + a_3 t) + a_3\right] - 2(a_2 + a_3 t)\frac{d}{dt}\left[2(a_3 a_2 - a_2 + a_3{}^2 t - a_3 t) + a_3\right]}{\left[2(a_3 - 1)(a_2 + a_3 t) + a_3\right]^2}, \quad \text{(C23)}$$

$$b(t)=\frac{4a_3(a_3-1)(a_2+a_3t)+2a_3{}^2-4a_3(a_2+a_3t)(a_3-1)}{\left[2(a_3-1)(a_2+a_3t)+a_3\right]^2}. \quad \text{(C24)}$$

Finally, I have a formulation for the limiting form of the *b*-parameter of the K1X model:

$$b(t)=\frac{2a_3{}^2}{\left[2(a_3-1)(a_2+a_3t)+a_3\right]^2}. \quad \text{(C25)}$$

I continue by deriving the expression for cumulative production for the limiting form of the K1X model. To do so, I need to integrate **Eq. C15**:

$$Q_D(t)=\int_0^t\frac{\exp\left[-(a_3-1)t\right]}{(a_2+a_3t)^{1/2}}dt. \quad \text{(C26)}$$

I will attempt to take the integral using the method of substitution. In order to do so, I need to transform the arguments. I begin with the argument of the exponential function:

$$(a_3-1)t=a_2+a_3t-t-a_2, \quad \text{(C27)}$$

$$(a_3-1)t=a_2+a_3t-\frac{a_3(t+a_2)}{a_3}, \quad \text{(C28)}$$

$$(a_3-1)t=(a_2+a_3t)-\frac{a_3t+a_3a_2+a_2-a_2}{a_3}, \quad \text{(C29)}$$

$$(a_3-1)t=(a_2+a_3t)-\frac{(a_2+a_3t)}{a_3}-a_2+\frac{a_2}{a_3}, \quad \text{(C30)}$$

$$(a_3-1)t=\frac{(a_3-1)(a_2+a_3t)}{a_3}-a_2+\frac{a_2}{a_3}. \quad \text{(C31)}$$

Substituting **Eq. C31** into **Eq. C26,** and moving the constant outside the integral, leads to:

$$Q_D(t) = \exp[a_2 - \frac{a_2}{a_3}]\int_0^t \frac{\exp\left[-(a_3-1)(a_2+a_3t)/a_3\right]}{(a_2+a_3t)^{1/2}}dt \,. \quad \text{(C32)}$$

Introducing the substitution function z defined by:

$$z(t) = \sqrt{\frac{(a_3-1)(a_2+a_3t)}{a_3}} \,. \quad \text{(C33)}$$

I continue by manipulating the argument of the power-law in the denominator to get an expression with respect to the substitution variable:

$$a_2 + a_3t = Cz^2, \quad \text{(C34)}$$

$$a_2 + a_3t = C\frac{(a_3-1)}{a_3}(a_2+a_3t), \quad \text{(C35)}$$

$$C = \frac{a_3}{a_3-1}, \quad \text{(C36)}$$

$$a_2 + a_3t = \frac{a_3}{a_3-1}z^2 \,. \quad \text{(C37)}$$

The last step in the substitution procedure is to calculate the derivative of the substitution function:

$$dz(t) = d\sqrt{\frac{(a_3-1)(a_2+a_3t)}{a_3}}dt \,, \quad \text{(C38)}$$

$$dz(t) = \frac{d\left[(a_3-1)(a_2+a_3t)/a_3\right]}{2\sqrt{\frac{(a_3-1)(a_2+a_3t)}{a_3}}}dt \,, \quad \text{(C39)}$$

$$dz(t) = \frac{a_3 - 1}{2\sqrt{\frac{(a_3 - 1)(a_2 + a_3 t)}{a_3}}} dt \quad \text{(C40)}$$

Substituting **Eq. C33** into **Eq. C40** and rearranging for *dt* yields:

$$dt = \frac{2z}{a_3 - 1} dz \quad \text{(C41)}$$

Now, I can integrate by substitution using **Eqs. C32**, **C33**, **C37**, **C41,** arriving at:

$$Q_D(t) = \exp[a_2 - \frac{a_2}{a_3}] \int_0^t \frac{\exp\left[-z^2\right]}{\left(\frac{a_3}{a_3 - 1} z^2\right)^{1/2}} \frac{2z}{a_3 - 1} dz \quad \text{(C42)}$$

Assuming z to be non-negative, **Eq. C42** becomes:

$$Q_D(t) = \frac{\exp[a_2 - \frac{a_2}{a_3}]}{\sqrt{a_3(a_3 - 1)}} 2 \int_0^t \exp\left[-z^2\right] dz \quad \text{(C43)}$$

Recall the definition of the error function:

$$erf(t) = \frac{2}{\sqrt{\pi}} \int_0^t \exp\left[-z^2\right] dz \quad \text{(C44)}$$

Substituting **Eq. C44** into **Eq. C43**, and returning to the original variables, yields the expression for the dimensionless cumulative production of the limiting form of the K1X DCA model:

$$Q_D(t) = \frac{\sqrt{\pi} \exp[a_2 - a_2 / a_3]}{\sqrt{a_3(a_3 - 1)}} \left[erf\left[\sqrt{\frac{(a_3 - 1)(a_2 + a_3 t)}{a_3}} \right] - erf\left[\sqrt{\frac{(a_3 - 1) a_2}{a_3}} \right] \right] \quad \text{(C45)}$$

I can derive an alternate form of **Eq. C45** by applying the incomplete Gamma function definition of the error function that is given by:

$$erf\left(x\right)=1-\frac{1}{\sqrt{\pi}}\Gamma\left(\frac{1}{2},x^2\right). \quad \text{(C46)}$$

Substituting **Eq. C46** into **Eq. C45**, I obtain the following alternate form of the dimensionless cumulative production relation:

$$Q_D\left(t\right)=\frac{\exp[a_2-a_2/a_3]}{\sqrt{a_3\left(a_3-1\right)}}\left[\Gamma\left(\frac{1}{2},\frac{\left(a_3-1\right)a_2}{a_3}\right)-\Gamma\left(\frac{1}{2},\frac{\left(a_3-1\right)\left(a_2+a_3t\right)}{a_3}\right)\right]. \quad \text{(C47)}$$

Now I need to compare the derived limiting form of the K1X model with the original form. **Figs. C1-C2** show the type curves for the limiting form of the K1X model with respect to the variable D_i- (or a_2-) parameter and the terminal decline D_{inf}- (or a_3-) parameter respectively.

From the assumptions made during the derivation, I only expect a difference in the early-time behavior of the limiting form of the K1X model. From **Figs. C1-C2,** I observe that the characteristic behavior is very similar to the K1X model. To get a higher resolution of the deviation between the limiting form and the model, I plot the "*qDb*" values for both models with all parameters kept equal. The comparison plot is shown on **Fig. C3**.

Inspecting **Fig. C3**, I note that the derivative functions *D*- and *b*-parameter converge in 10 days, thus confirming the validity of our assumption that the limiting form will only differ during very early times. The rate function, however, is shifted down for the limiting form, meaning that the D_i (a_2-) and q_i- parameters should be different for the two

models when approximating the same data, while the terminal decline parameter remains identical for both models. Thus, the correlation given by **Eq. 5.9** is valid for the limiting form.

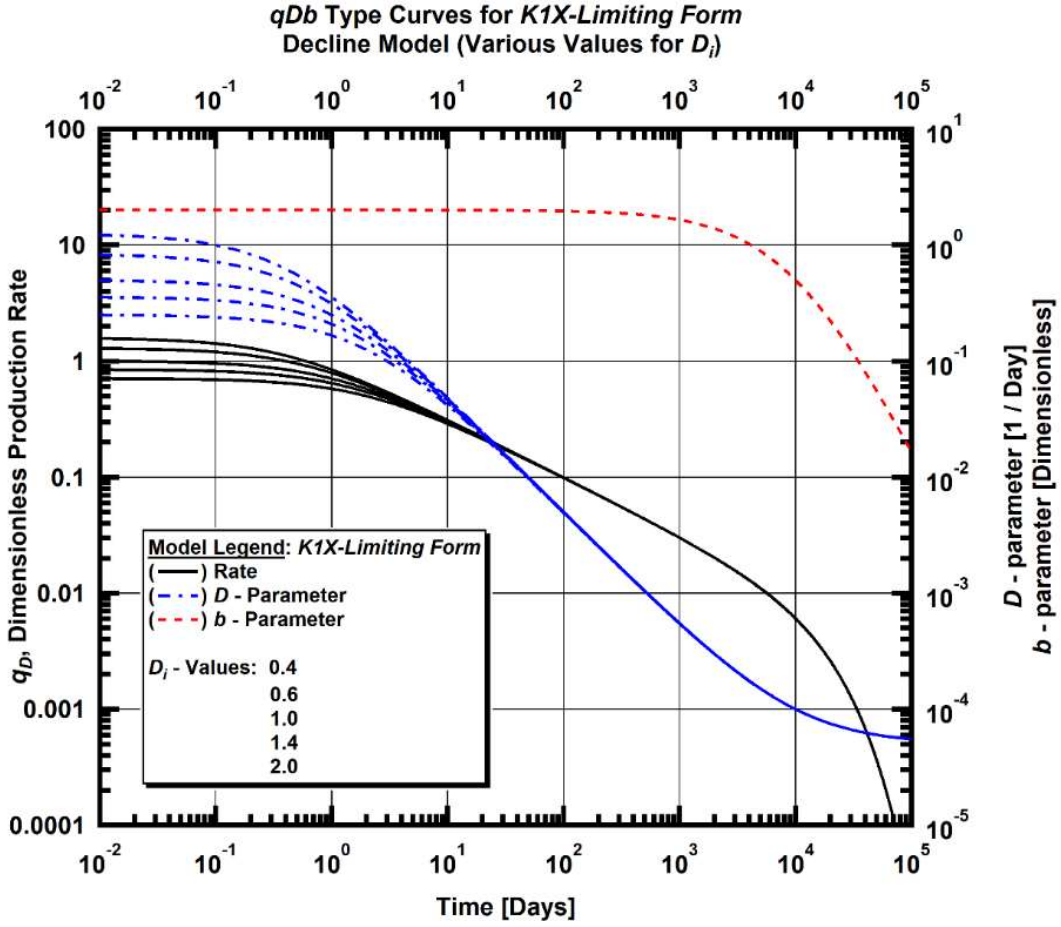

Figure C1— Log-log "*qDb*" plot of the limiting form of the K1X model type curves with respect to various values of the initial decline parameter.

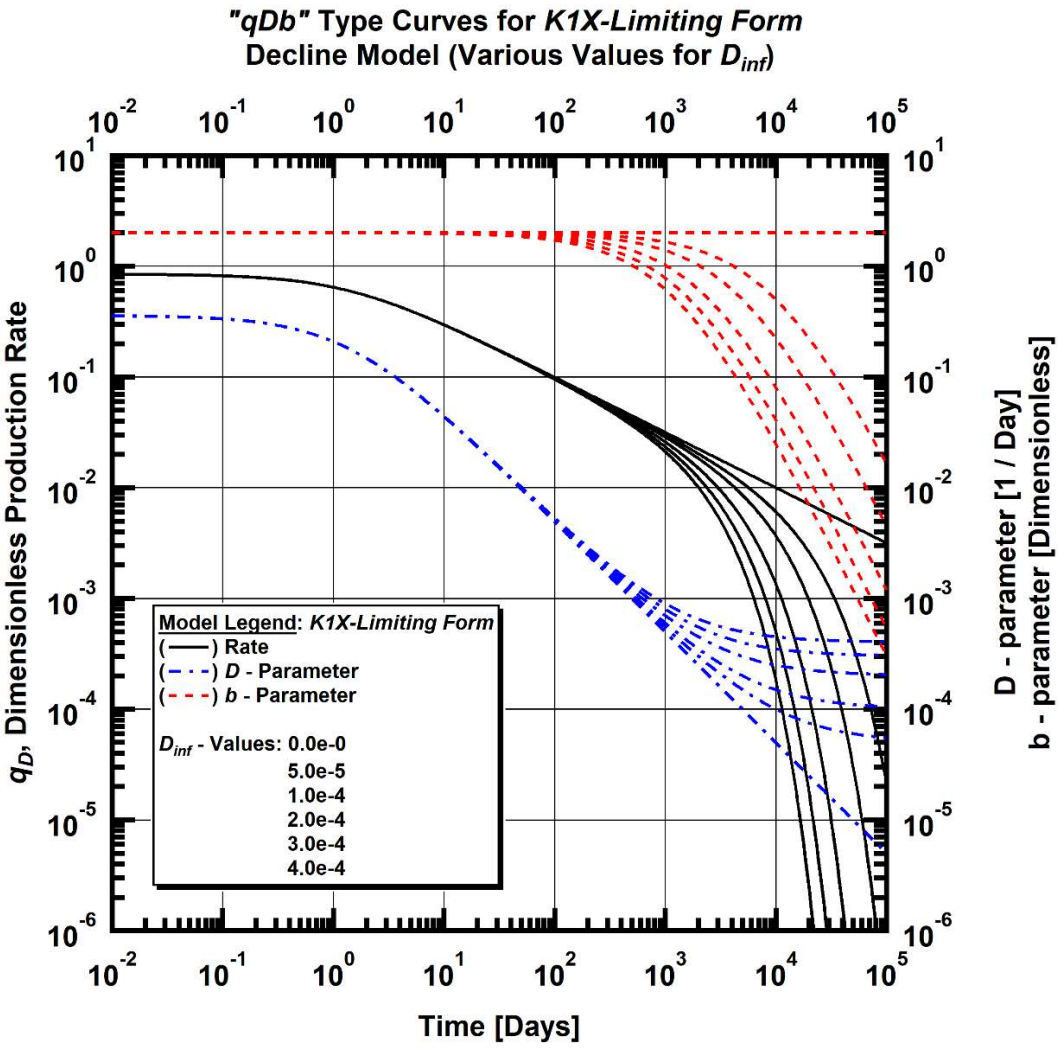

Figure C2— Log-log "*qDb*" plot of the limiting form of the K1X model type curves with respect to various values of the terminal decline parameter.

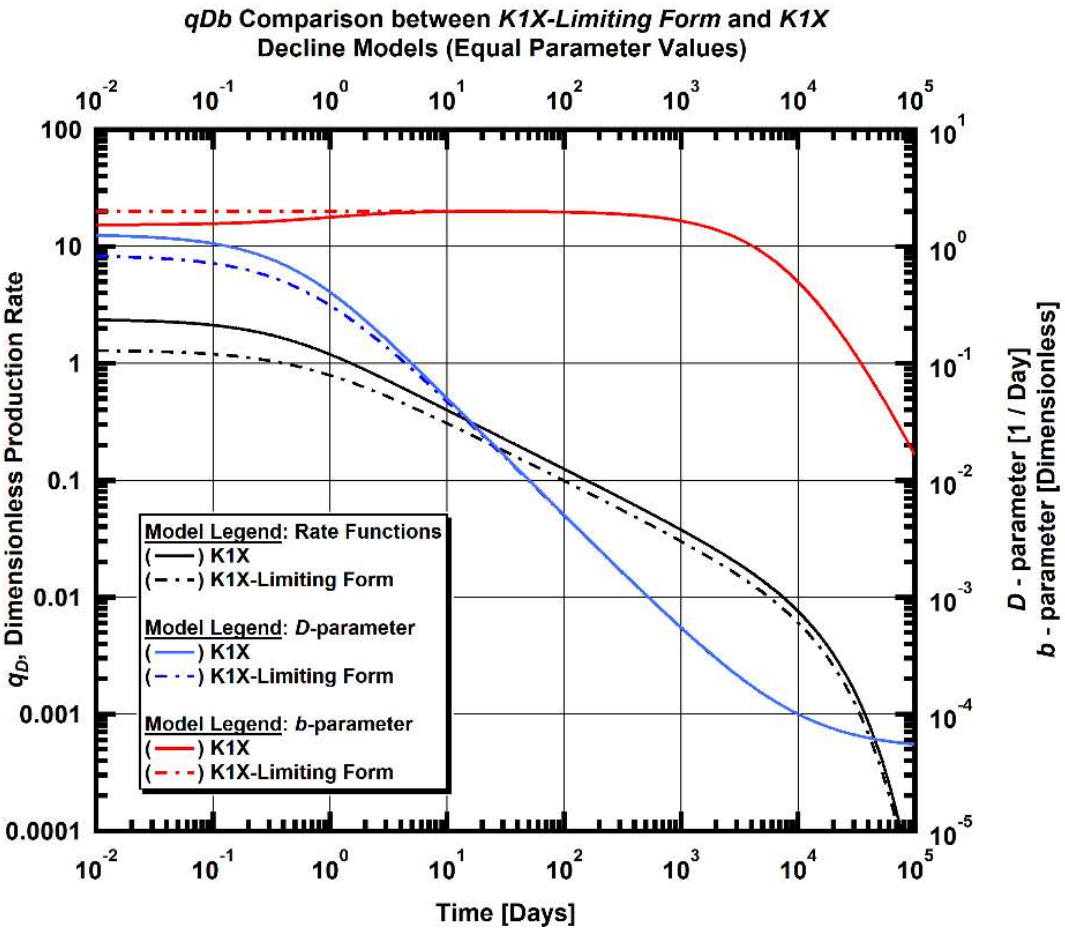

Figure C3— Log-log "*qDb*" plot of the comparison between the K1X and the limiting form of the K1X model with equal parameter values.

APPENDIX D

DERIVATION OF THE GENERAL FORM OF THE K1X DECLINE CURVE MODEL

The original form of the K1X model as given by **Eq. 5.1** as well as the limiting form given by **Eq. C16** are valid only for a well experiencing transient "linear flow" regime characterized by the -1/2 slope. However, this is a specific case that is not necessarily observed in the production data. In order to generalize the model for other types of transient flow regimes, I propose a new form of a rate-time relationship given by:

$$q(t) = q_i \frac{\exp\left[-(a_3 - 1)t\right]}{(a_2 + a_3 t)^{1/n}}, \quad \text{(D1)}$$

where n is the "slope of transient flow" parameter.

Recalling the definition of the D-parameter we have:

$$D(t) = -\frac{1}{q(t)}\frac{dq(t)}{dt}, \quad \text{(2.4)}$$

$$D(t) = -\frac{(a_2 + a_3 t)^{1/n}}{\exp\left[-(a_3 - 1)t\right]}\frac{d}{dt}\left[\frac{\exp\left[-(a_3 - 1)t\right]}{(a_2 + a_3 t)^{1/n}}\right], \quad \text{(D2)}$$

$$D(t) = -\frac{(a_2 + a_3 t)^{1/n}}{\exp\left[-(a_3 - 1)t\right]}\frac{-(a_3 - 1)\exp\left[-(a_3 - 1)t\right] - \frac{1}{n}\frac{a_3}{a_2 + a_3 t}\exp\left[-(a_3 - 1)t\right]}{(a_2 + a_3 t)^{1/n}}, \quad \text{(D3)}$$

$$D(t) = \frac{a_3}{n(a_2 + a_3 t)} + a_3 - 1 \quad \text{(D4)}$$

Recall the definition of the *b*-parameter:

$$b(t)=\frac{d}{dt}\left(\frac{1}{D(t)}\right), \quad (2.6)$$

$$b(t)=\frac{d}{dt}\left(\frac{n(a_2+a_3t)}{n(a_2+a_3t)(a_3-1)+a_3}\right), \quad (D5)$$

$$b(t)=\frac{na_3\left[n(a_2+a_3t)(a_3-1)+a_3\right]-n(a_2+a_3t)na_3(a_3-1)}{\left[n(a_2+a_3t)(a_3-1)+a_3\right]^2}, \quad (D6)$$

$$b(t)=\frac{na_3^{\,2}}{\left[n(a_2+a_3t)(a_3-1)+a_3\right]^2}. \quad (D7)$$

Finally, I derive an expression for the cumulative production function. In order to simplify the derivation, I integrate the dimensionless rate function:

$$Q_D(t)=\int_0^t \frac{\exp\left[-(a_3-1)t\right]}{(a_2+a_3t)^{1/n}}dt, \quad (D8)$$

I approach the integration using the method of variable substitution. From **Eq. C31**:

$$(a_3-1)t=\frac{(a_3-1)(a_2+a_3t)}{a_3}-a_2+\frac{a_2}{a_3} \quad (C31)$$

Then, I introduce the substitution function *z* given by:

$$z(t)=\frac{(a_3-1)(a_2+a_3t)}{a_3}. \quad (D9)$$

With the new variable, **Eq. C37** becomes:

$$a_2 + a_3 t = \frac{a_3}{a_3 - 1} z \,. \quad \text{(D10)}$$

Taking the derivative of **Eq. D9** results in:

$$dz = \left(a_3 - 1\right) dt \,. \quad \text{(D11)}$$

Rearranging **Eq. D11** for *dt* leads to:

$$dt = \frac{dz}{a_3 - 1} \,. \quad \text{(D12)}$$

Substituting **Eqs. D9**, **D10** and **D12** into **Eq. D8** yields:

$$Q_D\left(t\right) = \int_0^t \frac{\exp\left[-z + a_2 - \frac{a_2}{a_3}\right]}{\left(\frac{a_3}{a_3 - 1} z\right)^{1/n}} \frac{dz}{\left(a_3 - 1\right)} \,. \quad \text{(D13)}$$

Moving all the constants outside the integral in **Eq. D13** results in:

$$Q_D\left(t\right) = \frac{\exp[a_2 - \frac{a_2}{a_3}]}{\left(\frac{a_3}{a_3 - 1}\right)^{1/n} \left(a_3 - 1\right)} \int_0^t \frac{\exp\left(-z\right)}{z^{1/n}} dz \,. \quad \text{(D14)}$$

Simplifying **Eq. D14** yields:

$$Q_D\left(t\right) = \frac{\exp[a_2 - \frac{a_2}{a_3}]}{a_3^{\,1/n} \left(a_3 - 1\right)^{1-1/n}} \int_0^t \frac{\exp\left(-z\right)}{z^{1/n}} dz \,. \quad \text{(D15)}$$

Recalling the definition of the incomplete Gamma function:

$$\Gamma(m,x)=\int_0^x z^{m-1}\exp(-z)dz\ . \quad \text{(D16)}$$

Substituting **Eqs. D9** and **D16** into **Eq. D15** yields a formulation of the dimensionless cumulative production function:

$$Q_D(t)=\frac{\exp[a_2-\frac{a_2}{a_3}]}{a_3^{1/n}(a_3-1)^{1-1/n}}\left[\Gamma\left(1-\frac{1}{n},\frac{a_2}{a_3}(a_3-1)\right)-\Gamma\left(1-\frac{1}{n},\frac{a_2+a_3t}{a_3}(a_3-1)\right)\right]. \quad \text{(D17)}$$

Recall the relation between the incomplete Gamma function and the general form of the exponential integral is given by:

$$E_m(x)=x^{m-1}\Gamma(1-m,x). \quad \text{(D18)}$$

Substituting **Eq. D18** into **Eq. D17**, I derive the following alternative formulation for the dimensionless cumulative production function:

$$Q_D(t)=\frac{\exp[a_2-\frac{a_2}{a_3}]}{a_3^{1/n}(a_3-1)^{1-1/n}}\left[\left[\frac{a_2}{a_3}(a_3-1)\right]^{1-1/n}E_{1/n}\left[\frac{a_2}{a_3}(a_3-1)\right]-\left[\frac{a_2+a_3t}{a_3}(a_3-1)\right]^{1-1/n}E_{1/n}\left[\frac{a_2+a_3t}{a_3}(a_3-1)\right]\right], \quad \text{(D19)}$$

$$Q_D(t)=\frac{\exp[a_2-\frac{a_2}{a_3}]}{a_3}\left[\frac{E_{1/n}\left[\frac{a_2}{a_3}(a_3-1)\right]}{a_2^{1/n-1}}-\frac{E_{1/n}\left[\frac{a_2+a_3t}{a_3}(a_3-1)\right]}{(a_2+a_3t)^{1/n-1}}\right] \quad \text{(D20)}$$

Fig. D1 shows the type curves for the generalized form of the K1X model derived above with respect to the slope parameter *n*. Since the behavior of the other parameters should

be identical to the limiting form of the K1X model derived in **Appendix C**, I do not plot them.

From **Fig. D1** I observe that the slope values of the parameter *n* result in the same value of the *b*-parameter function before the onset of the terminal decline. I also observe that all the rates and the *D*-parameter functions shown on **Fig. D1** converge at late times, proving that the terminal decline parameters are equivalent in the different slope curves and in the limiting form of the K1X, as well as in the original K1X model. Thus, the correlation given by **Eq.5.9** is valid for the generalized model of the K1X rate-time model.

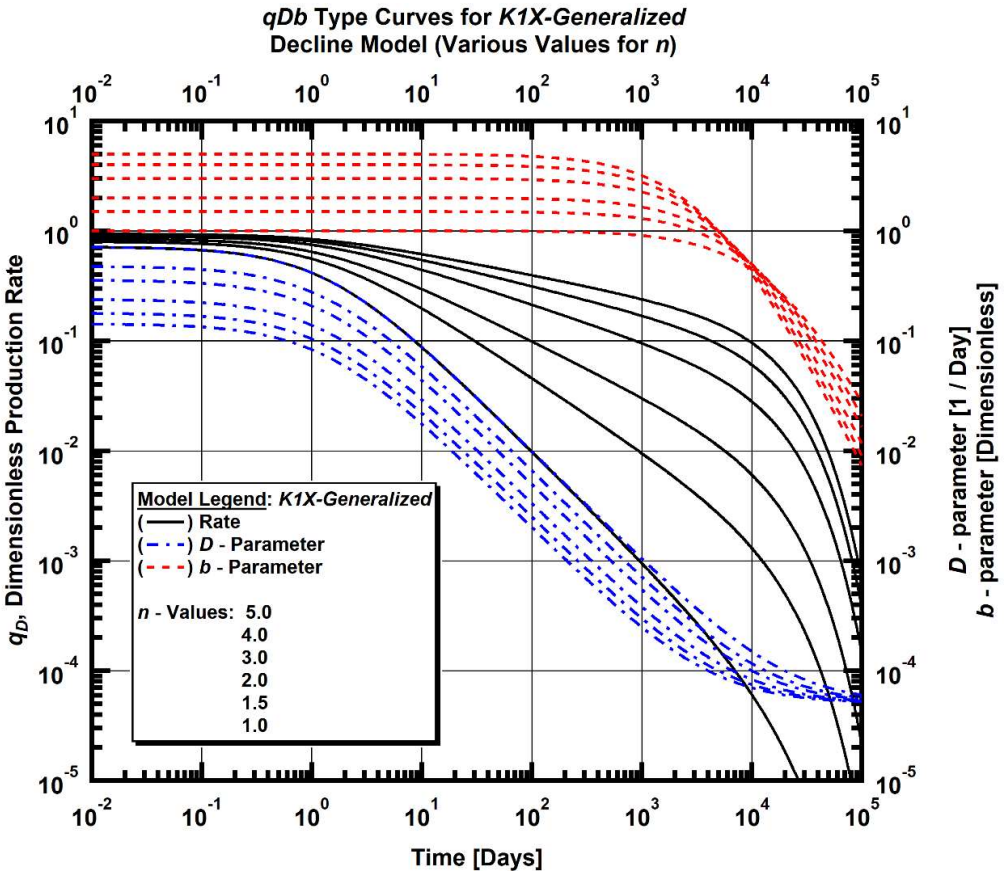

Figure D1— Log-log "*qDb*" plot of the generalized form of the K1X model type curves with respect to various values of the slope parameter.